

INAUGURAL - DISSERTATION

zur Erlangung der Doktorwürde
der Naturwissenschaftlich-Mathematischen Gesamtfakultät
der Ruprecht-Karls-Universität Heidelberg

vorgelegt von

Diplom-Biologe Diplom-Mathematiker Moritz Mercker

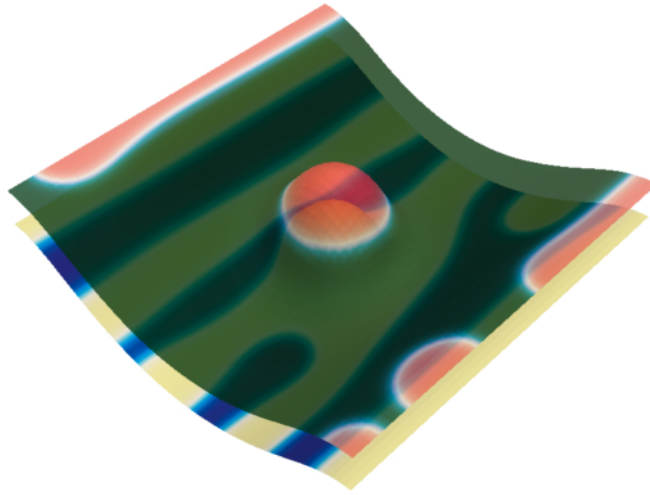
aus Oldenburg

Tag der mündlichen Prüfung:

Models, Numerics and Simulations of Deforming Biological Surfaces

Gutachter: Professor Dr. Dr. h.c. mult Willi Jäger

.....



Snapshot of a deforming bilayer membrane simulation

"A model should not fit all the facts, since not all of the facts are right"

- Francis Crick

To Virginie and Eline

ABSTRACT

Thin, elastic surfaces are a fundamental building block in each biological system. Their main representative on the small scale are biomembranes; an important example on the larger scale are cell tissues. In both cases, the surfaces define a mechanical and chemical border, indispensable for the genesis and maintenance of each organism. An essential property of the surfaces is a lateral inhomogeneous composition of the surfaces themselves: without these inhomogeneities, the complexity of shapes, mechanochemical properties and dynamics would not be possible.

In this thesis, we develop continuous mechanobiological models of membranes and tissues. Since these surfaces are experimentally often difficult to access, our approaches allow to investigate their behavior theoretically. The developed mathematical models are coupled nonlinear systems of partial differential equations (PDE) of fourth order. To enable simulations of these models, we significantly extend numerical algorithms for surface deformation based on the finite-element method (FEM).

Extensive systematic simulations of the different models - in close comparison to recent experimental and theoretical studies on different scales - lead to new findings in membrane as well as tissue research. The key findings are the prediction and characterization of new mechanisms of communication between the two monolayers of a biomembrane, the investigation of the elusive role of the Gaussian rigidity in different fundamental membrane processes (like budding and lateral sorting), and moreover, the postulation and investigation of a new model for pattern formation in biological tissues, leading to experimental evidences for a new key mechanism for symmetry break in *Hydra* polyps.

ZUSAMMENFASSUNG

Dünne, elastische Oberflächen stellen einen fundamentalen Baustein jedes biologischen Systems dar. Ihre Hauptvertreter auf kleiner Skala sind Biomembranen, ein wichtiges Beispiel auf größerer Skala sind Zellgewebe. In beiden Fällen definieren diese Oberflächen mechanische und chemische Grenzen, unverzichtbar für die Entstehung und Aufrechterhaltung eines jeden Organismus. Eine wesentliche Eigenschaft dieser Oberflächen sind dabei laterale Inhomogenitäten, die die komplexe Vielfalt an Formen, mechanochemischen Eigenschaften und Dynamiken erst ermöglichen.

Im Rahmen der vorliegenden Arbeit werden kontinuierliche mechanobiologische Modelle dieser Oberflächen entwickelt. Da Membranen und Zellgewebe experimentell oft nur schwer zugänglich sind, kann deren Verhalten auf diesem Wege theoretisch studiert werden. Die entwickelten mathematischen Modelle sind als gekoppelte nicht-lineare Systeme partieller Differentialgleichungen (PDE) vierter Ordnung gegeben. Um Simulationen der Modelle zu ermöglichen, werden numerische Verfahren, die auf der Finiten-Elemente Methode (FEM) basieren, deutlich erweitert.

Extensive systematische Simulationen der verschiedenen Modelle in Engführung mit bisherigen experimentellen und theoretischen Studien unterschiedlicher Skalen führen zu neuen Erkenntnissen in der Membran- und Gewebeforschung. Zentrale Erkenntnisse sind die Postulation und Charakterisierung neuartiger Mechanismen der Kommunikation zwischen den beiden Monolayern einer Biomembran, die Untersuchung der bisher unbekannt Rolle der Gauss'schen Biegesteifigkeit in verschiedenen fundamentalen Membran-Prozessen (wie Knospung und lateraler Organisation), sowie die Postulation und Analyse eines neuartigen Modells für die Gewebe-Musterbildung während der Embryogenese, was zu experimentellen Hinweisen auf einen bisher unbekannt Schlüsselmechanismus für den Symmetriebruch in *Hydra*-Polypen führt.

TABLE OF CONTENTS

| | |
|--|-----|
| ABSTRACT | i |
| LIST OF APPENDICES | vii |
| RELATED PUBLICATIONS | ix |
| CHAPTER | |
| I. Introduction | 1 |
| 1.1 Outline of the Thesis | 2 |
| II. Mathematical Modeling | 7 |
| 2.1 Biological, Biomechanical and Biochemical Background | 7 |
| 2.1.1 Membranes | 7 |
| 2.1.2 Tissues | 8 |
| 2.2 Thermodynamics | 10 |
| 2.2.1 Free Energy of a System | 10 |
| 2.2.2 Mechanical Forces | 11 |
| 2.2.3 Chemical Forces | 12 |
| 2.3 Previous Theoretical Approaches | 12 |
| 2.3.1 Membranes | 14 |
| 2.3.2 Tissues | 17 |
| 2.4 Mathematical Model | 19 |
| 2.4.1 Model Free Energy | 19 |
| 2.4.2 Dynamical Equations | 20 |
| 2.4.3 Statement of the Main Result | 21 |
| 2.4.4 Proof of the Main Result | 23 |
| 2.5 Nondimensionalization | 24 |
| 2.5.1 Free Energy | 24 |
| 2.5.2 Dynamics | 25 |
| III. Finite Element Approximation | 27 |
| 3.1 Mixed Formulation | 27 |
| 3.2 Analytical Reformulations | 27 |
| 3.3 Finite Element Discretization | 29 |

| | | |
|-------------------------|--|------------|
| 3.3.1 | Discretized Dynamical Equations | 30 |
| 3.4 | Tangential Grid Control | 33 |
| 3.5 | General Simulation Behavior | 34 |
| 3.5.1 | Simulation of a Membrane Patch | 34 |
| 3.5.2 | Correcting Advection of ϕ | 35 |
| 3.5.3 | Convergence Verification | 36 |
| 3.5.4 | Qualitative Sensitivity Analysis | 38 |
| 3.5.5 | Quantitative Sensitivity Analysis | 38 |
| IV. | Applications | 41 |
| 4.1 | A Multiscale Approach Investigating Curvature Modulated Sorting in Membranes | 43 |
| 4.1.1 | Introduction | 43 |
| 4.1.2 | Mathematical Model | 43 |
| 4.1.3 | Finite Element Approximation and Parameter Setup | 45 |
| 4.1.4 | Upscaling and Numerical Results | 46 |
| 4.1.5 | Discussion | 54 |
| 4.2 | Impact of Elastic Parameters on Membrane Budding | 57 |
| 4.2.1 | Introduction | 57 |
| 4.2.2 | Finite Element Approximation and Parameter Setup | 57 |
| 4.2.3 | Numerical Results | 59 |
| 4.2.4 | Discussion | 69 |
| 4.3 | Lateral Sorting and Transversal Communication in Coupled Mono- layers | 70 |
| 4.3.1 | Introduction | 70 |
| 4.3.2 | Mathematical Model | 70 |
| 4.3.3 | Nondimensionalization | 76 |
| 4.3.4 | Finite Element Approximation and Parameter Setup | 76 |
| 4.3.5 | Numerical Results | 77 |
| 4.3.6 | Discussion | 80 |
| 4.4 | On the Coupling of Tissue Mechanics with Morphogen Expression: A New Model for Early Pattern Formation in <i>Hydra</i> Polyps | 84 |
| 4.4.1 | Introduction | 84 |
| 4.4.2 | Mathematical Model | 85 |
| 4.4.3 | Nondimensionalization | 87 |
| 4.4.4 | Finite Element Approximation and Parameter Setup | 88 |
| 4.4.5 | Numerical Results | 88 |
| 4.4.6 | Discussion | 91 |
| V. | Summary and Outlook | 93 |
| APPENDICES | | 99 |
| BIBLIOGRAPHY | | 119 |
| ACKNOWLEDGEMENTS | | 141 |

LIST OF APPENDICES

Appendix

| | | |
|----|---|-----|
| A. | Notation | 101 |
| B. | Transition Between Sharp and Diffuse Line Tension | 103 |
| C. | Technical Remarks | 105 |
| D. | Fréchet Derivatives | 107 |

RELATED PUBLICATIONS

- MERCKER M, HARTMANN D, ŽIGMAN M, MARCINIAK-CZOCHRA A (2011)
On the coupling of tissue mechanics with morphogen expression: A new model
for early pattern formation in *Hydra* polyps, in preparation
- MERCKER M, RICHTER T, HARTMANN D (2011) Impact of elastic parameters
on membrane shape and budding transition, in review in Physical Review E
- MERCKER M, PTASHNYK M, KÜHNLE J, HARTMANN D, WEISS M, JÄGER
W (2011) A multiscale approach to curvature modulated sorting in biological
membranes, in review in the Journal of Theoretical Biology
- MERCKER M, RICHTER T, HARTMANN D (2011) Sorting mechanisms and com-
munication in phase separating coupled monolayers, Journal of Physical Che-
mistry B, 115(40), pp 11739-11745
- MERCKER M, MARCINIAK-CZOCHRA A, HARTMANN D (2011) A continuous
mechanobiological model of lateral inhomogeneous biological surfaces, in review
in the Journal of Mathematical Biology

CHAPTER I

Introduction

Elastic surfaces with large lateral dimensions but with a relatively small thickness are one of the basic building blocks of many structures in biology. One example is provided by biological membranes, which define a mechanical boundary of cells as well as of substructures inside cells. The lateral extension of these structures is usually up to a few micrometers, whereas the thickness of a membrane is only a few nanometers. Another example on a larger scale is cell tissue. For example, the early human embryo is 100 micrometers in diameter, but the thickness of its cell tissues is only a few micrometers. In both, membranes and cell tissues, it has been proved that lateral inhomogeneous distribution of molecules influencing the mechanical properties of the corresponding surfaces is essential for the genesis and maintenance of biological structures: in membranes, it has been shown that lateral phase separation of lipid molecules can lead to vesicle budding [18] (c.f. FIG 1.1 A-B). Furthermore, it has been suggested that lateral organization in membranes is a necessary condition for biogenesis and maintenance of cellular membrane systems themselves [175]. Thus, lateral organization in biological membranes is critical for the function of each biological cell. In cell tissues, it has been shown that lateral patterns of certain molecules, called morphogens, organize tissue morphology in the embryo; the process which is indispensable for development of any organ [200] (c.f. FIG 1.1 C-D).

In order to understand the complexity and variety of patterns, functions and dynamics of biological surfaces many different experimental model systems for membranes as well as for tissue-morphogenesis have been developed and used in the past ([18, 114, 172, 203, 245, 264], among many others). But in both, membranes and tissues, experimental techniques are subject to strong limitations, such as unmanageable complexity or limits of microscopy. To overcome these general experimental limitations, it is necessary to develop theoretical models, allowing e.g. to vary geometry, size and composition in a well defined way [43]. A strong synergy between theoretical models, their simulations and experimental approaches is assumed to be a major driver in the biomechanical research of biological surfaces [43, 85]. This thesis deals with the mathematical derivation of corresponding models, their numerical approximation and detailed simulation studies of the new models for different types of lateral inhomogeneous biological surfaces.

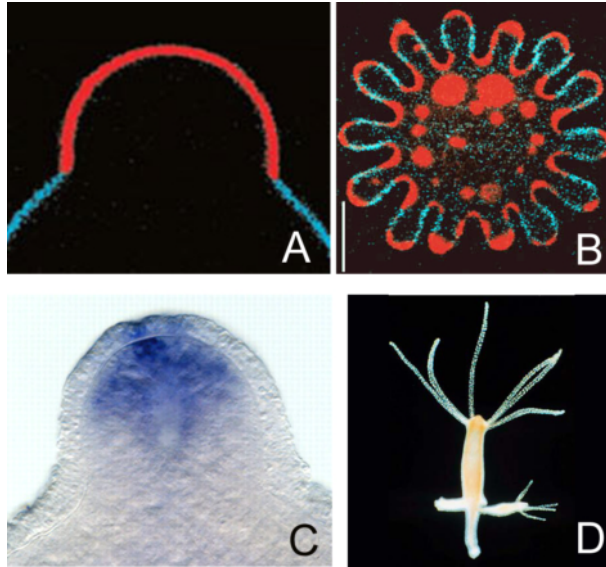


Figure 1.1: Prominent examples of deforming thin biological surfaces due to lateral inhomogeneities, at different levels of complexity. A-B: Biomembrane, two-photon microscopy image, red and blue color depict different membrane components, respectively (reprinted by permission from Macmillan Publishers Ltd: Nature, [18], © 2003). C-D: Tissue of *Hydra* polyps, light-microscopical images. C: Tissue during bud formation; blue color depicts expression of the morphogen *Wnt* (reprinted by permission from: Development, [106], © 2006); D: *Hydra*-polyp with budding miniature adults in the body wall (reprinted by permission from [111]).

1.1 Outline of the Thesis

This thesis is organized as follows: embedded in the context of related experimental results and previous modeling work, we first formulate a general mathematical model for the evolution of thin biological surfaces, using the example of biomembranes. Based on this, we subsequently develop a computational framework, enabling numerical simulations of the presented model. Furthermore, we apply the presented model and its modifications to investigate open questions in the field of mechanobiology, always in close relation to recent experimental and theoretical results. Various new insights into the mechanisms of deformations and pattern formation in biological membranes and tissues are gained, summarized at the end of the thesis. Finally, an outlook is presented, embedding the presented results in a possible future work.

For convenience of the reader, all mathematical notations and definitions as well as some additional remarks and information are given in Appendix A-D. Readers not interested in mathematical details, but in simulation results closely connected to biological processes, may skip Chapter II-III.

Chapter II: Mathematical Modeling

In this chapter, we first give an introduction of the biological background of membranes and tissues, the two most prominent examples of thin lateral inhomogeneous biological surfaces. Then we introduce the basic expressions and relationships of thermodynamics, constituting the fundament of our framework. We subsequently summarize previous modeling approaches in the field of membrane and tissue mechanics, including discrete as well as continuous approaches.

We recapitulate and generalize a mathematical model proposed in [163], which describes the dynamics of deforming lateral inhomogeneous biomembranes. (Our generalized model is from now on termed as the "basic model"; for modifications of this model leading to a description of biological tissues, we refer to Section 4.4.) In agreement with experimental observations, the model membrane consists of different molecular species undergoing lateral phase separation and influencing the mechanical properties of the membrane. More specifically, it accounts for line tension, for a monolayer area difference and for differences in spontaneous curvature, bending rigidity as well as Gaussian rigidity between the coexisting phases. The presented parametric 3D model is based on the minimization of a free energy leading to a nonlinear PDE system of fourth order, related to the Willmore flow and the Cahn-Hilliard equation. In order to enable a parameterization of independent parameters the model is nondimensionalized in the last section of Chapter II.

Chapter III: Finite Element Approximation

Here, we present the numerical approximation for the model equations (derived in Chapter II) using the finite element method (FEM): first, we analytically reformulate the model equations, in order to obtain a system of equations appropriate for a finite element discretization. In the subsequent sections, we present the detailed time and space discretization technique, since the considered parametric geometric differential equations require a non-standard approach. The numerical approach is based on a mixed finite element method combined with a semi-implicit Euler time-stepping scheme.

In the end of this chapter, we study the properties of the numerical approximation of the basic model (derived in Chapter II), including convergence verification of our approximations and relevant geometric quantities as well as a qualitative and quantitative sensitivity analysis.

Up to our knowledge, we present for the first time a parametric finite element approach describing realistic dynamics of lateral inhomogeneous biological membranes, neither restricted to axially symmetric geometries nor to small curvatures.

Chapter IV: Applications

In this chapter, the basic model and its modifications are used to study fundamental mechanochemical processes in biological surfaces using numerical simulations in comparison with recent experimental and theoretical results. We first consider deformations, sorting and communication in biological membranes (Section 4.1-4.3), but finally adopt our model to investigate pattern formation in the genesis of biological tissues as well (Section 4.4).

Section 4.1: A Multiscale Approach Investigating Curvature Modulated Sorting in Membranes

Connecting different theoretical approaches, in this section we investigate curvature modulated sorting in lipid bilayers fixed on non-planar surfaces. Adopting a truly multiscale approach, we use data from dissipative particle dynamics (DPD) to parameterize the continuous model, i.e. to derive a corresponding macroscopic model.

Our model predicts that curvature modulated sorting can occur if lipids or proteins differ in at least one of their macroscopic elastic moduli. Gradients in the spontaneous curvature, the bending rigidity or the Gaussian rigidity create characteristic (metastable) curvature dependent patterns. The structure and dynamics of these membrane patterns are investigated qualitatively and quantitatively using simulations. These simulations show that the decomposition time decreases and the stability of patterns increases with enlarging moduli differences or curvature gradients. Presented phase diagrams allow to estimate if and how stable curvature modulated sorting will occur for a given geometry and set of elastic parameters.

In addition, we find that the use of upscaled models is imperative studying membrane dynamics. Compared with common linear approximations, the system can evolve into different local minimum patterns. This emphasizes the importance of parameters and realistic dynamics in mathematical modeling of biological membranes.

Section 4.2: Impact of Elastic Parameters on Membrane Budding

Dynamic deformations of membranes, like budding, play a crucial role in many healthy and pathogenic cellular processes. It has been shown that lateral phase separation of different membrane components locally influencing membrane mechanics plays a key role in these processes.

Here, we use our basic mechanobiological model to investigate numerically the deformations of incompressible lateral phase separating two-component membranes. We perform systematic simulations to study the impact of the elastic parameters on membrane shape and budding, e.g. the impact of the line tension, monolayer area difference as well as differences in spontaneous curvature, bending rigidity and Gaussian rigidity between the coexisting phases. The impact of each elastic parameter fits qualitatively and quantitatively well with recent experimental and theoretical (sharp

line tension) results. Furthermore, we find that changes in each of the elastic parameters can be used to prevent or induce membrane budding. To our knowledge, we prove for the first time that the Gaussian rigidity plays a role qualitatively comparable to the impact of the other elastic parameters on dynamics and minimum shapes of the budding process.

Section 4.3: Lateral Sorting and Transversal Communication in Coupled Monolayers

A continuous model of two coupled monolayers constituting a fluid bilayer membrane is presented. The model is based on the minimization of a membrane free energy considering in both monolayer leaflets two different molecule types, undergoing lateral phase separation. Differences in the mechanical properties of the molecules, such as shape, stiffness and length, are considered explicitly by the model. In the presented model, we couple between the monolayers using an energy based model depending on the local distance between the two monolayers as well as the lengths of molecules constituting the local monolayer region.

We numerically study different passive mechanisms for molecule sorting and correlation across the bilayer induced by first order mechanical constraints. Here, we focus on three aspects: first, we find that the stretching of the two monolayers in the normal direction yields a sorting of molecules according to their length. Furthermore, we show that the length of molecules can be used to synchronize phases across the bilayer membrane. Moreover, we find that generating curvature in one layer (induced by different curvature creating mechanisms) sorts molecules of the other layer according to their shape and stiffness.

Many recent experimental data indicate the importance of specific lipid-protein interactions and the role of the bilayer thickness in membrane protein function and sorting. The presented model proposes different mechanisms leading to a co-localization of different components in different monolayers at the same place at the same time.

Section 4.4: On the Coupling of Tissue Mechanics with Morphogen Expression: A new Model for Early Pattern Formation in *Hydra* Polyps

Morphogens are small molecules, which regulate and coordinate different steps in the morphogenesis of cell tissues. It has been shown that in many cases morphogen dynamics are well described by the Turing mechanism, which induces pattern formation. However, in several other cases this mechanism seems to be unlikely, e.g. if strong tissue deformations are involved.

Based on recent experimental findings, we propose in this section a simple non-Turing type model for pattern formation, in which the tissue curvature is coupled with the morphogen expression. We show numerically that the presented model leads to a variety of morphogen and curvature patterns, which appear to be insensitive

to different stochastic initial conditions. Extensive simulations are used to identify important parameters in the control of characteristic pattern properties, such as size and number of appearing buds. Our results suggest that biomechanical interactions may replace the "missing" long range inhibitor in the process of Turing type pattern formation.

Comparing our simulations with recent experimental data, we propose the presented model as a possible key mechanism for symmetry break and early pattern formation in *Hydra*-reaggregates. However, experimental evidences are still weak. Hence, novel experimental approaches will be necessary to test our central assumption, which is: tissue curvature and morphogen expression are coupled in a positive feedback loop.

CHAPTER II

Mathematical Modeling

Membranes and cell tissues, the two main representatives of thin biological surfaces, share many biomechanical properties at first sight. However, there are key differences in their composition, in relevant scales as well as in their biological function. Let us give an example: both resist normal deformations in an elastic manner, but lateral dynamics are significantly different: the molecules constituting the mechanical membrane surface change their neighbors very fast, i.e. represent a "lateral fluid". On the contrary, cells constituting the mechanical tissue surface do not change their neighbors and could be considered as an elastic body (at least on small time scales) but molecules within the cells and tissues can show different and fast lateral dynamics. Because of these fundamental differences, in the following we will explicitly distinguish between membranes and cell tissues, if necessary.

2.1 Biological, Biomechanical and Biochemical Background

In this section, we present the mechanochemical properties, the biological functions as well as related experimental findings concerning membranes and cell tissues.

2.1.1 Membranes

Biological cells are composed by a multitude of membrane systems (c.f. FIG 2.1). Each of these systems provides a specific environment for certain chemical and mechanical processes. Lipid molecules (lipids) are the main component of membranes. In water, due to hydrophobic interactions, lipids form a bilayer structure consisting of two lipid monolayers, physically opposed to each other (c.f. FIG 2.4). In contrast to an elastic behavior with respect to bending, membrane molecules can move freely in lateral direction of the membrane. Therefore its lateral behavior can be compared to a two-dimensional (2D) fluid, first described in the "fluid mosaic" model by Singer [228]. In living cells, biological membranes are composed of many different lipids, proteins and other molecules with various functions [4]. Internal cellular membrane systems permanently change their shape, lateral composition and hence their mechanochemical properties - during the cellular genesis as well as in adult cells. This

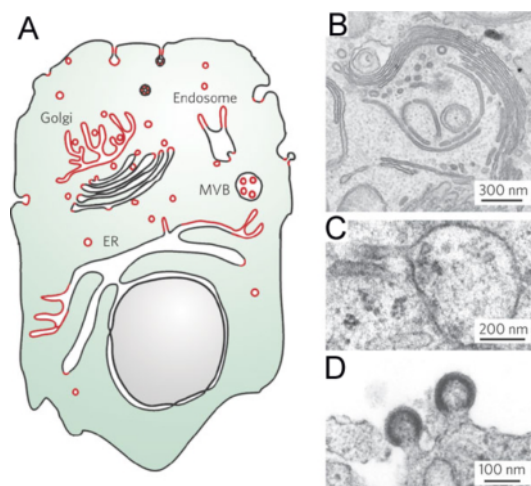


Figure 2.1: Biomembranes. A: Diagram of different cellular membrane systems. Regions with local high curvature are marked in red. B-D: Different sample electron micrographs on different scales (reprinted by permission from Macmillan Publishers Ltd: Nature, [161], © 2005).

constant dynamic membrane remodeling is indispensable for the communication between the different membrane systems as well as for other fundamental processes such as movement, division and vesicle trafficking [161], but also during infections [16, 249].

Different molecules responsible for dynamical cell remodeling are well characterized from a biological point of view [26, 154, 161, 243, 269]. However, details of the mechanochemical dynamics and steady states, leading to the impressive diversity of membrane shapes and composition patterns on larger scales, are far away from being understood. Especially the resolutional limits of microscopical techniques strongly restrict experimental studies to certain spatial scales. Hence, processes taking place on smaller scales need to be investigated theoretically. An additional problem of experimental techniques is the degree of complexity. In most of the cases, the exact mechanochemical properties of single components are neither known nor possible to be controlled or changed in a defined way. Hence, a strong synergy between simulations on all length scales and experiments is a major driver in the field of membrane research [43].

2.1.2 Tissues

Life is based on a hierarchy of structured levels, where each level is based on the level beneath [40]. On the (sub-)cellular level, biological membranes are defining boundaries, enabling the diversity of chemical and mechanical reactions. On the larger level, thin cell tissues undertake this task. As opposed to membranes, local chemical and mechanical properties of adult tissues do not change very much, most striking conformational changes take place during tissue morphogenesis.

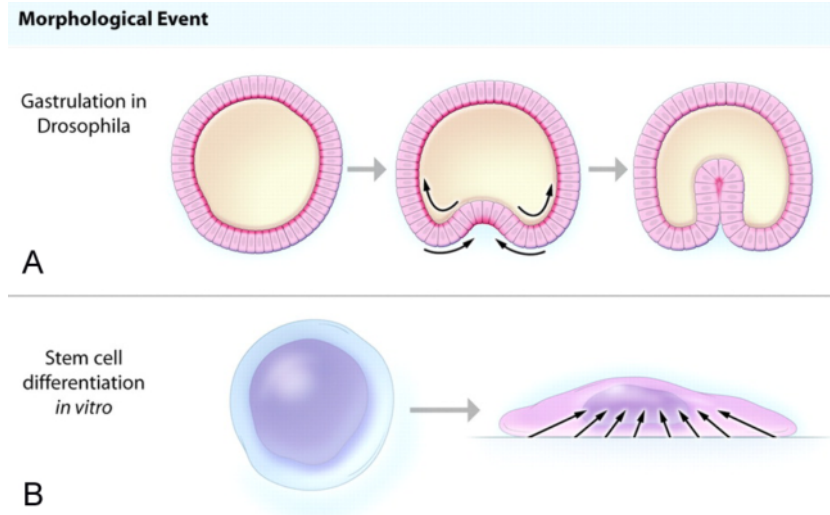


Figure 2.2: Cell tissues. A: *Drosophila*-tissue morphogenesis due to shape changes of single cells. B: Example of a single cell shape change. (Both pictures reprinted by permission from Wolters Kluwer Health: Circulation Research [194], © 2008.)

In order to change or/and keep its (e.g. mechanical) properties, each cell is able to produce a certain set of small molecules, called proteins [4]. Patterns and dynamics of protein production thereby depend on various stimuli, where proteins can directly or indirectly influence the production of other proteins in turn; all in all a network of unimaginable complexity [10]. Furthermore, proteins can move inter- and intracellularly, observed processes are reaching from simple diffusion up to highly specialized active transport [246].

It has been shown that certain proteins, conceptually termed as "morphogens", are responsible for pattern formation in tissue development and morphogenesis. Quite a few of these patterns have been explained by a mechanism discovered by Alan Turing [241], assuming a certain type of reaction-diffusion system. But in many other cases - especially when dynamic tissue deformations are involved - the molecular mechanisms seem to be different [66].

Recent experiments show that the mechanics of biological cells and tissues as well as their pattern formation, in interplay with morphogen dynamics, involve many complex biological processes [34, 66, 88, 106, 115, 182, 194] which have been only partially discovered. Furthermore, since living material is investigated, experimental requirements are quite sophisticated and experimental techniques are subject to strong limitations.

In order to avoid these limitations and the unmanageable order of complexity in experimental tissue mechanics, first theoretical model systems have been developed within the last years, considering explicitly the interplay of morphogens and tissue mechanics (c.f. Section 2.3.2). A further development of theoretical models could be

the future driver to study and filter fundamental biological mechanisms determining curvature and morphogen patterns during tissue development.

2.2 Thermodynamics

In this section, we will give an introduction to the most important definitions, quantities and relationships from the standpoint of classical thermodynamics. Since, within this work, thin biological surfaces are considered as thermodynamical systems, this introduction is the fundament for the presented modeling approach.

2.2.1 Free Energy of a System

We consider a deforming elastic surface, which is embedded in a fluid. With an appropriate choice of boundary conditions (or a closed surface), this surface depicts a closed thermodynamical system. It means that the system always contains the same amount of matter but heat (and work) can be exchanged via dissipation through the fluid. Since this transfer is possible, the total internal energy U of the surface can change due to the first law of thermodynamics. The "principle of minimum potential energy" states that the internal energy decreases in time, and that this energy approaches a minimum value at thermodynamical equilibrium - if the entropy S of the system is constant. The loss of energy can be explained by the dissipation.

If we consider the deformation of an elastic surface, it can be sufficient to take into account this total internal energy U with constant entropy S . However, e.g. if molecules are able to change places with their neighbors (like in the case of laterally free moving membrane molecules), the entropy S can change, what should be considered as well. Hence, due to the second law of thermodynamics, the thermodynamical equilibrium of the system is given by two conditions: minimal inner energy but maximal entropy.

For practical considerations and in experimental observations it is rarely possible and convenient, to distinguish between entropically and energetically dominated effects. Hence, a state function F (termed as the free energy) is typically introduced, governing both effects in a phenomenological way if the system has many degrees of freedom e.g. many particles which are impossible to be tracked individually. The Helmholtz-free energy may provide an adequate statistical description (that allows for the determination of mean quantities and fluctuations). This free energy is given by

$$F = U - TS,$$

where T is the thermodynamic temperature. In that way, the minimum of F represents the optimal (equilibrium) state for each mechanical or chemical system, combining a minimal internal energy with a maximal entropy. For further details of the nature of free energy and entropy, we refer to [232].

2.2.2 Mechanical Forces

For each moving particle within a thermodynamical system, the force field acting on this particle can be seen as the tendency of the system to approach a minimum of its free energy. In this section, we consider the same elastic mechanical forces in the framework of biological surfaces: given a closed surface Γ with a free energy functional F and let $\vec{A}(\vec{X}, t) \in \mathbb{R}^3$ be the force acting on Γ at \vec{X} at time t . We assume that the force is determined by the variation F' in form of the following elastic L^2 -gradient flow

$$\int \vec{A} \cdot \vec{\psi} ds = -\langle F', \vec{\psi} \rangle = - \left. \frac{d}{d\epsilon} [F(\vec{X} + \epsilon\vec{\psi})] \right|_{\epsilon=0}, \quad (2.1)$$

where $\vec{\psi} \in C^\infty(\Gamma, \mathbb{R}^3)$ is an arbitrary test function. (For notational clarity, here and in the following we use square brackets for differential operators.) Since (2.1) holds for all $\vec{\psi}$, let us consider the decomposition into the tangential and normal parts $\vec{\psi} = \psi\vec{n} + \sum_k \psi^k \partial_k \vec{X}$ and $\vec{A} = -A^\perp \vec{n} - \sum_u A^u \partial_u \vec{X}$. It follows:

$$\begin{aligned} \int_{\Gamma} \vec{A} \cdot \vec{\psi} ds &= - \int_{\Gamma} (A^\perp \vec{n} + \sum_u A^u \partial_u \vec{X}) \cdot \psi \vec{n} ds \\ &\quad - \int_{\Gamma} (A^\perp \vec{n} + \sum_u A^u \partial_u \vec{X}) \cdot \left(\sum_k \psi^k \partial_k \vec{X} \right) ds \\ &= - \int_{\Gamma} A^\perp \psi ds - \sum_{u,k} \int_{\Gamma} A^u \partial_u \vec{X} \cdot \partial_k \vec{X} \psi^k ds, \end{aligned}$$

as well as

$$\begin{aligned} \langle F', \vec{\psi} \rangle &= \langle F', \psi \vec{n} \rangle + \langle F', \sum_k \psi^k \partial_k \vec{X} \rangle \\ &= \left. \frac{d}{d\epsilon} F(\vec{X} + \epsilon \psi \vec{n}) \right|_{\epsilon=0} + \left. \frac{d}{d\epsilon} F(\vec{X} + \epsilon \sum_k \psi^k \partial_k \vec{X}) \right|_{\epsilon=0}. \end{aligned}$$

In the following, δ^\perp and δ^k depict the variation in the normal direction and the k -th tangential direction ($k = 1, 2$) with respect to Γ , respectively, where $\delta^t = \sum_k \delta^k$.

In friction dominated regimes, the surface velocity is often assumed to be proportional to the force [15, 211, 237], hence $\partial_t \vec{X} = L_X \vec{A}$, where L_X is a damping coefficient. It follows

$$\partial_t \vec{X} = -L_X \frac{\delta F}{\delta \vec{X}}, \quad (2.2)$$

where $\frac{\delta F}{\delta \vec{X}}$ denotes the strong and pointwise formulation of the variation $\left. \frac{d}{d\epsilon} [F(\vec{X} + \epsilon\vec{\psi})] \right|_{\epsilon=0}$.

One should notice that such a gradient flow approach often finds only stable local minima. But it has been shown to be also very effective in solving numerically models of thin biological surfaces [155, 237, 248].

In the case $\vec{A} = 0$, the minimum of F has been reached. In this case, equation (2.1) depicts an Euler-Lagrange equation, representing the equilibrium shape of the considered surface.

2.2.3 Chemical Forces

In chemical solutions where molecules can change their neighbors, the chemical potential μ is the quantity describing a force field being the cause of molecular movement. Thus, μ can be characterized as "the tendency of particles to diffuse" [13]. Let us consider a lateral inhomogeneous surface Γ with a free energy functional F , where ϕ describes the volume fraction of particles in the surface. Analogously to elastic forces (c.f. previous section), μ depends on the derivative of the free energy F with respect to ϕ . In that way, μ induces (lateral) diffusion, minimizing F with respect to ϕ . Hence [13, 121],

$$\mu = \frac{\delta F}{\delta \phi},$$

where $\frac{\delta F}{\delta \phi}$ depicts the strong and pointwise formulation of the variation $\frac{d}{d\epsilon} [F(\phi + \epsilon\psi)]|_{\epsilon=0}$.

Neglecting local mass conservation the diffusion velocity is assumed to be proportional to μ (analogous to equation (2.2)). It follows the Landau-Ginzburg type equation [11, 168, 242]

$$d_t \phi = -L_\phi \frac{\delta F}{\delta \phi},$$

where L_ϕ is a diffusion coefficient. In case of local mass conservation, the equation

$$d_t \phi = -L_\phi \Delta \left[\frac{\delta F}{\delta \phi} \right]$$

has been proposed [38, 185]; for a more detailed derivation of this equation we refer to Section 2.4.2 and [31]. For more details on the nature of the chemical potential we refer to [13, 121].

2.3 Previous Theoretical Approaches

To model biological surfaces, two main fundamental approaches have been used in the past: discrete models and continuous approaches. In the case of discrete models, reasonable discrete subunits of the system of interest and their interactions are

considered. Regarding membranes, usually simplified membrane molecules have been used [112, 214], whereas in the case of tissues, single cells depict meaningful subunits [53]. While using discrete approaches, a detailed consideration of surface behavior on small scales is assured. However, the disadvantage is the increasing computational cost for larger systems. This restricts discrete modeling approaches, e.g. particle based membrane studies, to system sizes and times still far away from biologically relevant scales [36].

In contrast, continuous models are not discretized until they are numerically approximated. Hence, the scale of consideration can be controlled and the computational costs (corresponding to the level of discretization) do not scale with the number of subunits, but the spatial and temporal resolution of the system. Furthermore, continuous descriptions of deforming surfaces allow a more appropriate coupling of mechanics with chemical processes. This is e.g. based on the fact that many biochemical processes have been already described via continuous formulations [38, 156, 168, 241].

Based on this knowledge, we will develop continuous models to describe the deformation of lateral inhomogeneous biological surfaces in this thesis. Nevertheless, to take into account molecular properties, data from discrete approaches are used to parameterize the presented continuous models, i.e. to derive macroscopic formulations based on microscopic models (c.f. Section 4.1).

Thin lateral homogeneous layers bend elastically and in the linear regime are well described by the plate equation [49], idealizing the layer by a two-dimensional (2D) bent surface. This idea was further developed by Helfrich [108], describing the stable shape of a 2D surface by considering the minima of the classical bending energy

$$F_{\text{Helfrich}} = \int_{\Gamma} \frac{\kappa}{2} (H - H_0)^2 ds + \int_{\Gamma} \kappa_G K ds. \quad (2.3)$$

Here, ds denotes the surface measure, H the mean curvature and K the Gaussian curvature, both depending on the geometry of the surface Γ [64]. If C_1 and C_2 are the two principal curvatures, H is defined as their sum and K as their product (see also FIG 2.3). H_0, κ, κ_G are the elastic moduli, which are constant if the surface is laterally homogeneous. H_0 is the spontaneous curvature and represents the preferred curvature in the relaxed state. It is nonzero if, for example, membrane molecules or cells are wedge-shaped. Parameters κ and κ_G are respectively the bending rigidity and the Gaussian rigidity. Both parameters represent the stiffness of the surface: in tubular structures (where K vanishes; c.f. FIG 2.3 B) κ penalizes curvatures; in saddle structures (where H vanishes; c.f. FIG 2.3 A) κ_G penalizes curvatures. In case of $\kappa = 1$ and $H_0 = 0$, the L^2 -gradient flow of (2.3) is known as the Willmore flow [250]. Since most of the geometries appearing in biological layers exhibit various structures intermediate between saddles, tubes and spheres (FIG 2.3 A-C), in the majority of cases both moduli contribute to the energy penalty of curved surfaces. In

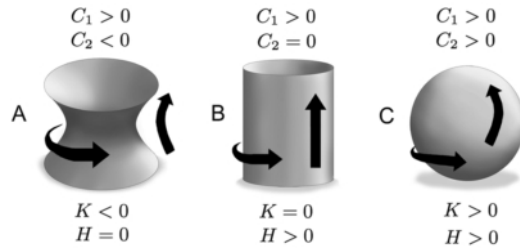


Figure 2.3: Principal curvatures C_1, C_2 , mean curvature $H = C_1 + C_2$ and Gaussian curvature $K = C_1 C_2$ for different geometries: (A) Saddle, (B) Tube, (C) Sphere.

this context we would like to mention the well known Gauss-Bonnet theorem stating that for closed surfaces Γ the integral $\int_{\Gamma} K ds$ is a constant, depending only on the topology of Γ .

Before we present in detail our basic mathematical model based on equation (2.3), we want to summarize previous theoretical approaches in the modeling of biomembranes and biological tissues.

2.3.1 Membranes

The complexity of real biological membranes has motivated the development of various different theoretical membrane models, to allow to vary geometry, size and composition in a well defined way [35, 43]. The most basic theoretical approaches to membranes are atomistic as well as coarse grained molecular dynamical approaches [92, 99]. They allow to investigate different magnitudes of the molecular scale, and have been used to study different fundamental processes such as endocytosis [265], rupture [183, 256], fission [229], lipid flip-flop [201], membrane protein diffusion [173, 215], vesicle shapes and transition [157, 158, 159, 253] as well as budding [56, 112, 132, 252], domain formation [117, 137, 214, 222] and the thermoelastic properties of bilayers depending on molecular properties [29, 55, 138, 188, 190].

Unfortunately, molecular dynamical approaches are not suited to study membrane behavior on time and space scales, where most of important cellular processes take place: in various experimental studies on biological membranes, it has been shown that relevant scales of fundamental processes are in the range of micrometers and seconds [6, 18, 67, 94, 96, 122, 170, 193, 254]. However, molecular dynamical approaches are still restricted to membrane sizes of tens of nanometers and times of hundreds of nanoseconds [36]. Although different solvent-free approaches have been developed to reduce the computational cost [54, 56, 183, 205, 265] it seems to be unlikely that these restrictions will change very much within the next decades [29].

To investigate larger scales and to compare experiments with analytical estimates, different continuous approaches have been developed in the past [35, 36, 218]. Mainly based on the minimization of the Helfrich free energy [108] (c.f. equation (2.3)), dif-

ferent properties and processes of homogeneous membranes have been investigated: interaction between different membranes [100], flux through semipermeable membranes [113] as well as the impact of different elastic parameters [39, 75, 76, 119], of the cytoskeleton [105], of temperature [151], of pressure [197, 266], of mechanical constraints [119, 169, 219] and of molecular properties [130, 208].

Biological membranes are typically very inhomogeneous structures, composed of different molecules. Molecule compositions can differ between the two monolayers as well as between different membrane systems. Furthermore, experimental data reveal that global surface areas between the two monolayers can differ, and that this area asymmetry has a striking influence on membrane morphology [174]. Mathematically, this affect has been first described using a hard constraint based on the bilayer-couple hypothesis [87, 221, 234], and later - more generally - by the area-difference-elasticity (ADE) model [169, 218]: in addition to the energy (2.3) depending on the local curvature, the effect of an area difference between the two monolayers is modeled in the ADE model considering the additional energy term

$$F_{\text{ADE}} = \frac{\bar{\kappa}}{2} \frac{\pi}{AD^2} (\Delta A - \Delta A_0)^2,$$

where $\Delta A \equiv A^{\text{out}} - A^{\text{in}}$ and $\Delta A_0 \equiv A_0^{\text{out}} - A_0^{\text{in}}$ depict the actual and the relaxed area difference between the two coupled monolayers, respectively. $A = \int_{\Gamma} ds$ is the total surface area (which is in case of lateral bilayer incompressibility a constant) and $\bar{\kappa}$ is an elastic parameter. The nonlocal term ΔA is related to the local curvature by

$$\Delta A = D \int_{\Gamma} H ds,$$

where D describes the distance between the two monolayers [169]. Note that the ADE model reduces for $\bar{\kappa} \rightarrow 0$ to the Helfrich model and matches for $\bar{\kappa} \rightarrow \infty$ with the hard constraint $\Delta A_0 = \Delta A$. Furthermore, values $\bar{\kappa} \neq 0$ presume local monolayer compressibility, since they describe an energetic penalty of the relative stretching and compression of the monolayers, which arise during membrane bending. However, this does not contradict to the assumption of bilayer incompressibility, since these contributions originate from splaying the molecules in the single monolayers and are of a much smaller order than lateral bilayer stretching [68].

In contrast to the elastic response with respect to bending, membrane molecules can move freely in the lateral direction of the membrane. Hence, its lateral behavior can be compared to a 2D fluids behavior [228]. In living cells, biological membranes are composed of many different lipids, proteins and other molecules with different functions [4]. For both lipids [18, 244] and proteins [26], the lateral phase separation and clustering have been shown. Mathematically, the concentration of two different laterally distributed components A and B in a surface Γ can be described by an order parameter (or phase-field variable) $\phi : \Gamma \rightarrow [-1, 1]$. That is, if $\phi = 1$ the membrane is locally composed purely of species A and if $\phi = -1$ locally only species

B is present. The lateral phase separation of an order parameter ϕ is well described by the minimization of the Cahn-Hilliard energy [38] on a surface

$$F_{\text{Cahn-Hilliard}} = \sigma \int_{\Gamma} \left(\frac{\xi^2}{2} (\nabla^{\Gamma} \phi)^2 + f(\phi) \right) ds, \quad (2.4)$$

where σ is the (diffuse) line tension, ξ the transition length, ∇^{Γ} the surface gradient, and f a double-well potential.

The first theoretical work in the field of membrane research considering the interplay of curvature generation and phase separation goes back to Lipowsky [150]. Since then a lot of efforts have been spent in studying membrane budding using continuous approaches based on the minimization of a free energy, consisting of different couplings of the two energy components (2.3) and (2.4). Early works have used phenomenological coupling terms [5, 8, 45, 120, 237, 260], whereas more recent works have derived the coupling terms directly from the first physical principles [83, 84, 155, 248]. The techniques used to describe the membranes range from parametric representations [83, 84, 120, 237] based on modeling membranes as continuous hypersurfaces, to phase field descriptions [155, 248], where membranes of a finite thickness are embedded in a surrounding fluid. The advantage of the parametric approach is the relatively low computational cost of simulations, since they are performed on a 2D surface embedded in a 3D space.

Based on a coupling between the Helfrich energy (2.3) and a Cahn-Hilliard type energy (2.4), various properties and processes of lateral inhomogeneous membranes have been investigated in the past, i.e. membrane budding and fission [5, 155, 171, 240], periodicity of lateral patterns [255], vesicle fission [47], curvature induced phase separation [217], domain-boundary interaction [71], phase separation under shear flow [48], and adhesion induced phase separation [128].

The first derivation of the homogeneous layer's free energy (2.3) has relied on a phenomenological approach [108]. Since then, different experimental and theoretical efforts have been made to derive its macroscopic elastic moduli directly from molecular properties [42, 133, 191, 208, 209, 235, 251]. However, most of these approaches are limited to the impact of selected molecule properties, special surface geometries, small curvatures, or consideration of one-dimensional (1D) curves. Furthermore, all these approaches consider lateral homogeneous surfaces. In reality, biological surfaces often display lateral inhomogeneities. Up to now, there exists no general approach determining directly from the molecular scale the elastic moduli for an arbitrary curved and inhomogeneous surface. Dynamics of inhomogeneous membranes depend strongly on the detailed relationship between mechanical moduli and the local composition of the membrane. A rigorous multiscale derivation of this relationship is an open problem and a rewarding target of research in applied mathematics.

In this thesis, we present different continuous models describing deformations in inhomogeneous membranes consisting of two components, using a parametric description of the membrane. The mechanical models are coupled with a diffuse model of lateral phase separation of the two components. Furthermore, we present a numerical approximation of these models, using the finite element approach. Although the models do not result from a rigorous upscaling from the molecular scale, the coupling between the energies (2.3) and (2.4) is based on first physical principles. All models take into account the observation that different molecules vary in their shape and stiffness. In contrast to the very recent works of Elliott and Stinner [83, 84], presented gradient flows are considered to be realistic models for the dynamics, and not only to generate equilibrium configurations. This has important mathematical consequences: e.g. we have to consider lateral surface deformations advecting local mass, combined with a local area constraint instead of a global constraint. Furthermore the dynamics for the order parameter are taken to be of a Cahn-Hilliard type rather than of a Allen-Cahn type as in [83, 84].

Considering realistic membrane dynamics is motivated by different reasons from a biological point of view: on the one hand, it appears that the use of different dynamics can trap the system in different local minimum patterns (c.f. Section 3.5.4 as well as Section 4.1). Hence, realistic dynamics for a system in membrane modeling are necessary to ensure biologically reasonable equilibrium configurations. On the other hand, cellular membrane systems are arranged in dynamic equilibrium rather than static configurations. Budding and fusion of membrane spheres occur with flux constantly maintaining the communication between subcellular membrane-bound systems [161]. Furthermore, there seems to be chemical control mechanisms, interacting with the membrane during the dynamics of fundamental processes [154]. Accordingly, within this thesis we consider realistic dynamics, in order to provide a model depicting a basis to describe these processes.

2.3.2 Tissues

During the embryogenesis, an initial homogeneous tissue sphere evolves up to a complex organism, finally showing various different chemical and mechanical patterns. Underlying spatial pattern generating mechanisms have been subject of much experimental and theoretical research [176, 179]. However, most of these processes are still unknown, although the mechanisms behind embryonic pattern formation appear to be one of the biggest current unsolved biological challenges [176].

First fundamental works in the theory of pattern formation in biological tissues have been achieved by Turing: he suggested that small molecules within the tissues (termed as morphogens, c.f. Section 2.1.2) can react and diffuse such that they produce spontaneously stable morphogen patterns without any initial prepattern [241]. The key mechanism beyond this process is the interaction between an activator and an inhibitor molecule in combination with diffusion ("diffusion driven instability")

[176]. It has appeared that there are experimental evidences for this mechanism and its modifications [162, 176] in many different tissue pattern formation processes ([25, 103, 224], among many others).

However, in many cases - especially if dynamic tissue deformations are involved - pure chemical mechanisms seem to be unlikely, suggesting that tissue mechanics is directly involved in pattern formation [66]. Although a mechanical theory for generating pattern and form in development has been developed during the last decades, mechanisms behind pattern establishment in the early embryo are still a field of active research [176]. Broadly speaking, the main mechanochemical approach during the last two decades explaining tissue pattern formation has constituted the Murray-Oster approach (e.g. [144, 177, 186, 189]). This approach considers the role mechanical forces play in the process of tissue pattern formation and has been applied to several specific developmental problems such as vasculogenesis [178] or skin patterns [57, 179, 180] and is experimentally well documented [178]. It considers cell pattern formation of moving cells within a substrate, usually describing cells by density functions, modeling the system as a planar 2D-surface.

However, tissue curvatures have not been considered explicitly in mechanochemical modeling of tissue pattern formation up to now - except very few approaches. Cummings has developed a mathematical fundament to describe the geometry of a surface with finite thickness, depending on two key morphogens [58, 59]. Furthermore, invagination processes in the *Drosophila* blastoderm have been studied numerically using a 3D finite element method [53] - but in both cases without considering any morphogen dynamics. Indeed, on the one hand, experimental evidences for genetic responses depending on tissue curvature have been discovered only very recently [34, 66, 88, 182]. On the other hand, mathematical models of evolving surfaces embedded in 3D-space are quite challenging: usually they consist of geometric nonlinear coupled partial differential equations of fourth order [163]. Up to now there seems to be no mathematical model and numerical approach describing pattern formation in biological tissues, explicitly accounting for tissue curvatures.

Within this thesis, we present for the first time (up to our knowledge) a non-Turing type dynamic mechanochemical model explicitly coupling tissue curvature with morphogen dynamics. Based on recent experimental findings, morphogen expression is coupled with tissue curvature in a positive feedback loop. Furthermore, we present a numerical approximation of our model equations using a finite element approach. We numerically show that the proposed model leads to stable patterns without any initial pre-patterns. Furthermore, we present experimental evidences showing that the presented mechanism could constitute a key mechanism for pattern formation in *Hydra* polyps.

2.4 Mathematical Model

In the following, we recapitulate and generalize a 3D mathematical model for dynamics of biological membranes [163], combining a parametric approach for the deforming surface with a diffuse approach for lateral dynamics. Derivations already presented in [163] have been shifted to the Appendix D and shortened significantly, for further details of the proofs we refer to [163]. (For a modification of this model describing deforming biological tissues, we refer to Section 4.4.)

The dynamic model presented in this section is based on the fundamental approaches of [38] and [108]. It is a generalization of many other continuum models in the field of membrane research [5, 45, 60, 83, 84, 120, 123, 150, 155, 237, 260]. In the proposed model, the bilayer is represented by a continuous two-dimensional (2D) surface Γ depicted by a parametric representation $\vec{X}(u_1, u_2) : U \rightarrow \Gamma \subset \mathbb{R}^3$ with e.g. $U = [0, 1] \times [0, 1]$, i.e. we adopt a Lagrangian point of view instead of an Eulerian point of view (typically adopted in phase field models [155]). Here, we focus on a membrane composed of two different lipid species (or alternatively one lipid and one protein species). The concentration of the two components A and B in Γ is described by the order parameter $\phi : U \rightarrow [-1, 1]$. That is, if $\phi = 1$ only species A is present and if $\phi = -1$ the membrane is locally purely composed of species A .

2.4.1 Model Free Energy

Our model is based on the minimization of the free energy $F = F_1 + F_2 + F_3 + F_4$ containing the curvature-dependent part $F_1 + F_2$, the Cahn-Hilliard energy F_3 inducing lateral phase separation as well as the area-difference-elasticity (ADE) term F_4 , which has not been considered in [163]. The energy components F_1 , F_2 , F_3 and F_4 are:

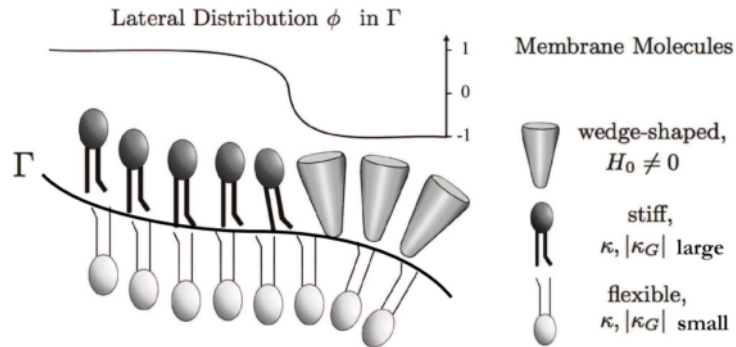


Figure 2.4: Continuous model bilayer membrane: the bilayer is represented by the surface Γ and its lateral inhomogeneity by the order parameter ϕ . Mechanical molecule properties are outlined on the right hand side.

$$\begin{aligned}
F_1 &= \frac{1}{2} \int_{\Gamma} \kappa(\phi) (H - H_0(\phi))^2 ds, \\
F_2 &= \int_{\Gamma} \kappa_G(\phi) K ds, \\
F_3 &= \sigma \int_{\Gamma} \left(\frac{\xi^2}{2} (\nabla^{\Gamma} \phi)^2 + f(\phi) \right) ds, \\
F_4 &= \frac{\bar{\kappa}}{2} \frac{\pi}{AD^2} (\Delta A - \Delta A_0)^2,
\end{aligned} \tag{2.5}$$

where for each $\vec{X} \in \Gamma$ the order parameter $\phi(\vec{X}(\vec{u}))$ is identified with $\phi(\vec{u})$. Since different components of the membrane may differ in their mechanical properties such as shape and stiffness, each macroscopic mechanical modulus h , $h \in \{\kappa, \kappa_G, H_0\}$, is a function of the order parameter ϕ . Each function h is chosen so that $h(1) = h^A$ and $h(-1) = h^B$, where h^A and h^B are the mechanical moduli of the pure components. Furthermore, σ is the line tension, ξ the transition length, ∇^{Γ} the surface gradient, f a double well potential, $A = \int_{\Gamma} ds$ the total surface area, ΔA and ΔA_0 represent the current and the relaxed monolayer area difference, respectively, D depicts the distance between the two monolayers and $\bar{\kappa}$ is a dimensionless parameter (c.f. Section 2.3.1).

2.4.2 Dynamical Equations

Instead of directly minimizing $F = F_1 + F_2 + F_3 + F_4$ we adopt a dynamic point of view considering the evolution of $\vec{X}(\vec{u}, t)$ and $\phi(\vec{u}, t)$ for $t \in [0, T)$. In a first step, let us consider the evolution of the species A and B within the membrane and in a second step the evolution of the membrane itself.

Assuming local mass conservation, lateral dynamics of the two species A and B in the framework of the Lagrangian description is determined by the lateral continuity equation

$$d_t[\phi] + \nabla^{\Gamma} \cdot [\vec{j}] = 0,$$

where $d_t = d/dt$ is the total time derivative and $\nabla^{\Gamma} \cdot$ is the surface divergence operator [64]. Since we employ a Lagrangian approach, $d/dt[\phi]$ can be evaluated directly. However, in Eulerian approaches it would be necessary to evaluate $\frac{d}{dt}[\phi] = \nabla^{\Gamma}[\phi] \cdot \partial_t[\vec{X}] + \partial_t[\phi]$, i.e. the transport of ϕ by the deforming surface would have to be considered.

The flux \vec{j} is determined by the lateral gradient of the chemical potential $\mu(u_1, u_2)$, i.e. $\vec{j} = \nabla^{\Gamma}[\mu]$. μ is proportional to the variation of the free energy F with respect to

ϕ , and thus $\mu = L_\phi \frac{\delta}{\delta \phi} [F]$; the mobility L_ϕ is assumed to be constant. We obtain the following dynamical equation for ϕ :

$$d_t[\phi] = L_\phi \Delta^\Gamma \left[\frac{\delta}{\delta \phi} [F] \right],$$

where Δ^Γ is the Laplace-Beltrami operator [64].

Given a certain deformation, the membrane system itself evolves in the direction of the steepest descent of the free bilayer energy. Assuming overdamped motion (a typical assumption for molecular systems) as well as lateral incompressibility [70], the dynamics of the deformation \vec{X} in $U \times [0, T)$ are given by the following gradient flow

$$d_t[\vec{X}] = -L_X \frac{\delta}{\delta \vec{X}} \left[F + \int_\Gamma \gamma ds \right] \quad (2.6)$$

with a local area constraint,

$$d_t[\sqrt{g}] = 0, \quad (2.7)$$

where L_X is the kinetic coefficient, $\frac{\delta}{\delta \vec{X}} [F]$ denotes the variation of F with respect to \vec{X} , including normal as well as tangential components, γ is the local Lagrange multiplier modeling local membrane incompressibility, and \sqrt{g} is the surface measure (c.f. Appendix A). For details concerning equation (2.7) and the realization of local incompressibility, we refer to [93, 237].

Although variations of parts of F have been previously derived in [163], a complete treatment of F using a sharp interface approach for the membrane and an arbitrary diffuse interface for ϕ can not be found in the literature. We present some detailed calculations of the Fréchet derivatives of F in the following section; proofs developed in [163] have been significantly shortened and they are presented in Appendix D.

2.4.3 Statement of the Main Result

In the following, we assume vanishing boundary integrals, i.e. closed surfaces or periodic boundary conditions. Furthermore, we assume that the elastic moduli and the function $f(\phi)$ are regular functions, i.e. $\kappa, \kappa_G, H_0, f \in C^\infty([-1, 1])$.

Theorem II.1. *Deformation of the lateral phase separating local incompressible membrane is given by*

$$\begin{aligned} d_t \vec{X} &= -L_X \frac{\delta}{\delta \vec{X}} \left[F + \int_{\Gamma} \gamma ds \right] \\ &= -L_X \left[A^\perp \vec{n} + \sum_k A^k \partial_k \vec{X} \right] \end{aligned} \quad (2.8)$$

with the constraint

$$d_t [\sqrt{g}] = 0, \quad (2.9)$$

where

$$\begin{aligned} A^\perp &= -\Delta^\Gamma [\kappa(\phi)(H - H_0(\phi))] \\ &\quad -\kappa(\phi)(H - H_0(\phi))(H^2 - 2K) + \frac{\kappa(\phi)}{2}(H - H_0(\phi))^2 H \\ &\quad -\widehat{\Delta}^\Gamma [\kappa_G(\phi)] \\ &\quad -\xi^2 \sum_{i,j} b^{ij} \partial_i [\phi] \partial_j [\phi] + H \left(\frac{\xi^2}{2} (\nabla^\Gamma [\phi])^2 + f(\phi) \right) \\ &\quad + H\gamma \\ &\quad + \frac{2\bar{\kappa}\pi}{AD} (\Delta A - \Delta A_0) K \end{aligned}$$

and

$$\begin{aligned} A^k &= -\frac{1}{2} \partial^k [\kappa(\phi)] (H - H_0(\phi))^2 \\ &\quad + \kappa(\phi)(H - H_0(\phi)) \partial^k [H_0(\phi)] \\ &\quad - \partial^k [\kappa_G(\phi)] K \\ &\quad + \xi^2 \sum_l \nabla_l [\partial^k \phi \partial^l \phi] - \partial^k \left[\frac{\xi^2}{2} (\nabla^\Gamma \phi)^2 + f(\phi) \right] \\ &\quad - \partial^k [\gamma]. \end{aligned}$$

Furthermore, lateral dynamics of the order parameter ϕ are given by

$$\begin{aligned} d_t [\phi] &= L_\phi \Delta^\Gamma \left[\frac{\delta}{\delta \phi} [F] \right] \\ &= L_\phi \Delta^\Gamma \left[\frac{1}{2} \kappa'(\phi) (H - H_0(\phi))^2 - \kappa(\phi) (H - H_0(\phi)) H_0'(\phi) \right. \\ &\quad \left. + \kappa'_G(\phi) K - \xi^2 \Delta^\Gamma \phi + f'(\phi) \right]. \end{aligned} \quad (2.10)$$

The proof of the theorem is given in the following section and in Appendix D (Fréchet derivatives of $F_1 - F_3$ appear already in [163]. Corresponding shortened calculations are given in Appendix D). For notational convenience, we consider here and in the following the case $\sigma = 1$.

2.4.4 Proof of the Main Result

To prove the main result, we rely in the following on already derived variational expressions (c.f. Appendix C) as well as in some parts on simple reformulations using the parametric representation.

Lemma II.2.

$$\frac{\delta^\perp[F_4]}{\delta \vec{X}} = \frac{2\bar{\kappa}\pi}{AD} (\Delta A - \Delta A_0) K.$$

Proof: Using the chain rule, (C.1)-(C.2) (c.f. Appendix C) as well as $\Delta A = D \int_\Gamma H \sqrt{g} d^2u$, we obtain

$$\begin{aligned} \delta^\perp[F_4] &= \frac{\bar{\kappa}\pi}{AD^2} (\Delta A - \Delta A_0) D \int_\Gamma \delta^\perp[H \sqrt{g} d^2u] \\ &= \frac{\bar{\kappa}\pi}{AD} (\Delta A - \Delta A_0) \int_\Gamma (\delta^\perp[H] \sqrt{g} d^2u + H \delta^\perp[\sqrt{g} d^2u]) \\ &= \frac{\bar{\kappa}\pi}{AD} (\Delta A - \Delta A_0) \int_\Gamma ((-\Delta^\Gamma[\psi] - \psi(H^2 - 2K)) \sqrt{g} d^2u + H\psi H \sqrt{g} d^2u). \end{aligned}$$

From Green's identities it follows that $\int_\Gamma \Delta^\Gamma[\psi] \sqrt{g} d^2u = 0$ [258], leading to the assertion of the Lemma. \square

Lemma II.3.

$$\frac{\delta^t[F_4]}{\delta \vec{X}} = 0.$$

Proof: Using Proposition (D.5)-(D.6) (c.f. Appendix D), the chain rule as well as $\Delta A = D \int_\Gamma H \sqrt{g} d^2u$, we obtain

$$\begin{aligned} \delta^t[F_4] &= \frac{\bar{\kappa}\pi}{AD^2} (\Delta A - \Delta A_0) D \int_\Gamma \delta^t[H \sqrt{g} d^2u] \\ &= \frac{\bar{\kappa}\pi}{AD} (\Delta A - \Delta A_0) \int_\Gamma (\delta^t[H] \sqrt{g} d^2u + H \delta^t[\sqrt{g} d^2u]) \\ &= \frac{\bar{\kappa}\pi}{AD} (\Delta A - \Delta A_0) \int_\Gamma \left(\left(\sum_{i,j,k} g^{ij} \nabla_k [b_{ij}] \psi^k \right) - \left(\sum_{k,u} \partial^u [H] g_{uk} \psi^k \right) \right) \sqrt{g} d^2u. \end{aligned}$$

Using (C.7) and (C.8) (c.f. Appendix C) as well as commutation of the covariant derivatives and the first metric tensor, we conclude that

$$\begin{aligned} \sum_{i,j} g^{ij} \nabla_k [b_{ij}] &= \sum_{i,j} g^{ij} \nabla_j [b_{ik}] = \sum_j \nabla_j \left[\sum_i g^{ij} b_{ik} \right] \\ &= \sum_j \nabla_j [b^j_k] = \partial_k [H] = \sum_u g_{uk} \partial^u [H]. \end{aligned}$$

Hence, the claim follows. \square

2.5 Nondimensionalization

In the following section the free energy (c.f. Section 2.4.1) and corresponding dynamic equations (c.f. Section 2.4.2) of our basic model are nondimensionalized. This reformulation allows us, on the one hand, to identify essential parameters and characteristic properties of our system. On the other hand, it enables us to study the relative dependence of different parameters on spatial and temporal scales.

To nondimensionalize the model, we replace each variable v with a dimensionless quantity v_c which is scaled with a characteristic unit of measure ϵ_v .

2.5.1 Free Energy

We set

$$\vec{X} = \epsilon_x \vec{X}_c,$$

with $[\vec{X}] = [\epsilon_x] = m$, which implies $ds = \epsilon_x^2 ds_c$, $\nabla^\Gamma = \frac{1}{\epsilon_x} \nabla_c^\Gamma$, $\xi = \epsilon_x \xi_c$, $D = \epsilon_x D_c$, $A = \epsilon_x^2 A_c$, $\Delta A = \epsilon_x^2 \Delta A_c$, $\Delta A_0 = \epsilon_x^2 \Delta A_{0c}$, $H = \frac{1}{\epsilon_x} H_c$, $H_0 = \frac{1}{\epsilon_x} H_{0c}$ and $K = \frac{1}{\epsilon_x^2} K_c$.

Furthermore, we choose

$$\begin{aligned} \phi &= \phi_c, \quad f = f_c, \quad \kappa(\phi) = \epsilon_\kappa \kappa_c(\phi), \quad \kappa_G(\phi) = \epsilon_\kappa \kappa_{Gc}(\phi), \quad \bar{\kappa} = \epsilon_\kappa \bar{\kappa}_c \\ \text{and } \sigma &= \frac{\epsilon_\kappa}{\epsilon_x^2} \sigma_c \end{aligned}$$

with $[\epsilon_\kappa] = k_B T$, $[\kappa(\phi)] = [\kappa_G(\phi)] = [\bar{\kappa}] = k_B T$, $[\sigma] = \frac{k_B T}{m^2}$ and $[\xi] = m$. Since $[\phi] = [f] = 1$, ϕ and f are dimensionless by construction and thus do not need to be nondimensionalized. The nondimensionalization yields

$$\begin{aligned} & \frac{1}{2} \int_{\Gamma} \kappa(\phi) (H - H_0(\phi))^2 ds + \int_{\Gamma} \kappa_G(\phi) K ds + \sigma \int_{\Gamma} \left(\frac{\xi^2}{2} (\nabla^\Gamma \phi)^2 + f(\phi) \right) ds \\ & \quad + \frac{\bar{\kappa}}{2} \frac{\pi}{AD^2} (\Delta A - \Delta A_0)^2 \\ &= \epsilon_\kappa \int_{\Gamma} \left(\frac{1}{2} \kappa_c(\phi) (H_c - H_{0c}(\phi))^2 + \kappa_{Gc}(\phi) K_c + \sigma_c \left(\frac{\xi_c^2}{2} (\nabla_c^\Gamma \phi)^2 + f(\phi) \right) \right) ds_c \\ & \quad + \frac{\bar{\kappa}_c}{2} \frac{\pi}{A_c D_c^2} (\Delta A_c - \Delta A_{0c})^2. \end{aligned}$$

A consistency check shows that $[F]$ has units of energy as expected, i.e. $F = \epsilon_\kappa F_c$ with $[F_c] = 1$. Calculating the variation of F we obtain for the strong formulation $[\frac{\delta F}{\delta \phi}] = \frac{[\epsilon_\kappa]}{[\epsilon_x]^2} = \frac{k_B T}{m^2}$ as well as $[\frac{\delta F}{\delta \vec{X}}] = \frac{[\epsilon_\kappa]}{[\epsilon_x]^3} = \frac{k_B T}{m^3}$.

2.5.2 Dynamics

Considering the dynamics, we set

$$t = \epsilon_t t_c, \quad L_\phi = \epsilon_L L_{\phi c}, \quad L_X = \epsilon_L L_{Xc}, \quad \gamma = \frac{\epsilon_\kappa}{\epsilon_x^2} \gamma_c$$

with $\epsilon_L = \frac{\epsilon_x^4}{\epsilon_\kappa \epsilon_t}$ and thus $[t] = s$, $[L_\phi] = [L_X] = \frac{m^4}{k_B T s}$ as well as $[\gamma] = \frac{k_B T}{m^2}$. Furthermore, it holds $\partial_t = \frac{1}{\epsilon_t} \partial_{t_c}$, hence $[\partial_t] = \frac{1}{s}$. It follows

$$\partial_{t_c} \phi_c = -L_{\phi c} \Delta_c^\Gamma \left(\frac{\delta F_c}{\delta \phi} \right)$$

and

$$\partial_{t_c} \vec{X}_c = -L_{Xc} \left(\frac{\delta(F_c + \int \gamma_c ds_c)}{\delta \vec{X}} \right). \quad (2.11)$$

CHAPTER III

Finite Element Approximation

3.1 Mixed Formulation

Using the finite element library Gascoigne [19], we discretize the fourth order PDE model in a mixed formulation [33] following the ideas of [14, 15]. Hence, variational formulations use H^1 spaces, and we use quadrangulated surfaces and H^1 conforming bilinear surface finite elements for corresponding approximations. The mean curvature H and the Gaussian curvature K are treated in the following as additional unknown functions. For this purpose, we use the geometric identities [211]

$$\Delta^\Gamma[\vec{X}] = H\vec{n}, \quad (3.1)$$

and

$$|\nabla^\Gamma \vec{n}|^2 = H^2 - 2K, \quad (3.2)$$

where \vec{n} denotes the unit normal vector. Furthermore, following the approach of [80] we introduce the chemical potential as an additional unknown function Y , i.e. we introduce the additional equation

$$Y = \frac{1}{2}\kappa'(\phi)(H - H_0(\phi))^2 - \kappa(\phi)(H - H_0(\phi))H_0'(\phi) + \kappa_G'(\phi)K - \sigma(\xi^2\Delta^\Gamma\phi - f'(\phi)). \quad (3.3)$$

Finally, the additional unknown function G is introduced via the equation

$$G = \frac{\xi^2}{2}(\nabla^\Gamma[\phi])^2 + f(\phi). \quad (3.4)$$

3.2 Analytical Reformulations

The derivation of a weak formulation of system (2.8)-(2.10) (c.f. Section 2.4.3), as it will be introduced below, relies mainly on the chain rule and on partial integration as well as on the following calculations based on reformulation of the parametric representation.

Using the definition of the covariant derivative as well as integration by parts (assuming vanishing boundary conditions) it follows that

$$\begin{aligned}
& \int_{\Gamma} \nabla_u [\partial^k [\phi] \partial^u [\phi]] \psi \sqrt{g} d^2u \\
&= \int_{\Gamma} (\partial_u [\partial^k [\phi] \partial^u [\phi]] + \sum_l \Gamma_{ul}^k \partial^l [\phi] \partial^u [\phi] + \sum_l \Gamma_{ul}^u \partial^k [\phi] \partial^l [\phi]) \psi \sqrt{g} d^2u \\
&= - \int_{\Gamma} \partial^k [\phi] \partial^u [\phi] \partial_u [\psi \sqrt{g}] d^2u + \int_{\Gamma} (\sum_l \Gamma_{ul}^k \partial^l [\phi] \partial^u [\phi] + \sum_l \Gamma_{ul}^u \partial^k [\phi] \partial^l [\phi]) \psi \sqrt{g} d^2u \\
&= - \int_{\Gamma} \partial^k [\phi] \partial^u [\phi] \partial_u [\psi] ds - \int_{\Gamma} \partial^k [\phi] \partial^u [\phi] \partial_u [\sqrt{g}] \psi d^2u \\
&+ \int_{\Gamma} (\sum_l \Gamma_{ul}^k \partial^l [\phi] \partial^u [\phi] + \sum_l \Gamma_{ul}^u \partial^k [\phi] \partial^l [\phi]) \psi ds.
\end{aligned}$$

Applying the chain rule to the determinant and using the definition of the Christoffel symbols leads to $\partial_u [\sqrt{g}] = \sum_{r,s} \frac{1}{2\sqrt{g}} g g^{rs} \partial_u [g_{rs}] = \sum_l \sqrt{g} \Gamma_{ul}^l$. This yields

$$\begin{aligned}
\sum_u \int_{\Gamma} \nabla_u [\partial^k [\phi] \partial^u [\phi]] \psi \sqrt{g} d^2u &= \sum_u \left(- \int_{\Gamma} \partial^k [\phi] \partial^u [\phi] \partial_u [\psi] ds - \sum_l \int_{\Gamma} \partial^k [\phi] \partial^u [\phi] \Gamma_{ul}^l \psi ds \right. \\
&\quad \left. + \sum_l \int_{\Gamma} \Gamma_{ul}^k \partial^l [\phi] \partial^u [\phi] \psi ds + \sum_l \int_{\Gamma} \Gamma_{ul}^u \partial^k [\phi] \partial^l [\phi] \psi ds \right) \\
&= - \sum_u \int_{\Gamma} \partial^k [\phi] \partial^u [\phi] \partial_u [\psi] ds + \sum_{l,u} \int_{\Gamma} \Gamma_{ul}^k \partial^l [\phi] \partial^u [\phi] \psi ds.
\end{aligned}$$

Furthermore, for $h \in \{H_0, \kappa, \kappa_G\}$ it holds

$$\nabla^\Gamma [h(\phi)] = \sum_{i,j} g^{ij} \partial_j [h(\phi)] \partial_i \vec{X} = \sum_{i,j} g^{ij} h'(\phi) \partial_j [\phi] \partial_i \vec{X} = h'(\phi) \nabla^\Gamma [\phi]$$

and

$$\partial^k [h(\phi)] = \sum_i g^{ik} \partial_i [h(\phi)] = \sum_i g^{ik} h'(\phi) \partial_i [\phi] = h'(\phi) \partial^k [\phi],$$

from the chain rule.

Thus, using Green's formula (assuming vanishing boundary conditions, i.e closed surfaces or periodic boundary conditions) it follows that

$$\begin{aligned}
\int_{\Gamma} \Delta^{\Gamma}[\kappa(\phi)(H - H_0(\phi))]\psi \, ds &= - \int_{\Gamma} \nabla^{\Gamma}[\kappa(\phi)(H - H_0(\phi))] \cdot \nabla^{\Gamma}[\psi] \, ds \\
&= - \int_{\Gamma} (H - H_0(\phi))\kappa'(\phi)\nabla^{\Gamma}[\phi] \cdot \nabla^{\Gamma}[\psi] \, ds \\
&\quad - \int_{\Gamma} \kappa(\phi)\nabla^{\Gamma}[H] \cdot \nabla^{\Gamma}[\psi] \, ds \\
&\quad + \int_{\Gamma} \kappa(\phi)H_0'(\phi)\nabla^{\Gamma}[\phi] \cdot \nabla^{\Gamma}[\psi] \, ds
\end{aligned}$$

and

$$\begin{aligned}
&\frac{1}{2}\partial^k[\kappa(\phi)](H - H_0(\phi))^2 + \kappa(\phi)(H - H_0(\phi))\partial^k[H_0(\phi)] \\
&= -\frac{1}{2}\kappa'(\phi)\partial^k[\phi](H - H_0(\phi))^2 + \kappa(\phi)(H - H_0(\phi))H_0'(\phi)\partial^k[\phi] \\
&= \partial^k[\phi](H - H_0(\phi))\left(-\frac{1}{2}\kappa'(\phi)(H - H_0(\phi)) + \kappa(\phi)H_0'(\phi)\right).
\end{aligned}$$

3.3 Finite Element Discretization

The adopted finite element discretization is mainly based on the work of Barrett *et al* [15]. Let us assume that $0 = t_0 < t_1 < \dots < t_{M-1} < t_M = T$ is a discretization of the time interval $[0, T]$ into time steps $\tau_m := t_{m+1} - t_m$, which are not necessarily equidistant. Further, let us assume that U^m is a conforming quadrangulation of $U = [0, 1] \times [0, 1]$ at time $t = t_m$. The approximation of the deformed surface Γ will be given by the parameterization $\vec{X}^m : U^m \rightarrow \Gamma^m$; thus it holds $\Gamma^m \ni \vec{q}_k^m = \vec{X}^m(\vec{u}_k^m)$. Since we work on U rather than on Γ we pursue a purely Lagrangian approach. Hence, $\Gamma^m = \cup_{j=1}^J \bar{\sigma}_j^m$ and $\{\sigma_j^m\}_{j=1}^J$ is a family of mutually disjoint open quadrangles with vertices $\{\vec{q}_k^m\}_{k=1}^K$ and areas $|\sigma_j^m|$. By $\vec{q}_{k1,j}^m$ and $\vec{q}_{k2,j}^m$ we denote the nearest neighbor vertices of \vec{q}_k^m in $\bar{\sigma}_j^m$, i.e. $\vec{q}_k^m, \vec{q}_{k1,j}^m, \vec{q}_{k2,j}^m \in \bar{\sigma}_j^m$. Furthermore, let us define $h_{ki,j}^m := |\vec{u}_k^m - \vec{u}_{ki,j}^m|$.

Let \vec{N}_j^m be the unit normal on each quadrangle σ_j^m . Based on this, we further introduce the discrete vertex normals by (following [15])

$$\vec{\nu}^m(\vec{q}_k^m) = \frac{\vec{n}_k^m}{|\vec{n}_k^m|} \quad \text{where} \quad \vec{n}_k^m := \frac{1}{|\alpha_k^m|} \sum_{\sigma_j^m \cap q_k^m \neq \emptyset} |\sigma_j^m| \vec{N}_j^m, \quad (3.5)$$

where $|\alpha_k^m| := \sum_{\sigma_j^m \cap q_k^m \neq \emptyset} |\sigma_j^m|$ represents the total measure of the quadrangles counterminous to q_k^m . Furthermore, we define $\vec{t}_i^m := \partial_i[\vec{X}(\vec{u}_k, t_m)]/|\partial_i[\vec{X}(\vec{u}_k, t_m)]|$ such that

$\{\nu^m, \vec{t}_1^m, \vec{t}_2^m\}$ form an orthonormal basis of \mathbb{R}^3 . In addition, we introduce the following finite difference quotient

$$\vec{\delta}_{i,j}^k := \frac{\vec{X}^m(u_{ki,j}^m) - \vec{X}^m(u_k^m)}{h_{ki,j}^m},$$

where the index i and the sign of $\vec{\delta}_{i,j}^k$ are chosen such that $\vec{\delta}_{i,j}^k$ is the differential quotient corresponding to $\partial_i[\vec{X}(\vec{u}_k, t_m)]$. Using this finite difference quotient, the discrete vertex components of the first fundamental tensor g_{xy} can be computed as follows

$$g_{(x,y)k}^m := \frac{1}{|\alpha_k^m|} \sum_{\sigma_j^m \cap q_k^m \neq \emptyset} |\sigma_j^m| (\vec{\delta}_{x,j}^k \cdot \vec{\delta}_{y,j}^k). \quad (3.6)$$

In contrast to the approach in reference [15], which does not consider the Cahn-Hilliard part, we explicitly require a discrete approximation of the first fundamental tensor to approximate the resulting covariant derivatives. Discrete vertex Christoffel symbols are defined by

$$\Gamma_{jz}^{i(m)}(\vec{q}_k^m) := \frac{1}{2} \sum_l g_k^{(i,l)m} \left(\partial_z [g_{(j,l)k}^m] + \partial_j [g_{(l,z)k}^m] - \partial_l [g_{(j,z)k}^m] \right), \quad (3.7)$$

where $g_k^{(i,l)m}$ are the components of the inverse of the matrix \mathbf{g}^m , defined as

$$\mathbf{g}^m = (\partial_i [\vec{X}^m(\vec{q}_k^m)] \cdot \partial_l [\vec{X}^m(\vec{q}_k^m)])_{i,l}.$$

Numerical studies indicate that both approximations (3.5) and (3.6) are of order $\mathcal{O}(h^2)$, where $h := \max_{j=1 \rightarrow J} \text{diam}(\sigma_j^m)$.

In the following, we define the finite element space of globally continuous, periodic, piecewise bilinear elements by $V(\Gamma^m) := \{\vec{\psi} \in C(\Gamma^m, \mathbb{R}) : \vec{\psi}|_{\sigma_j^m} \text{ is bilinear for } j = 1, \dots, J\} \subset H^1(\Gamma^m, \mathbb{R})$. Similarly, we introduce the finite element space $\underline{V}(\Gamma^m) \subset H^1(\Gamma^m, \mathbb{R}^d)$. For scalar, vector and matrix valued functions $f, g \in L^2$ we introduce the L^2 inner product $\langle \cdot, \cdot \rangle_m$ over Γ^m as $\langle f, g \rangle_m := \int_{\Gamma^m} (f \cdot g) ds$, where $f \cdot g$ denotes the usual inner products for scalars, vectors and matrices.

3.3.1 Discretized Dynamical Equations

In the following we use the "natural functions" \vec{X}, ϕ and γ (c.f. Section 2.4) and the auxiliary functions H, K, G, Y as well as the discrete approximations (3.5)-(3.7). Furthermore, we use the additional functions B_1 and B_2 which appear in the weak approximation of equation (3.1) and play a role in tangential grid control (c.f. Section 3.4 as well as [15]). Hence, the discrete approximation of the nonlinear PDE system (2.8)-(2.10) (c.f. Section 2.4.3) in its weak form containing only the first order derivatives has the following form.

Theorem III.1. *Discrete formulation of the basic model (presented in Section 2.4.3).*

Find

$\{\vec{X}^{m+1}, \phi^{m+1}, \gamma^{m+1}, H^{m+1}, K^{m+1}, B_1^{m+1}, B_2^{m+1}, G^{m+1}, Y^{m+1}\} \in V(\Gamma^m)^{11}$ such that

$$\begin{aligned}
& \left\langle \frac{\vec{X}^{m+1} - \vec{X}^m}{\tau_m}, \frac{\psi \vec{\nu}^m}{L_X} \right\rangle_m = \\
& - \langle \nabla^\Gamma[\phi^m], \nabla^\Gamma[\psi] \kappa'(\phi^m) (H^m - H_0(\phi^m)) \rangle_m \\
& - \langle \kappa(\phi^m) \nabla^\Gamma[H^{m+1}], \nabla^\Gamma[\psi] \rangle_m + \langle \kappa(\phi^m) H_0'(\phi^m) \nabla^\Gamma[\phi^m], \nabla^\Gamma[\psi] \rangle_m \\
& + \langle (H^m - H_0(\phi^m)) |\nabla^\Gamma[\nu^m]|_m^2, \psi \rangle_m \\
& - \left\langle \frac{\kappa(\phi^m)}{2} (H^m - H_0(\phi^m))^2 H^{m+1}, \psi \right\rangle_m \\
& - \langle \kappa'_G(\phi^m) \widehat{\nabla}^\Gamma[\phi^m], \nabla^\Gamma[\psi] \rangle_m + \sum_{i,j} \langle \sigma \xi^2 b^{ij} \partial_i[\phi^m] \partial_j[\phi^m], \psi \rangle_m \\
& - \langle H^m (G^{m+1} + \gamma^{m+1}), \psi \rangle_m \\
& - \left\langle \frac{2\bar{\kappa}\pi}{AD} (\Delta A^m - \Delta A_0) K^m, \psi \right\rangle_m \quad \forall \psi \in V(\Gamma^m),
\end{aligned} \tag{3.8}$$

and

$$\begin{aligned}
& \left\langle \frac{\vec{X}^{m+1} - \vec{X}^m}{\tau_m}, \frac{\psi \partial_k[\vec{X}^m]}{L_X} \right\rangle_m = \\
& - \langle \partial^k[\phi^m] (H^m - H_0(\phi^m)) \\
& \quad \left(- \frac{\kappa'(\phi^m)}{2} (H^m - H_0(\phi^m)) + \kappa(\phi^m) H_0'(\phi^m) \right), \psi \rangle_m \\
& + \langle \kappa'_G(\phi^m) K^{m+1} \partial^k[\phi^m], \psi \rangle_m \\
& + \sigma \sum_u \langle \xi^2 \partial^k[\phi^m] \partial^u[\phi^m], \partial_u[\psi] \rangle_m \\
& - \sigma \sum_{l,u} \langle \xi^2 \Gamma_{ul}^{k(m)} \partial^l[\phi^m] \partial^u[\phi^m], \psi \rangle_m \\
& + \langle \partial^k[G^{m+1} + \gamma^{m+1}], \psi \rangle_m \quad \forall \psi \in V(\Gamma^m),
\end{aligned} \tag{3.9}$$

hold for $k = 1, 2$. They are the discrete approximations of the evolution equation (2.8) in Section 2.4.3. Furthermore, we require that it holds:

$$\left\langle \frac{\nabla^\Gamma \cdot [\vec{X}^{m+1}] - \nabla^\Gamma \cdot [\vec{X}^m]}{\tau_m}, \psi \right\rangle_m = 0 \quad \forall \psi \in V(\Gamma^m), \tag{3.10}$$

which is the discrete approximation of the lateral incompressibility equation (2.9) in

Section 2.4.3 (since $\partial_t[\sqrt{g}] = \nabla^\Gamma \cdot [\vec{X}_t]$ [93]), as well as

$$\langle H^{m+1} \vec{\nu}^m + \sum_i B_i^{m+1} \vec{t}_i^m, \vec{\psi} \rangle_m + \langle \nabla^\Gamma[\vec{X}^{m+1}], \nabla^\Gamma[\vec{\psi}] \rangle_m = 0 \quad (3.11)$$

$$\forall \vec{\psi} \in \underline{V}(\Gamma^m),$$

which is the discrete approximation of equation (3.1) (c.f. [15]). Additionally we require that it holds:

$$\langle K^{m+1}, \psi \rangle_m = \frac{1}{2} \langle t \tau^2 (\nabla^\Gamma \vec{\nu}^m) - |\nabla^\Gamma \vec{\nu}^m|_m^2, \psi \rangle_m \quad \forall \psi \in V(\Gamma^m), \quad (3.12)$$

which is the discrete approximation of equation (3.2), as well as

$$\langle G^{m+1}, \psi \rangle_m = \sigma \langle \frac{\xi^2}{2} |\nabla^\Gamma[\phi^m]|_m^2 + f(\phi^m), \psi \rangle_m \quad \forall \psi \in V(\Gamma^m), \quad (3.13)$$

which is the discrete approximation of equation (3.4). Finally the discrete approximations of the equation determining the evolution of the components (2.10) in Section 2.4.3 and (3.3) are approximated by

$$\langle \frac{\phi^{m+1} - \phi^m}{\tau_m}, \psi \rangle_m = -L_\phi \langle \nabla^\Gamma[Y^{m+1}], \nabla^\Gamma[\psi] \rangle_m \quad \forall \psi \in V(\Gamma^m) \quad (3.14)$$

and

$$\begin{aligned} \langle Y^{m+1}, \psi \rangle_m &= \langle \frac{\kappa'(\phi^m)}{2} (H^m - H_0(\phi^m))^2, \psi \rangle_m \\ &\quad - \langle \kappa(\phi^m) (H^m - H_0(\phi^m)) H_0'(\phi^m), \psi \rangle_m \\ &\quad + \langle \kappa_G'(\phi^m) K^m + \sigma f'(\phi^m), \psi \rangle_m \\ &\quad + \sigma \xi^2 \langle \nabla^\Gamma[\phi^{m+1}], \nabla^\Gamma[\psi] \rangle_m \end{aligned} \quad \forall \psi \in V(\Gamma^m). \quad (3.15)$$

The surface measure ds and the surface gradients ∇^Γ and $\widehat{\nabla}^\Gamma$ depend on the detailed configuration of the membrane \vec{X} , which is an unknown. Thus, the gradients as well as many other operators are functionals with respect to the current deformation, leading to a highly nonlinear system. We choose a dependence on the previous time step, i.e. a dependence on \vec{X}^m and hence ds^m , ∇^{Γ^m} and $\widehat{\nabla}^{\Gamma^m}$. That is, we avoid true nonlinear formulations to facilitate numerical analysis. Hence, we linearize the system explicitly considering the nonlinear terms. In this way, the schemes are easy to solve as they are linear at each time step.

On the top of this non-conservative discretization (3.8)-(3.15) we add non-physical correction terms to ensure convergence to physically realistic solutions. Accumulation of numerical errors violating the incompressibility of the membrane and hence the

mass conservation of ϕ is globally corrected via an artificial global pressure. Furthermore, we correct the grid as outlined in the next section, without violating effective local mass conservation. We have verified in all simulations that the total area and the total amount of ϕ at the minimum configurations, $\int_{\Gamma^{min}} ds$ and $\int_{\Gamma^{min}} \phi ds$, differ from the initial values $\int_{\Gamma^0} ds$ and $\int_{\Gamma^0} \phi ds$ by less than 2.5%.

3.4 Tangential Grid Control

The numerical stability of the finite element scheme depends crucially on a consistent and conforming distribution of vertices on the deformed surface Γ^m . In order to control the tangential motion of Γ^m , we follow the ideas of Barrett [15] introducing a separate "mesh redistribution step" after each time step. However, it is not the mesh on the parameterizing surface U which is redistributed, but the transformed mesh on the surface Γ^m . Further alternative approaches preventing mesh distortion are given in [27, 79, 83]. Since we correct each transformed vertex in the tangential direction of the surface, the surface does not evolve up to discretization errors (in the normal direction) and thus the curvatures are not influenced by this correction step. However, during the correction step the spatial distribution of ϕ is influenced, since we have adopted a Lagrangian point of view and coordinate system. It holds: $\frac{d}{dt}\phi[\vec{X}(u_1, u_2, t), t] = \partial_t[\phi(u_1, u_2, t)] + \partial_t\vec{X} \cdot \nabla^\Gamma[\phi] = 0$, with $\partial_t\vec{X} \neq 0$, i.e. ϕ is advected with the membrane during the correction movement. In the normal direction no evolution takes place during the tangential grid control step. Therefore further corrections balancing this advection are necessary, i.e. ϕ has to be advected with the rate $-\partial_t\vec{X}$ in the opposite direction. Thus, the full grid control problem applied here reads:

Find $\{\vec{X}^{m+1}, H^{m+1}, B_1^{m+1}, B_2^{m+1}, \phi^{m+1}\} \in V(\Gamma^m)^7$ such that the following equations hold:

$$\left\langle \frac{\vec{X}^{m+1} - \vec{X}^m}{\tau_m}, \psi \vec{\nu}^m \right\rangle_m = 0 \quad \forall \psi \in V(\Gamma^m) \quad (3.16)$$

and, for $k = 1, 2$,

$$\left\langle \alpha_i^m \frac{\vec{X}^{m+1} - \vec{X}^m}{\tau_m}, \psi \vec{t}_k^m \right\rangle_m = \langle \alpha_i^m (\delta_i^m B_i^{m+1} + c_i^m), \psi \rangle_m \quad (3.17)$$

$$\forall \psi \in V(\Gamma^m),$$

as well as

$$\left\langle \frac{\phi^{m+1} - \phi^m}{\tau_m}, \psi \right\rangle_m \quad (3.18)$$

$$= \langle -(\delta_1^m B_1^{m+1} + c_1^i)(\nabla^\Gamma[\phi^{m+1}])_1 - (\delta_2^m B_2^{m+1} + c_2^m)(\nabla^\Gamma[\phi^{m+1}])_2, \psi \rangle_m$$

$$\forall \psi \in V(\Gamma^m)$$

and

$$\langle H^{m+1} \vec{\nu}^m + \sum_i \alpha_i^m B_i^{m+1} \vec{t}_i^m, \vec{\psi} \rangle_m + \langle \nabla^\Gamma [\vec{X}^{m+1}], \nabla^\Gamma [\vec{\psi}] \rangle_m = 0 \quad (3.19)$$

$$\forall \vec{\psi} \in \underline{V}(\Gamma^m).$$

Here, $0 \leq \alpha_i^m, \delta_i^m \in V(\Gamma^m)$ are the coefficients influencing the strength of the tangential correction and $c_i^m \in V(\Gamma^m)$ are the forcing terms, determining the direction of the tangential correction. A feasible choice for c_i^m is the tangential projection of the vector between each vertex \vec{q}_k^m and the average \vec{z}_k^m of its neighboring nodes, i.e. $c_i^m(\vec{q}_k^m) \equiv \frac{1}{\tau_m} (\vec{z}_k^m - \vec{q}_k^m) \cdot \partial_i [\vec{X}^m]$ [15]. Note that with the special choice $\alpha_i^m \equiv 0$ equations (3.16)-(3.19) collapse to a system without any normal and tangential movement.

3.5 General Simulation Behavior

Using the outlined macroscopic modeling approach, in this section we present numerous numerical experiments, including experimental convergence tests as well as qualitative and quantitative sensitivity analysis.

For all simulations shown in this section we use stochastically perturbed initial conditions as well as periodic boundary conditions. We have repeated each simulation at least twice using different stochastically perturbed initial conditions to ensure that this type of stochastic perturbation affects neither the dynamics nor the resulting shapes. Furthermore we assume constant rigidities κ , κ_G and $\bar{\kappa}$ but different spontaneous curvatures H_0^A and H_0^B for the lipid and molecule species A and B , reflecting the fact that the two components differ in shape. If not otherwise stated, $H_0(\phi) \equiv H_0^{in}$ is chosen as a linear interpolation between the two values $H_0(-1) = H_0^A$ and $H_0(+1) = H_0^B$. Furthermore, we use the double well potential $f(\phi) = \frac{9}{32}(1 - \phi^2)^2$ (c.f. Appendix B). Mass or energy flux across the boundaries is prevented due to lateral incompressibility $\sqrt{g} = const$ as well as periodic boundary conditions for all variables.

3.5.1 Simulation of a Membrane Patch

To qualitatively compare the model with the experimental data, we start from the simulations of membrane patches with slightly curved membranes and stochastically perturbed initial conditions with the average $\langle \phi(t=0) \rangle = \Phi^0 = -0.37$ (cf. FIG 3.1 A). We assume $\kappa \equiv 1.5$, $\kappa_G \equiv -1.0$, $\bar{\kappa} \equiv 0$, $H_0^A = -10.0$, $H_0^B = 5.0$, $\sigma = 450.0$, $\xi = 0.03$, $L_X = 0.0005$, and $L_\phi = 0.05$. Simulations show the transition from very heterogeneous initial conditions to a single domain of one component with a budded geometry being the minimal configuration (cf. FIG 3.1 A-D). This shape and pattern are comparable to those of stable structures observed in the experiments with real membranes (cf. FIG 3.1 F). Plotting the energy (2.5) over the simulation period reveals the expected decay in time (cf. FIG 3.1 E).

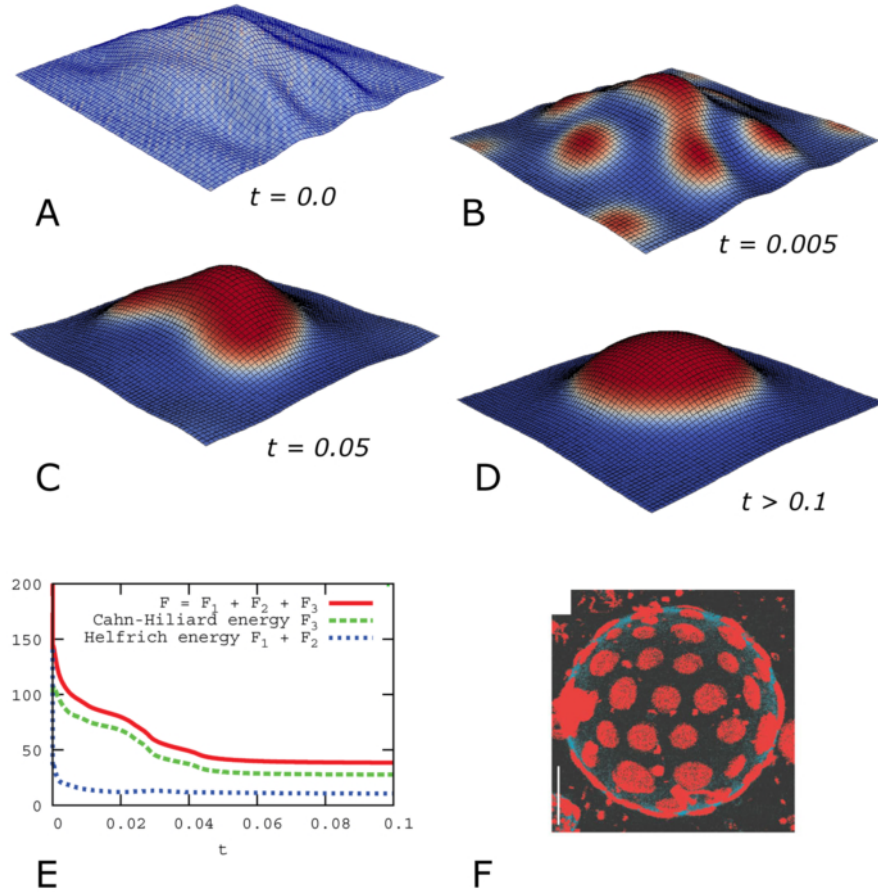


Figure 3.1: Simulation of membrane dynamics (A-D) reveals minimum structures (D) comparable to experiments (F) starting from disordered initial conditions (A). E: Corresponding energy decay. In (A-D) the two colors, red and blue, correspond to locally high concentrations of membrane species A and species B, respectively. F: Reprinted by permission from Macmillan Publishers Ltd: Nature, [18], © 2003.

3.5.2 Correcting Advection of ϕ

As already described in Section 3.4, due to non-physical lateral grid redistributions, ϕ has to be advected back. To check if this correcting advection works properly, we perform comparative simulations (c.f. FIG 3.2): we simulate Cahn-Hilliard dynamics starting with an initial gradient in ϕ on a planar membrane patch, comparing a uniformly distributed static mesh (FIG 3.2 A) with a highly nonuniform mesh being redistributed during the simulation (FIG 3.2 B-C). Simulation with and without correction advection shows the reliability of the scheme in case of mesh redistribution: in the case FIG 3.2 B simulation patterns are similar to those of the uniform mesh (FIG 3.2 A), whereas without correcting advectuations simulations show strikingly different patterns (FIG 3.2 C).

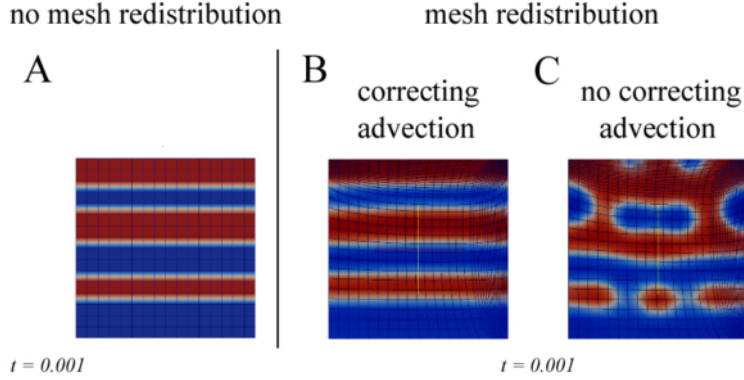


Figure 3.2: Numerically proving lateral correcting advection of ϕ simulating Cahn-Hilliard dynamics on a planar membrane patch. A: Uniform static mesh. B-C: Nonuniform mesh, redistributing during simulation time. Active correcting advection terms (B) lead to very similar patterns as in the case of the uniform mesh (A); inactive correcting advection leads to nonphysical defective patterns (C).

3.5.3 Convergence Verification

In this section, we present experimental convergence tests. First, we check the experimental order of convergence (EOC) for the discrete approximations for the normal and the first metric tensor (c.f. Section 3.3) on a highly curved non-symmetric surface. The EOC is defined by $EOC := \frac{\log E(h_1) - \log E(h_2)}{\log h_1 - \log h_2}$, where E is an error functional and h_1 and h_2 represent two sequent mesh sizes. Since we have used second order difference quotients for these approximations, the observed EOC is expected to be of order 2 while refining the mesh (c.f. Table 3.1). As reference values we use the normal and first metric tensor of the finite element approximation with $K = 4^8$ elements.

| K | $\ \vec{n} - \vec{n}'\ _{L^2} / \ \vec{n}\ _{L^2}$ | EOC | $\ \mathbf{g} - \mathbf{g}'\ _{L^2} / \ \mathbf{g}\ _{L^2}$ | EOC |
|-------|--|--------|---|--------|
| 4^2 | 0.003850 | — | 0.005675 | — |
| 4^3 | 0.001032 | 0.9497 | 0.001636 | 1.7944 |
| 4^4 | 0.000270 | 1.9344 | 0.000441 | 1.8913 |
| 4^5 | 0.000069 | 1.9683 | 0.000119 | 1.8898 |
| 4^6 | 0.000017 | 2.0211 | 0.000031 | 1.9406 |
| 4^7 | 0.000004 | 2.0875 | 0.000007 | 2.1468 |

Table 3.1: Relative errors and experimental orders of convergence (EOC) of the discrete approximations \vec{n}' and \mathbf{g}' of the normal vector and the first metric tensor, respectively. K is the number of elements, \vec{n} and \mathbf{g} are the finite element approximations using $K = 4^8$ elements.

Secondly, we investigate the EOC of the free energy F (c.f. Section 2.4.1) of a budded minimum configuration of the coupled system. Using the minimum free energy F_{min}^{ref} of the finite element approximation with $K = 4^7$ elements as the reference value, we observe that the EOC is of order 2 while refining the mesh (c.f. Table 3.2), as expected. For the corresponding simulations we use $\kappa_A = 1.5$, $\kappa_B = 2.0$ $\kappa_G \equiv -1.0$,

$H_0^A = -5.0$, $H_0^B = 0.0$, $L_X = 0.0005$, and $L_\phi = 0.05$. Furthermore, we compare $\xi = 0.1, \sigma = 50$ with $\xi = 0.05, \sigma = 100$. Hence, in both cases it holds for the sharp line tension $\sigma_{si} = \sigma\xi = 5$ (c.f. Appendix B).

| | $\xi = 0.1, \sigma = 50$ | | $\xi = 0.05, \sigma = 100$ | |
|-------|-----------------------------|--------|-----------------------------|--------|
| K | $ F_{min} - F_{min}^{ref} $ | EOC | $ F_{min} - F_{min}^{ref} $ | EOC |
| 4^2 | 8.6349 | — | 3.4178 | — |
| 4^3 | 0.6752 | 3.6768 | 0.2669 | 3.6787 |
| 4^4 | 0.1809 | 1.9001 | 0.0393 | 2.7637 |
| 4^5 | 0.0446 | 2.0201 | 0.0107 | 1.8769 |
| 4^6 | 0.0081 | 2.4610 | 0.0018 | 2.5715 |

Table 3.2: Experimental order of convergence of the free energy F_{min} in the minimum configuration of the coupled system while refining the mesh, using different values for ξ and σ . K is the number of elements and F_{min}^{ref} is the finite element approximation using $K = 4^7$ elements.

Thirdly, we investigate the EOC of the Willmore free energy $\int_\Gamma H^2 ds$, comparing minimum configurations of closed lateral homogeneous surfaces with known analytical solutions (simulations with closed surfaces have been used in Section 4.4, following the numerical approach of [105]). To do so, we have considered the relaxation to equilibrium of a strongly deformed lateral incompressible unit sphere $K_1(0)$. Comparing its Willmore energy with the energy of the well known analytical solution $K_1(0)$ [227] yields the expected EOC of approximately 2 (c.f. Table 3.3).

| K | $ \int_\Gamma H^2 ds - \int_{K_1(0)} H^2 ds $ | EOC |
|-------|---|--------|
| 4^2 | 31.3126 | — |
| 4^3 | 6.6054 | 2.2450 |
| 4^4 | 1.6003 | 2.0453 |
| 4^5 | 0.3958 | 2.0155 |
| 4^6 | 0.0991 | 1.9978 |

Table 3.3: Experimental order of convergence (EOC) of the Willmore free energy $\int_\Gamma H^2 ds$ in the equilibrium configuration, based on the deformed unit sphere. K is the number of elements; as reference we used the Willmore energy of the analytical well known solution which is the unit sphere itself.

3.5.4 Qualitative Sensitivity Analysis

To investigate the dependence of lateral dynamics, i.e. phase separation, and lateral minimum patterns on the choice of the unknown function $H_0(\phi)$, we perform simulations using $L_X = 0$ and fixing a non planar membrane setting $X^0(U) = 0.06 \sin(2\pi u_1) \sin(2\pi u_2)$ (cf. FIG 3.3 B). As initial conditions we choose $\langle \phi^0 \rangle = \Phi^0 = 0$. To facilitate the comparison of different simulations, we use exactly the same stochastically perturbed initial conditions. Corresponding results are presented in FIG 3.3. We compare the impact of the three different monotonous functions $H_0^{(1)}(\phi) = a_1 + b_1\phi$, $H_0^{(2)}(\phi) = a_2 + b_2 \tanh(-\phi)$ and $H_0^{(3)}(\phi) = a_3 + b_3x^5$ on the dynamics and minimum patterns of lateral sorting. Here, a_i and b_i are chosen so that $H_0^{(i)}(-1) = 0$ and $H_0^{(i)}(1) = -16$ hold for $i \in \{1, 2, 3\}$. Furthermore we set $\kappa \equiv 0.12$, $\kappa_G \equiv -0.12$, $\bar{\kappa} \equiv 0.0$, $\sigma = 9$, $\xi = 0.04$, and $L_\phi = 1.0$.

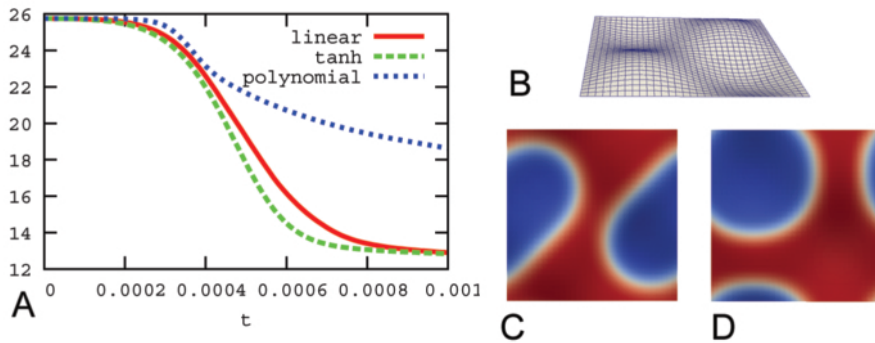


Figure 3.3: Lateral sorting on fixed non-planar geometry. A: The decay of the Cahn-Hilliard energy from unstable initial conditions using different functions for the spontaneous curvature $H_0(\phi)$. B: Corresponding membrane geometry. C-D: Various minimum patterns depending on the definition of $H_0(\phi)$.

We find that different choices of the function $H_0(\phi)$ strongly influence the dynamics of the model as well as the minimum patterns. Depending on the choice of $H_0^{(i)}$ the Cahn-Hilliard energy decays at different rates from the unstable initial conditions (c.f. FIG 3.3 A) resulting in the case of $H_0^{(3)}$ in a different pattern of minimum (c.f. FIG 3.3 D) compared to $H^{(1)}$ and $H^{(2)}$ (c.f. FIG 3.3 C). However, stable shapes of domains can differ from circles and stripes usually known from Cahn-Hilliard dynamics (c.f. FIG 3.3 C). This is caused by the fact that minimum patterns appear as the minimum of the overall energy, containing a curvature dependent part as well.

3.5.5 Quantitative Sensitivity Analysis

To investigate the sensitivity of the membrane minimum geometry with respect to the choice of the elastic coefficient, we perform simulations with various values of H_0^A , keeping $H_0^B = 0$. The corresponding results are shown in FIG 3.4, with $\sigma = 90$, $\xi = 0.03$, $L_X = 0.0005$, $L_\phi = 0.05$. Our simulations reveal that a stepwise increase of H_0^A from zero up to $H_0^A = -8$ results in minimum shapes stepwise increasing the

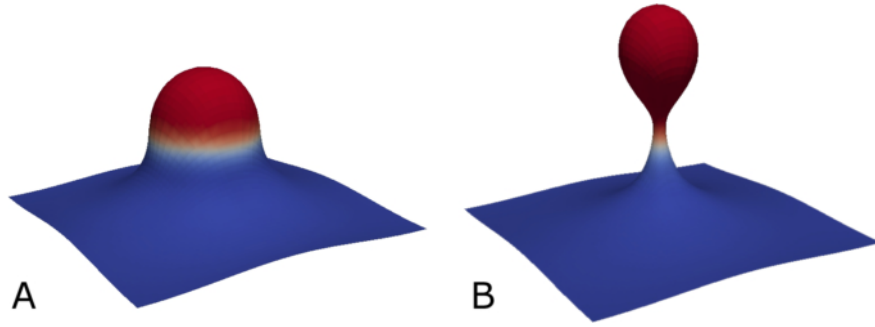


Figure 3.4: H_0 -induced budding transition: The minimum geometry is sensitive to the choice of elastic coefficient. A: $H_0^A = -8$, B: $H_0^B = -9$.

strength of budding, but still showing an incomplete bud (cf. FIG 3.4 A). Interestingly, choosing $H_0^A = -9$ results in a complete bud (c.f. FIG 3.4 B). This effect has been previously described as the budding transition and can be induced by different elastic parameters as well as domain size or volume constraints [60, 123, 124, 152]. This example shows prominently that small changes in the parameter value can lead to very different minimal geometries of the membrane.

CHAPTER IV

Applications

In the following chapter, we present various modifications of the basic model in order to investigate fundamental pattern formation mechanisms in both membranes and tissues. Our approach here is to perform extensive simulations in close comparison with recent experimental and theoretical results. Especially, we obtain the following new results.

Section 4.1:

- Numerical simulations show that curvature modulated sorting can occur if lipids or proteins differ in at least one of their macroscopic elastic moduli: gradients in each modulus, the bending rigidity, the Gaussian rigidity and the spontaneous curvature create characteristic (metastable) curvature dependent patterns.
- Simulations indicate that the larger moduli differences or curvature gradients are decomposition time decreases and the stability of curvature modulated patterns increases.
- Obtained phase diagrams allow to estimate if and how stable curvature modulated sorting will occur for a given geometry and elastic parameters.
- We present a new upscaling approach for models in membrane research, using DPD studies. Our results highlight that the use of upscaled models compared with common linear approximations can trap the system in different local minimum patterns.

Section 4.2:

- In numerical simulations we observe that all five elastic parameters - line tension, bending rigidity, Gaussian rigidity, spontaneous curvature as well as monolayer area difference - can be used to induce membrane budding. Particularly, we

show for the first time that the Gaussian rigidity plays a qualitative equivalent role in this process as the other parameters.

Section 4.3:

- We find that the stretching of two monolayers in the normal direction yields a sorting of membrane molecules according to their length. Furthermore, our simulations indicate that the length of molecules can be used to synchronize phases across the bilayer membrane.
- Simulations suggest that generating curvature in one monolayer (induced by different curvature creating mechanisms) sorts molecules of the other layer according to their shape and stiffness.

Section 4.4:

- We present for the first time a model for early pattern formation in biological tissues explicitly considering tissue curvature. Corresponding simulations reveal that a positive feedback loop of one morphogen with tissue curvature is sufficient to create various patterns from stochastic initial conditions without any prepattern.
- Comparing simulations to experimental data suggests that the proposed mechanism for tissue pattern formation is the key mechanism for symmetry break and early pattern formation in *Hydra* polyps.

We want to point out that the following Sections 4.1 - 4.4 are closely related to the publications [164, 165, 166, 167].

4.1 A Multiscale Approach Investigating Curvature Modulated Sorting in Membranes

4.1.1 Introduction

Biological membranes are composed of many different lipids, proteins and other molecules with different functions [4]. (For further details concerning the detailed assembly of biological membranes we refer to Section 2.1.1.) Lateral sorting of these components is essential for maintaining the diversity of different membrane systems inside the cell as well as the function of these systems [97]. For both, lipids [18] and proteins [26], lateral phase separation and clustering have been shown. It is widely accepted that membrane curvature modulated sorting is a basal mechanism controlling the spatial organization of lipids and proteins in the absence of specific chemical interactions. However, the exact underlying mechanisms remain mostly unknown [239].

It has been shown that spatial gradients in elastic moduli can exhibit a driving force for lateral curvature modulated sorting. Membrane proteins are drawn to regions with curvature adapted to the protein shape [202] and lipids with small bending rigidity are sorted to highly curved membrane regions [193], so that lateral reorganization reduces the membrane curvature energy. Although various theoretical and experimental studies have been performed to investigate lateral sorting due to gradients in spontaneous curvature [28, 55, 65, 125, 141, 148, 202, 207, 217] and bending rigidity [18, 65, 193, 210, 212], the impact of the elusive Gaussian rigidity on lateral sorting has not been investigated so far. However, experimental studies show that different membrane components can differ distinctly in their Gaussian rigidities [220].

In this section, we adopt and present a multiscale approach for lateral inhomogeneous membranes to parameterize a Cahn-Hilliard/Helfrich-type model (which is a simplification of the basic model, c.f. Section 2.4). Especially, parameterization of the continuous model from the molecular scale has been achieved via upscaling from dissipative particle dynamic (DPD) studies. On the basis of this multiscale modeling approach, simulations are performed comparing dynamics and minimum patterns of lateral sorting. We investigate theoretically the impact of an inhomogeneous Gaussian rigidity on lateral sorting and compare it with sorting due to gradients in the bending rigidity and spontaneous curvature. Following the experimental approach of [193, 210], we consider membranes attached to non-planar substrates. Thus, by considering a geometrically fixed membrane, the complexity is reduced facilitating the extraction of hypotheses to be checked by experimentalists. For large scale studies, we approximate solutions of the model using a finite element approach. The presented section is closely related to [165].

4.1.2 Mathematical Model

The model presented in this section is a simplified version of the model presented in Section 2.4. Following the ideas of [193, 210], we consider a curved membrane re-

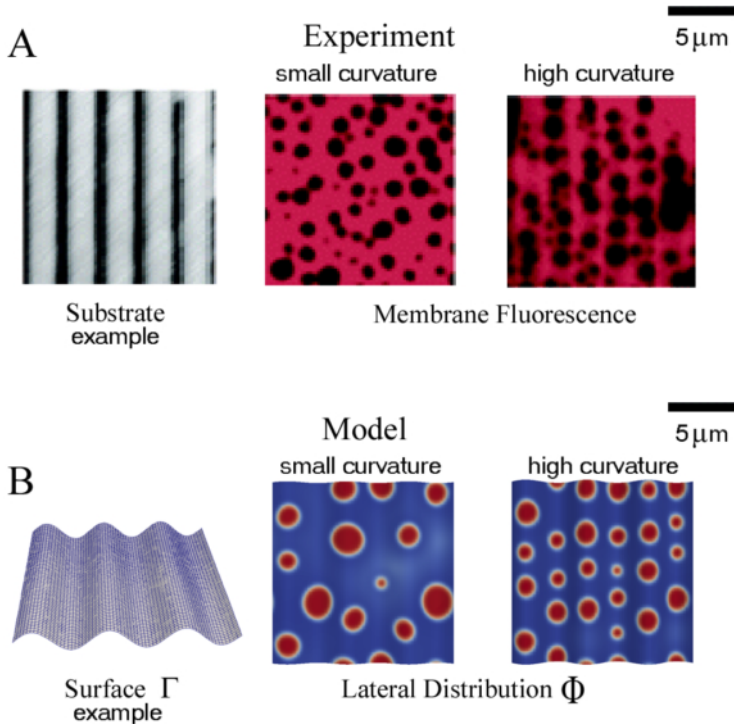


Figure 4.1: Experimental results versus mathematical model simulations. A: Experimental curvature dependent phase separation in corrugated membranes (reprinted with permission from [193], © 2006 American Chemical Society). B: Simulations of the mathematical model coupling curvature with lateral phase separation. High curvatures induce an ordering, whereas a phase separation on small curvatures appears randomly.

presented by a fixed smooth surface Γ in contrast to a free membrane (or a partially adhered vesicle) typically studied [2, 18, 107, 125, 196, 210, 239], where Γ itself is evolving in time.

Again, we consider a membrane composed of two different molecule species, e.g. two different lipids or lipids and proteins. The concentration of the two components ϕ^A and ϕ^B in Γ is described by the order parameter $\phi : \Gamma \rightarrow [-1, 1]$, where $\phi = \phi^A - \phi^B$. That means, if $\phi = 1$ the membrane is locally composed purely of species A and if $\phi = -1$ locally only species B is present.

It has been shown that sorting depends critically on membrane curvature and phase separation (in the absence of specific signals actively influencing lateral dynamics) [193, 210]. Therefore our model is based on the minimization of the free energy $F = F_1 + F_2 + F_3$ (c.f. Section 2.4.1) containing both the curvature depending energy $F_1 + F_2$ and the Cahn-Hilliard energy F_3 modeling lateral phase separation. The area difference elasticity term F_4 has been neglected, since it does not depend on the local distribution of ϕ , and hence does not influence lateral sorting.

Describing the fact that different components may differ in their mechanical properties (such as shape and stiffness), each macroscopic elastic modulus h ($h \in \{\kappa, \kappa_G, H_0\}$) is assumed to be a function of the concentration ϕ . Each function h is chosen so that $h(1) = h^A$ and $h(-1) = h^B$, where h^A and h^B are the elastic moduli of the pure components. Furthermore, ξ is a transition length, $\sigma_{si} = \sigma\xi$ the sharp line-tension (c.f. Appendix B), ∇^Γ the surface gradient and f a double well potential. The function $f : \mathbb{R} \rightarrow \mathbb{R}_+$ is of the form $f(\phi) = \frac{9}{32}(\phi^2 - 1)^2$ (c.f. Appendix B).

Instead of minimizing $F = F_1 + F_2 + F_3$ directly we adopt a dynamic point of view. Thus assuming local mass conservation (c.f. Section 2.4.2) as well as a fixed membrane, the basic model (c.f. Section 2.4.3) reduces to the following evolution equation for ϕ , given by

$$\begin{aligned} \partial_t[\phi] &= L_\phi \Delta^\Gamma \left[\frac{\delta}{\delta \phi} [F] \right] = L_\phi \Delta^\Gamma \left[\frac{1}{2} \kappa'(\phi) (H - H_0(\phi))^2 \right. \\ &\quad \left. - \kappa(\phi) (H - H_0(\phi)) H'_0(\phi) + \kappa'_G(\phi) K - \sigma (\xi^2 \Delta^\Gamma \phi - f'(\phi)) \right]. \end{aligned} \quad (4.1)$$

For corresponding existence and uniqueness proofs we refer to [165].

4.1.3 Finite Element Approximation and Parameter Setup

The bilayer is represented by a continuous two-dimensional (2D) surface Γ depicted by a parametric representation $\vec{X}(u_1, u_2) : U \rightarrow \Gamma \subset \mathbb{R}^3$, where $U = [0, 1] \times [0, 1]$, corresponding to a membrane patch of $12 \mu\text{m} \times 12 \mu\text{m}$.

By means of numerical studies, the equation (4.1) will be investigated in detail using numerical simulations based on the finite element library Gascoigne [19]. Since here only first order derivatives are available, we discretize this fourth order PDE in a mixed formulation, [33], with bilinear finite elements. In this section we briefly recapitulate the numerical approach adopted here, for further details we refer to Chapter III.

Let $0 = t_0 < t_1 < \dots < t_{M-1} < t_M = T$ be a discretization of the time interval $[0, T]$ into time steps $\tau_m := t_{m+1} - t_m$, which may be possibly variable. Let further Γ^q be a conforming quadrangulation approximating Γ , where $\Gamma^q = \cup_{j=1}^J \tilde{\nu}_j$ and $\{\tilde{\nu}_j\}_{j=1}^J$ is a family of mutually disjoint open quadrangles. The finite element space of globally continuous, piecewise bilinear elements is defined by $V(\Gamma^q) := \{\psi \in C(\Gamma^q, \mathbb{R}) : \psi|_{\tilde{\nu}_j} \text{ is bilinear } \forall j = 1, \dots, J\} \subset H^1(\Gamma^q, \mathbb{R})$. For scalar and vector valued functions $f, g \in L^2$ we introduce the L^2 inner product $\langle \cdot, \cdot \rangle$ over Γ^q as $\langle f, g \rangle := \int_{\Gamma^q} (f \cdot g) ds$, where $f \cdot g$ denotes the usual inner product for scalars and vectors. For details concerning approximations \mathcal{H} of the mean curvature H , \mathcal{K} of the Gaussian curvature K and of other geometrical quantities concerning Γ we refer to Section 3.3.

To reformulate the fourth order PDE (4.1) in a weak formulation using only first order derivatives, we follow the approach presented in Section 3.1. This leads to the

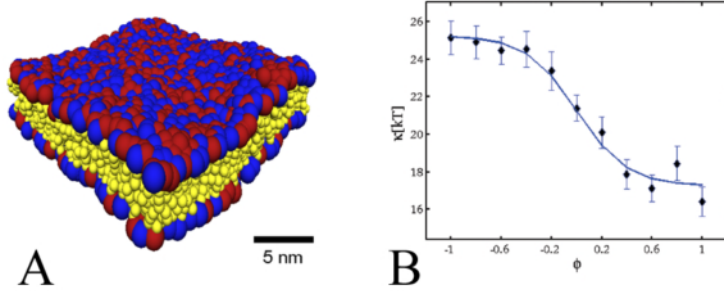


Figure 4.2: Dissipative particle dynamics (DPD) studies to investigate the nature of $\kappa(\phi)$. A: Typical DPD simulation snapshot with two lipids depicting different stiffnesses (headgroups are marked in blue and red, respectively). B: The bending rigidity κ of the simulated bilayers varies sigmoidal with the concentration ϕ of lipid species. (Both pictures reprinted with permission from Jens Kühnle, [131], © 2011)

following discrete approximation of equation (4.1):

For $m \geq 0$, find $\phi^{m+1}, Y^{m+1} \in V(\Gamma^q)$ such that

$$\left\langle \frac{\phi^{m+1} - \phi^m}{\tau_m}, \psi \right\rangle = -L_\phi \langle \nabla^\Gamma[Y^{m+1}], \nabla^\Gamma[\psi] \rangle \quad \forall \psi \in V(\Gamma^q) \quad (4.2)$$

and

$$\begin{aligned} \langle Y^{m+1}, \psi \rangle &= \left\langle \frac{\kappa'(\phi^m)}{2} (\mathcal{H} - H_0(\phi^m))^2, \psi \right\rangle + \sigma \xi^2 \langle \nabla^\Gamma[\phi^{m+1}], \nabla^\Gamma[\psi] \rangle \\ &\quad - \left\langle \kappa(\phi^m) (\mathcal{H} - H_0(\phi^m)) H_0'(\phi^m) + \kappa'_G(\phi^m) \mathcal{K} + \sigma f'(\phi^m), \psi \right\rangle \\ &\quad \forall \psi \in V(\Gamma^q) \end{aligned} \quad (4.3)$$

hold.

4.1.4 Upscaling and Numerical Results

So far, in the first approximation we have used a linear relationship $\kappa(\phi)$ in order to describe the macroscopic dependence of the bending rigidity κ on the lateral composition ϕ . Since the exact nature of the function $\kappa(\phi)$ is unknown, discrete Dissipative Particle Dynamics (DPD) studies can be used to determine this dependency in detail. We want to point out that all DPD studies in this regard have been performed and evaluated by Jens Kühnle (workgroup Matthias Weiss, Heidelberg University); for a detailed introduction concerning the DPD method, we refer to [131]. The DPD simulations use two different lipids showing different intrinsic lipid chain stiffnesses. Various simulations using different ratios of these two well mixed lipid species in DPD studies of small membrane patches (c.f. FIG 4.2 A) are performed. Using the methods of [86, 109, 218] it is possible to extract the corresponding macroscopic bending rigidity κ for each ratio. Finally, a heuristic fit yields that κ is a form of $a + b \tanh(-\phi)$, $a, b \in \mathbb{R}_{\geq 0}$ (c.f. FIG 4.2 B).

Using the calibrated functional relationship $\kappa(\phi)$ obtained from the DPD studies on a small scale level, we numerically study the lateral phase separation behavior in curved lipid bilayers on the large scale. Here, lateral phase separation is induced by gradients in the macroscopic elastic moduli κ , κ_G and H_0 . The molecular counterpart are differences in stiffness and shape of two kinds of membrane molecules.

In the first part, we compare the difference in dynamics and minimum patterns of our nonlinear multiscale model with common linear approximations. In the second part, we qualitatively and quantitatively compare and analyze the impact of gradients in each of the elastic moduli κ , κ_G and H_0 on lateral phase separation.

In the remainder of this section we use the following setup: the space discretization Γ^q consists of $J = 4096$ quadrangles with periodic boundary conditions for ϕ^m and Y^m . Since the Cahn-Hilliard functional has a small length scale, mesh sizes are always chosen significantly smaller than the transition length ξ . We numerically have proved that the numerical scheme converges as the mesh sizes are reduced. Furthermore, the result of simulations does not change with the further reduction of the mesh size (c.f. FIG 4.3 as well as Section 3.5.3). The time discretization is based on an adaptive time stepping scheme, starting with $\tau_0 = 0.3$ s. Since available experimental data do not contain the full parameter set necessary to parameterize our model, some values have been estimated. We always use a stochastically disturbed initial distribution $\phi^0 = \phi(t = 0)$ of total average $\langle \phi^0 \rangle = \Phi^0$ over the domain. Additionally, we have set: $\sigma = 119.47 k_B T \mu\text{m}^{-2}$, $\xi = 0.133 \mu\text{m}$, $L_\phi = 3.87 \cdot 10^{-4} \mu\text{m}^4 \text{s}^{-1} (k_B T)^{-1}$ and for the double well potential we have chosen $f(\phi) = \frac{9}{32}(\phi^2 - 1)^2$ (c.f. Appendix B). If not otherwise stated, we have considered $H_0^A = H_0^B = 0 \mu\text{m}^{-1}$; $\kappa^A = \kappa^B = 25.2 k_B T$ and $\kappa_G^A = \kappa_G^B = -25.2 k_B T$ ensuring the stability restriction $0 \geq \kappa_G \geq -2\kappa$ [216]. This set of parameters implies the following molecular membrane diffusion coefficient $D = L_\phi \sigma = 1.15 \cdot 10^{-10} \text{cm}^2 \text{s}^{-1}$ as well as the following "sharp" line tension given by $\sigma_{si} = \sigma \xi = 15.84 k_B T \mu\text{m}^{-1}$ (c.f. Appendix B). Odd numbers result from the conversion of abstract nondimensionalized model parameters into physical values.

4.1.4.1 Parameterized Model vs. Linear Approximations

Although the idea of coupling macroscopic elastic moduli with the lateral composition of lipid bilayers has been used in the past, the exact nature of these dependencies remains still unrevealed. Different approaches reaching from phenomenological coupling terms [5, 45, 120, 237, 260] to linear [145] and nonlinear [155, 248] functions $\kappa(\phi)$, $\kappa_G(\phi)$ and $H_0(\phi)$ have been used.

In this study a multiscale approach is proposed for the first time. As an example, the bending rigidity κ of the continuous model is parameterized via DPD experiments. We find that $\kappa(\phi)$ has the form of a tanh-function (see FIG 4.2 B) rather than a simple linear relationship. In order to get an impression of the importance of using more realistic upscaled data, we perform comparative studies: considering parallelly the

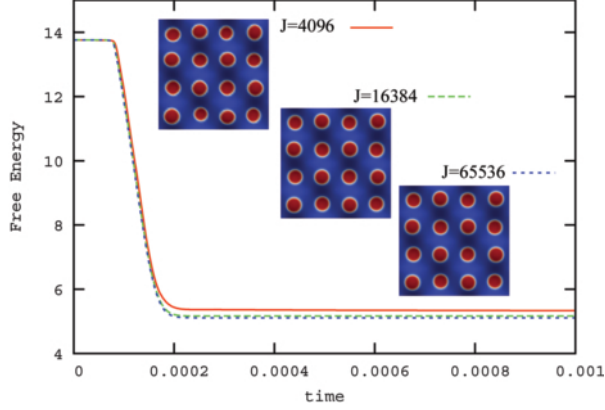


Figure 4.3: Using $J = 4096$, $J = 16384$ as well as $J = 65536$ meshpoints reveals a very similar temporal and spatial behavior.

nonlinear (upscaled) function

$$\kappa_{\tanh}(\phi) = a + b_1 \tanh(-\phi) \quad (4.4)$$

and the linear case commonly adopted

$$\kappa_{\text{lin}}(\phi) = a + b_2 \phi. \quad (4.5)$$

In FIG 4.4 the corresponding results are shown. The constants $a = \frac{\kappa^A + \kappa^B}{2}$, $b_1 = \frac{\kappa^A - \kappa^B}{2 \tanh(1)}$ and $b_2 = \frac{\kappa^A - \kappa^B}{2}$ are chosen so that in both cases $\kappa(1) = \kappa^A = 17.3k_B T$ and $\kappa(-1) = \kappa^B = 25.2k_B T$ are ensured. Furthermore, in both simulations we use the fixed geometry $\Gamma = \vec{X}(u_1, u_2) = 0.625 \sin(6\pi u_1) \mu\text{m}$ (cf. FIG 4.1 B) and the initial conditions $\langle \phi^0 \rangle = 0$, i.e. for a 1 : 1 mixture of both components. The prescribed geometry ensures $K \equiv 0$ so that κ_G does not play any role for this specific geometry.

We observe in early states of phase separation in the nonlinear case of κ a stronger dependence on the curvature (FIG 4.4 C) than in the linear case (FIG 4.4 A). This is likely to be a consequence of the steeper gradient of κ_{\tanh} compared to κ_{lin} close to the initial value $\langle \phi^0 \rangle = 0$. Since the breakage of already formed cross connections between the phases is energetically costly (it would elongate the overall size of the boundaries) early sorting effects can trap the system into different minimum patterns, corresponding to local minima of the free energy (2.5). This becomes obvious in comparing the minimum configurations FIG 4.4 B with FIG 4.4 D.

Choosing initial conditions $\langle \phi^0 \rangle$ away from zero, e.g. having many molecules of one component and less of the other, does not result in different local minimum configurations (results not shown). Since in this case circular phases of the component with the smaller amount are quickly arising and stable cross-connecting phases (c.f. green circular marks in FIG 4.4 A) are missing.

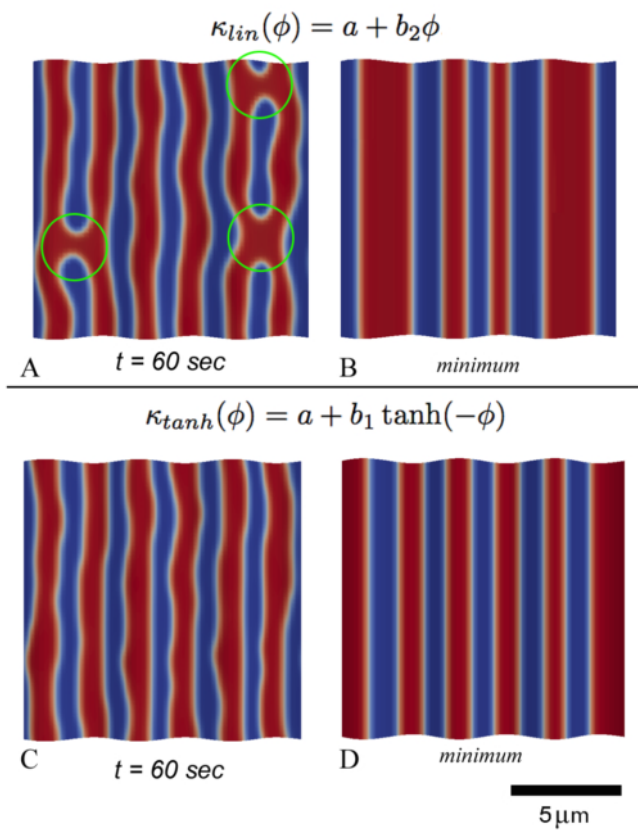


Figure 4.4: Different minimum patterns depending on the form of the function $\kappa(\phi)$. A-B: κ is linear; C-D: κ is a form of $a + b \tanh(-\phi)$. Note that early sorting in (A) is less curvature dependent than in (C), showing cross connections between the red domains (marked by green circles).

4.1.4.2 Gradients in the Elastic Moduli and Lateral Sorting

So far we have only studied the influence of lipids with differences in the bending rigidity $\kappa(\phi)$, which has previously shown to induce lateral sorting. In the following, we will also investigate the impact of spatial gradients in the spontaneous curvature H_0 and the Gaussian rigidity κ_G . Especially the latter has not been studied so far in the literature. For this purpose, the moduli are again assumed to be functions of the order parameter ϕ . Due to our results from the DPD studies we assume the rigidity functions $\kappa(\phi)$ as well as $\kappa_G(\phi)$ having the form $a + b_1 \tanh(-\phi)$. For the spontaneous curvature, we use the linear function $H_0(\phi) = a + b_2 \phi$. In further studies κ_G as well as H_0 should be identified from DPD studies or other molecular approaches. Furthermore, for the following simulations we choose for the geometry $\Gamma = \vec{X}(u_1, u_2) = 0.75 \sin(4\pi u_1) \sin(4\pi u_2) \mu\text{m}$ (cf. FIG 4.5 L) and $\langle \phi^0 \rangle = -0.6$. In the following, the notation Δh constitutes the difference $|h^A - h^B|$ in an elastic modulus $h \in \{\kappa, \kappa_G, H_0\}$ between the two species A and B.

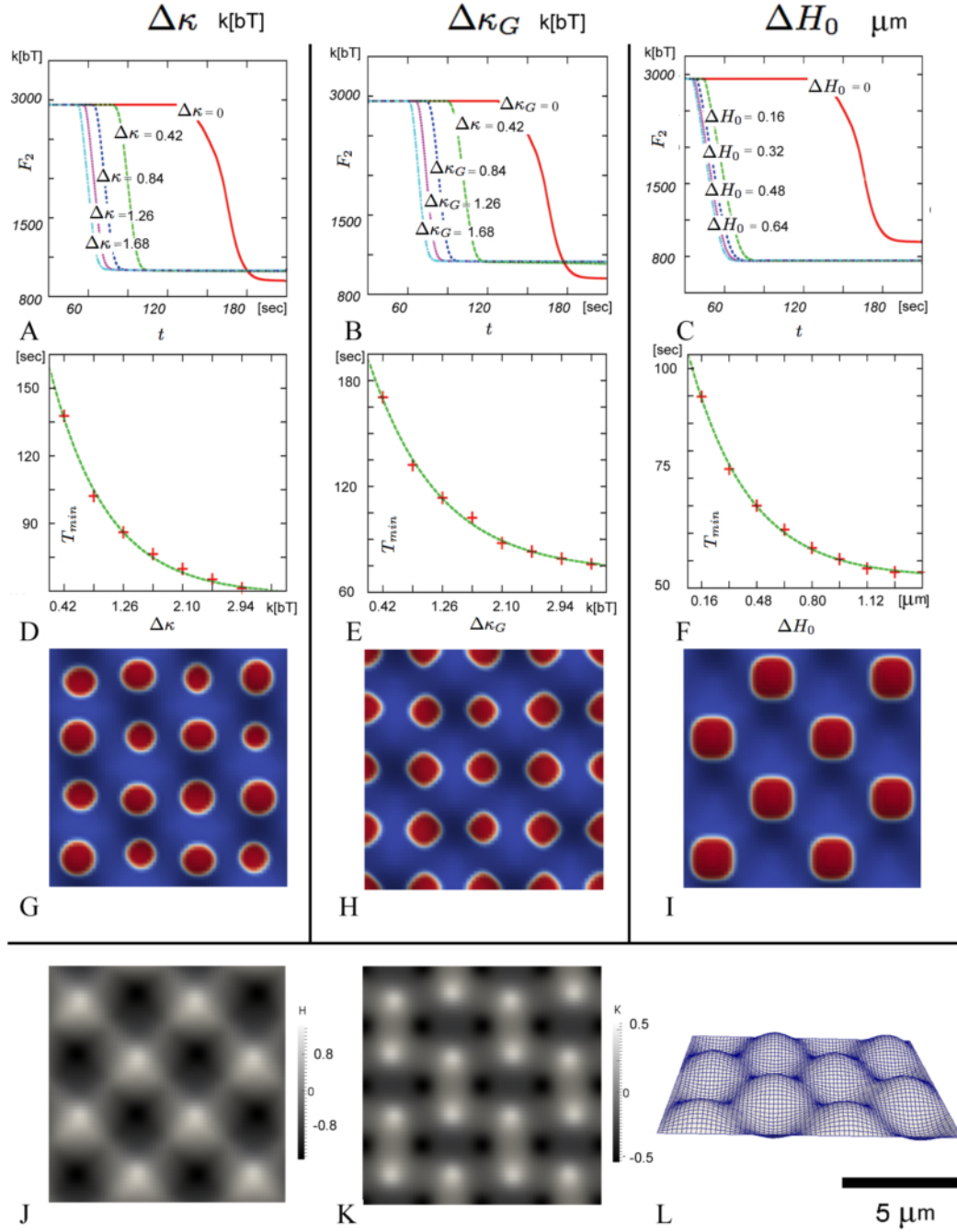


Figure 4.5: Investigating lateral sorting using different strengths of gradients in the elastic moduli $\Delta\kappa$ (A,D,G), $\Delta\kappa_G$ (B,E,H) and ΔH_0 (C,F,I) on a fixed non-planar surface. A-C: The decay of the Cahn-Hilliard energy F_2 in time. The stronger Δh ($h \in \{\kappa, \kappa_G, H_0\}$) is, the earlier is the observed decay of F_2 . D-F: The time up to the metastable pattern T_{min} decays exponentially with Δh (red dots: values from simulations; green spotted line: exponential fit of the kind $a + b \exp(-c\Delta h)$). G-I: Representative minimum patterns. J: Mean curvature of Γ . K: Gaussian curvature of Γ . L: Discretized surface Γ , side view.

Interestingly, by varying independently all three elastic moduli in our simulations, we observe in principle the same effects: the stronger Δh is, the faster phase separation occurs. This can be observed by an early and faster decay of the Cahn-Hilliard part F_2 of the free energy from the unstable initial conditions (c.f. FIG 4.5 A-C). Plotting the time to the achievement of the minimum T_{min} against Δh yields in all cases an exponential decay of $T_{min}(\Delta h)$ (c.f. FIG 4.5 D-F). The exponential fit leads to a good approximation for physically reasonable values. However, for significantly larger values we observe that T_{min} decays even stronger, without any offset.

In the case $\Delta\kappa = \Delta\kappa_G = \Delta H_0 = 0$, phase separation occurs randomly (results not shown). Considering gradients in each of the moduli we observe distinct curvature dependent phase separation patterns: choosing nonzero $\Delta\kappa_G$ induces phase separation of the component with the lower absolute value of κ_G in areas with high negative Gaussian curvature (FIG 4.5 H). Doing the same with $\Delta\kappa$ we observe phase separation of the component with the lower bending rigidity in regions with high mean curvature (FIG 4.5 G). Choosing $H_A < 0$ while $H_B = 0$ (causing $\Delta H_0 \neq 0$) drives ϕ_A to regions allocating this curvature (FIG 4.5 I). Interestingly, in most of the cases, these minimum patterns are only metastable, showing only slight changes in the size of the domains for a long time after T_{min} , but resulting very late ($t > 300$ min) in different minimum patterns with less and larger domains (c.f. Section 4.1.4.4).

The observed minimum patterns (c.f. FIG 4.5 G-I) differ significantly - each minimum pattern is the optimal pattern for the corresponding elastic modulus. Therefore, it is absolutely necessary to consider all three effects, since neglecting one part could lead to completely different minimum patterns and thus different biological interpretations.

4.1.4.3 Curvature Gradients and Lateral Sorting

Curvature depending sorting in membranes appears to be the result of the interplay between spatial gradients in the elastic moduli and in membrane curvature [193]. In the previous section, we have varied the strength of spatial moduli gradients keeping the membrane geometry constant. Analogously, in this section we vary the membrane geometry (i.e. the strength of curvature gradients) keeping differences in the elastic moduli constant. Corresponding results are shown in FIG 4.6. In order to quantify curvature gradients in mean curvature H and Gaussian curvature K , we define $H'_{max} := \max\{|\nabla^\Gamma[H(\vec{X})]| : \vec{X} \in \Gamma\}$ as well as $K'_{max} := \max\{|\nabla^\Gamma[K(\vec{X})]| : \vec{X} \in \Gamma\}$.

First, we fix for each elastic modulus $h \in \{\kappa, \kappa_G, H_0\}$ a certain difference $\Delta h \neq 0$ (while choosing vanishing differences in the other two moduli) but vary the corresponding curvature gradient $G'_{max} \in \{H'_{max}, K'_{max}\}$. We observe in all three cases that the stronger G'_{max} is, the earlier and faster phase separation occurs (c.f. FIG 4.6 A-C). Plotting the time to the achievement of the minimum T_{min} against the strength of G'_{max} yields in all cases an exponential decay of $T_{min}(G'_{max})$ (c.f. FIG 4.6 D-F).

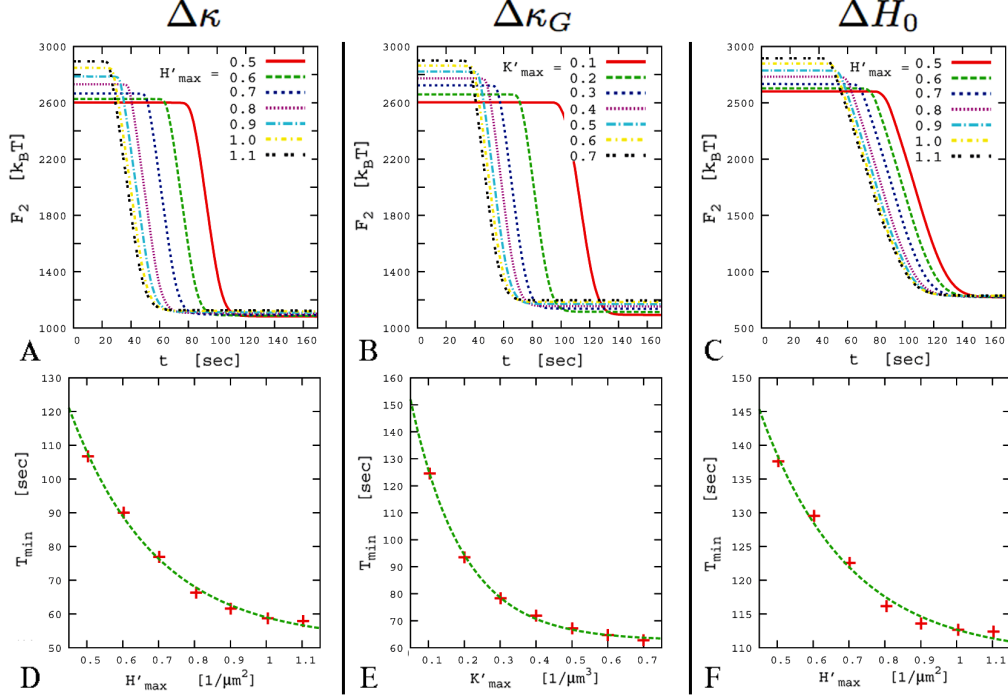


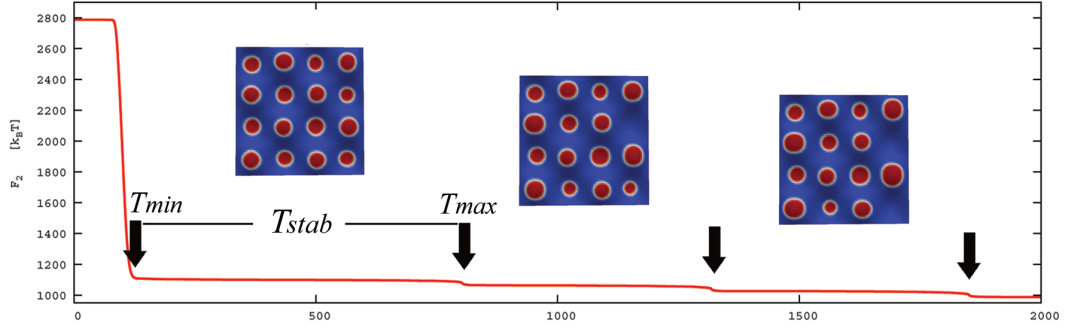
Figure 4.6: Investigating lateral sorting using different strengths of curvature gradients $G'_{max} \in \{H'_{max}, K'_{max}\}$ but fixed differences in the elastic moduli $\Delta\kappa \neq 0$ (A,D), $\Delta\kappa_G \neq 0$ (B,E) and $\Delta H_0 \neq 0$ (C,F). A-C: The decay of the Cahn-Hilliard energy F_2 in time. The stronger G'_{max} is, the earlier the observed decay of F_2 is. D-F: The time up to the metastable pattern T_{min} decays exponentially with G'_{max} (red dots: values from simulations; green spotted line: exponential fit of the kind $a + b \exp(-c\Delta h)$).

In detail, we have set $\Delta\kappa = 0.02k_B T$ and $\Delta\kappa_G = \Delta H_0 = 0$ in FIG 4.6 A and D; $\Delta\kappa_G = 0.02k_B T$ and $\Delta\kappa = \Delta H_0 = 0$ in FIG 4.6 B and E as well as $\Delta H_0 = 0.08\mu m^{-1}$ and $\Delta\kappa = \Delta\kappa_G = 0$ in FIG 4.6 C and F.

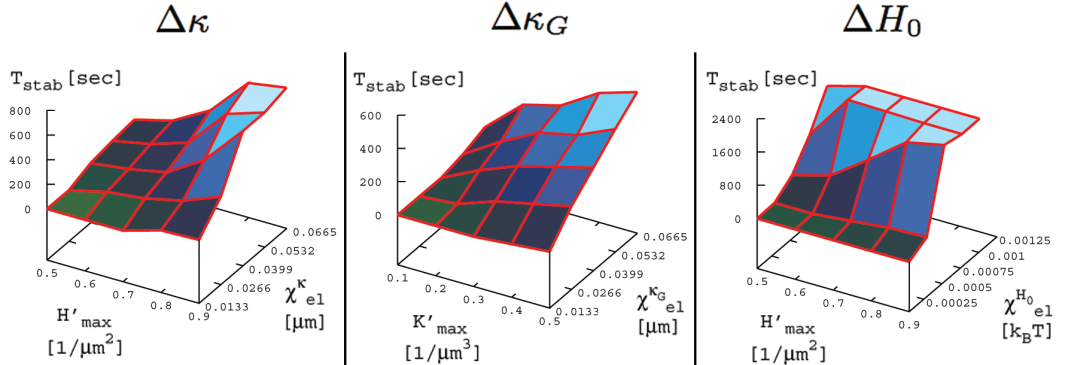
Hence, increasing differences in elastic moduli as well as increasing gradients in membrane curvature accelerate the lateral sorting process exponentially.

4.1.4.4 Parameter Interplay and its Influence on the Stability of Sorting Patterns

As mentioned above, most of the observed curvature depending patterns appear to be metastable: if differences in elastic moduli and curvature gradients are strong enough, a periodic symmetric pattern appears at $t = T_{min}$, which loses at $t = T_{max}$ its symmetry by fusing into less and bigger domains. The latter can be observed by a jump in the free energy F_2 (c.f. FIG 4.7 A). This process continues stepwise; the assumed stable minimum pattern is built up of one big domain. To quantify the stability of a curvature modulated pattern, we define $T_{stab} := T_{max} - T_{min}$ which equals to zero if no curvature depending sorting takes place. In order to quantify the mechanochemical disposition for curvature modulated sorting subject to line tension



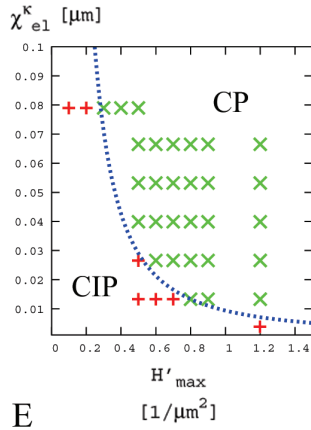
A



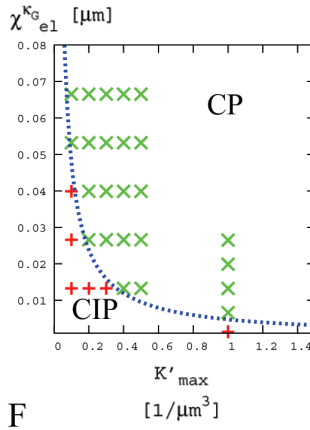
B

C

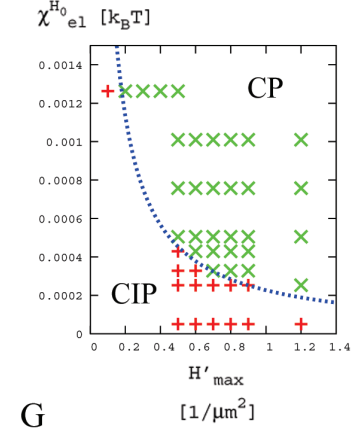
D



E



F



G

Figure 4.7: Stability of patterns depending on the interplay of elastic moduli gradients, curvature gradients and the line tension. A: $T_{stab} := T_{max} - T_{min}$ measures the stability of a curvature modulated pattern, where T_{max} defines the time where the symmetry of the pattern gets lost by fusing domains. Each fusion can be recognized by a jump in the free energy F_2 (black arrows). B-D: for each $h \in \{\kappa, \kappa_G, H_0\}$, T_{stab} increases with growing curvature gradient H'_{max} and K'_{max} , respectively, as well as with growing corresponding elastic parameter $\chi_{el}^h = \Delta h/\sigma$ (in figure D the value T_{stab} has been cutted at $T_{stab} = 2400$ sec due to limited simulation time). E-G: Phase diagrams as a function of the elastic parameter χ_{el} for each elastic modulus and the corresponding curvature gradient. CP: region with (metastable) curvature modulated sorting, CIP: region with curvature independent sorting. Green x-marks: simulations with $T_{stab} > 0$, red + -marks: simulations with $T_{stab} = 0$. Blue dotted line: heuristically fitted transition line of the kind $a/x + b/x^2$.

and modulus differences, for each $h \in \{\kappa, \kappa_G, H_0\}$ we introduce the elastic parameter $\chi_{el}^h = \Delta h / \sigma$ [212]. We systematically investigate the influence of gradients in elastic moduli, line tension and curvature gradients on the stability T_{stab} . For this purpose, for each modulus h and the corresponding curvature gradient $G'_{max} \in \{H'_{max}, K'_{max}\}$ we have performed ≥ 30 simulations with different parameter sets (G'_{max}, χ_{el}^h) . Our results clearly show that increased values for G'_{max} as well as for χ_{el}^h result in an increased stability T_{stab} (c.f. FIG 4.7 B-D).

For each $h \in \{\kappa, \kappa_G, H_0\}$ we present phase diagrams, showing regions with at least metastable curvature modulated pattern formation (CP) and curvature independent sorting regions (CIP) relying on χ_{el}^h and the corresponding $G'_{max} \in \{H'_{max}, K'_{max}\}$ (c.f. FIG 4.7 E-G). Hence, we assume that the relation $\chi_{el}^h = f_{tr}^h(G'_{max})$ describing the transition between CP and CIP regions can be approximated by $f_{tr}^h(G'_{max}) = a/G'_{max} + b/(G'_{max})^2$ for $a, b \in \mathbb{R}_{\geq 0}$. This is physically motivated by the assumption that the *graph*(f_{tr}^h) asymptotically approaches the axes. Based on our numerical simulations, heuristic fits yield rough approximations of \tilde{f}_{tr}^h (blue spotted lines in FIG 4.7 E-G). Especially it holds $f_{tr}^\kappa(H'_{max}) = 0.0043/H'_{max} + 0.0052/(H'_{max})^2$, $f_{tr}^{\kappa_G}(K'_{max}) = 0.0048/K'_{max}$ as well as $f_{tr}^{H_0}(H'_{max}) = 0.00023/H'_{max}$. In future experiments these functions can be used to estimate if curvature modulated sorting will occur. This is the case namely if for at least one elastic modulus h the relationship $\chi_{el}^h \gg f_{tr}^h(G'_{max})$ holds for the corresponding value $G'_{max} \in \{H'_{max}, K'_{max}\}$.

4.1.5 Discussion

In the Section 4.1 we have outlined a continuous multiscale model for curvature induced lateral sorting in biological membranes. Passive lateral organization in membranes is involved and actually is a premiss for various cellular processes, such as budding [18], signaling [233] and sorting [140]. Furthermore, it is assumed to be an essential condition for the biogenesis and maintenance of cellular organelles [175]. Thus it is critical for the function of each biological cell. The presented model enables to study how differences of membrane components in at least one of the macroscopic elastic moduli influence dynamics and the selection of minimum patterns. Here, we have studied the influence of curvature gradients in interplay with the bending rigidity κ , the spontaneous curvature H_0 and the Gaussian rigidity κ_G . The latter has not been studied in the literature so far. In terms of molecular parameters, the different elastic moduli reflect differences in stiffness and shape of the corresponding molecules.

Differences in the elastic moduli have been experimentally used to study the interplay between molecular properties and curvature [18, 107, 125, 193, 196, 210, 239, 262]. Furthermore, various theoretical continuous approaches have already been used to study the coupling of different moduli with curvature [5, 45, 83, 120, 146, 155, 237, 248, 260]. Despite of this effort, three points have not been studied so far (at least up to our knowledge):

- Parameterization of the presented continuous model directly from the molecular scale.
- Studies of the influence of differences in the Gaussian rigidities on lateral sorting.
- Phase diagrams estimating if and how stable a curvature depending sorting occurs.

In this thesis, we have addressed these three issues.

First of all, we have studied the influence of the detailed parameterization, i.e. the functional dependencies used in the model. In collaboration with Jens Kühnle [131] we have used discrete DPD models to determine the dependence of the bending rigidity $\kappa(\phi)$ on the composition of a binary lipid bilayer. We have restricted ourselves to lipids of the same length and type yet varied the lipids chain stiffness. Simulation results reveal that $\kappa(\phi)$ is best described by a sigmoid curve, e.g. having a hyperbolic tangent form.

In the macroscopic finite element simulations, we have found that the steady state depends strongly on $\kappa(\phi)$. In FIG 4.4 the dynamics and minimum configurations of two simulations are shown comparing the use of a linear bending rigidity $\kappa_{lin}(\phi)$ with the nonlinear case $\kappa_{tanh}(\phi)$. The latter has been determined directly from DPD studies. Although the global energy F of a given lateral distribution ϕ on Γ is the same for the two cases $\kappa_{lin}, \kappa_{tanh}$, we observe strong differences in dynamics and minimum patterns. We postulate that this effect is due to differences in $\frac{d}{d\phi}\kappa_{lin}$ and $\frac{d}{d\phi}\kappa_{tanh}$, leading locally (and very early in time) to differences in the strength of curvature dependent sorting. This again traps the whole system in completely different minimum patterns. These results emphasize the importance of dynamics and parameters in mathematical modeling. In other words, even if only minimum patterns (with a certain set of parameters) are studied, the dependence of the minimum configuration on initial conditions should be carefully checked as well as the robustness with respect to parameter variation.

Furthermore, we have investigated the impact of differences in each of the macroscopic elastic moduli on lateral sorting using macroscopic finite element simulations (c.f. FIG 4.5). Our results suggest that each of the moduli κ , H_0 and κ_G has a comparable impact on dynamics and curvature dependent patterns: in the parameter regime studied, the decomposition time decreases roughly exponentially with the gradient of each elastic modulus. The same effect can be observed by fixing the difference in each elastic modulus and increasing corresponding curvature gradients (c.f. FIG 4.6). Additionally, each gradient can lead to a distinct minimum pattern, influenced by the mean curvature or the Gaussian curvature of the given geometry, respectively. These findings suggest that the Gaussian rigidity plays an equivalent role in lateral

sorting, as the other two moduli, which are well known to influence lateral sorting [5, 18, 45, 72, 107, 120, 125, 146, 155, 193, 196, 210, 237, 239, 248, 260, 262].

The presented results agree with the following molecular intuition: given an arbitrary curved membrane containing a stiff and a flexible component, it is energetically favorable for the most flexible component to stay in curved regions, independent of the sign of the principle curvatures. To account for each kind of curvature, we have to consider both, gradients in the bending rigidity and in the Gaussian rigidity.

These findings are supported by the experimental observation that differences in bending rigidities usually coincide with differences in Gaussian rigidities [220]. The importance of the elusive Gaussian rigidity in biological processes has been neglected for a long time. Only very recently theoretical studies investigate its influence on membrane shapes [17, 30, 60], fusion [225] and lateral diffusion [263] considering either a homogeneous membrane composed of only one component or - in the case of two component membranes - domains composed of different molecular species have been assumed to be lateral immobile. In experiments investigating lateral sorting, effects due to Gaussian rigidities are also generally assumed to be negligible [262]. This may be caused by the fact that, on the one hand, κ_G cannot be measured directly in experiments [226]. On the other hand, the well known Gauss-Bonnet theorem (stating $\int_S K d\omega = \text{const.}$ in homogeneous materials considering closed membranes) may have led to a misunderstanding that the effect of K is negligible in heterogeneous membranes as well. However, the results presented in this study show that the impact of inhomogeneities in Gaussian rigidities have a comparable strong effect on lateral sorting as the other two moduli, the bending rigidity and the spontaneous curvature.

The results presented in FIG 4.7 show that the appearance and stability of curvature modulated patterns strongly depend on the exact choice of line tension, curvature gradients and moduli gradients. It appears the question if beside metastable patterns also stable curvature modulated patterns exist. However, this question has to be traced by methods of rigorous stability analysis and is far beyond the scope of this thesis. Nevertheless, the presented phase diagrams in this study allow to estimate, at least, under which conditions curvature modulated sorting takes place.

In the future, all these findings can help to understand, predict and interpret more precisely experimental observations concerning curvature dependent lateral organization and its stability in biological membranes.

4.2 Impact of Elastic Parameters on Membrane Budding

4.2.1 Introduction

A biological cell is composed of a multitude of membrane systems. Each of these systems provides a specific shape and composition of chemical components fulfilling highly specialized functions. Although most of these systems are physically well separated they are connected among each other via permanent flow of membrane parts. This happens due to small membrane spheres, called vesicles, constricting from a donor membrane in a process called budding. Budding plays a key role in various healthy and pathogenic cellular processes such as sorting, transport, biogenesis and infections [116, 175, 249].

In vivo, biological membranes are composed of many different lipids, proteins and other molecules [4]. Recent experiments show that the lateral phase separation or clustering of certain membrane components serves as a basal mechanism to produce local membrane deformations, e.g. buds [12, 17, 18, 245]. Although most of the budding process details still remain unknown, it is assumed that the mechanical properties and interactions of different membrane molecules play a crucial role in budding processes. (For further details concerning basic properties of biological membranes as well as concerning previous general work in the field of membrane modeling, we refer to Section 2.1.1 and Section 2.3, respectively.)

In this section, the impact of each elastic parameter (the line tension, bending rigidity, Gaussian rigidity, spontaneous curvature and monolayer area-difference) on membrane shape and budding is investigated, using the basic model (c.f. Section 2.4) as well as the corresponding computational approach (c.f. Chapter III). Various simulation results are compared to recent theoretical results (sharp line tension limit) as well as experimental results. Since within this section most of the studies are qualitative, we work with abstract nondimensionalized model parameters in place of physical values (contrary to Section 4.1 and Section 4.3). The presented section is closely related to [166].

4.2.2 Finite Element Approximation and Parameter Setup

Since the strongly coupled nonlinear PDE system of fourth order (2.8)-(2.10) (c.f. Section 2.4.3) can hardly be investigated using analytical techniques, it will be investigated in detail using numerical studies. Here, we will use the finite element library Gascoigne [19] using bilinear finite elements. Details of the numerical approach adopted here are shown in Chapter III.

If not otherwise stated we will use the parameter setup given below. For time discretization we use an adaptive time stepping scheme starting with $\tau_0 = 10^{-5}$. Local expansion of the grid due to an evolution of the membrane is avoided using local mesh refinement starting with $J = 1024$ vertices. Initial conditions for mem-

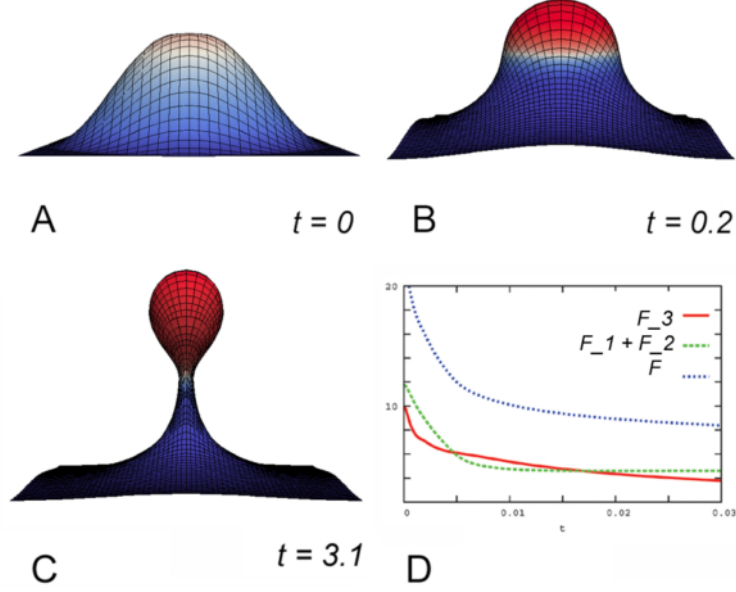


Figure 4.8: A-C: Typical simulation snapshots of a deforming two-component membrane at different time steps (red = local high concentrations of species A, blue = local high concentrations of species B). D: Corresponding decay of different parts of the free energy.

brane shapes and lateral composition are given by $\vec{X}^0 = (0, 0, a_1(1 + \cos(a_2\pi)))$ and $\phi^0 = -1 + a_3 \cos(a_2\pi)$, where the constants a_1, a_2, a_3 are chosen so that $\int_{\Gamma} ds = 1.3$ and $\int_{\Gamma} \phi ds = -0.85$. For all variables, periodic boundary conditions are used. (However, it appears that using Neumann zero boundary conditions leads to the same qualitative and quantitative results.) As not otherwise stated, we set: $\kappa^A = \kappa^B = 1.5$, $\kappa_G^A = \kappa_G^B = -1$ (ensuring the stability restriction $0 \geq \kappa_G \geq -2\kappa$ [216]), $\bar{\kappa} = 0$, $\sigma = 90$, $\xi = 0.03$, $f(\phi) = \frac{9}{32}(\phi^2 - 1)^2$, $L_X = 5 \cdot 10^{-4}$ and $L_\phi = 0.05$. Furthermore, for $i \in \{1, 2\}$ we choose $\alpha_i^m \equiv \beta_i^m \equiv 0.1$. Elastic moduli are assumed to be linear functions of ϕ , i.e. $h(\phi) = \frac{h^A + h^B}{2} + \frac{h^A - h^B}{2}\phi$, where h^A and h^B are the macroscopic elastic moduli of the molecular species A and B in Γ , $h \in \{\kappa, \kappa_G, H_0\}$.

In FIG 4.8 A-C snapshots at different time steps of a typical simulation are shown. Furthermore, the corresponding decay of different parts of the free energy (2.5) is shown in FIG 4.8 D. In case of energy minimizing geometries consisting of an incomplete bud (e.g FIG 4.9 D) the achievement of the local minimum of F can be evaluated naturally by the corresponding discretized derivative, i.e. by $\frac{F[\vec{X}^{m+1}, \phi^{m+1}] - F[\vec{X}^m, \phi^m]}{\tau^{m+1}}$. If the minimum is reached, the simulation is stopped. In case of a complete budding event (e.g. FIG 4.9 E) the energy minimizing shape contains an infinitesimal narrow neck and thus is beyond discrete approximations. Hence, we stop simulations just before the numerically computed solutions "blow up" due to geometric singularities knowing that we are close to the energy minimum. The limit represents the fission of a daughter vesicle from the underlying membrane. This is also the limit of our mathematical model in different senses: beside the topological limit, the process of

fission itself includes several complex and partial unknown stages of membrane reorganization [129, 142] which are not considered in our model.

4.2.3 Numerical Results

Using the outlined macroscopic modeling approach (Section 2.4) discretized by the scheme described in Chapter III, we investigate dynamics and minimum configurations of the deformation of two-component membranes in this section. Particularly, we study membrane shape and budding transition by varying:

- the line tension σ acting along the phase boundaries and thus tending to shorten the boundary length,
- the spontaneous curvatures H_0^A and H_0^B modeling an explicit coupling between different components and the preferred membrane curvature,
- the bending rigidities κ^A and κ^B reflecting an explicit coupling of different components with the stiffness of the membrane,
- the Gaussian rigidities κ_G^A and κ_G^B reflecting again an explicit coupling of different components with the stiffness of the membrane, and
- the monolayer area difference modulus $\bar{\kappa}$, reflecting that different components may influence the global area difference between the two monolayers in different ways.

Corresponding results are qualitatively and quantitatively compared in detail and discussed in context of recent experimental and theoretical results.

In contrast to the often used sharp line tension approaches, which assume axially symmetric geometries with already separated phases (e.g. [6, 17, 60, 124]), the presented approach is not restricted to specific geometries (except topological changes) and includes lateral dynamics as well as a variable interface width. Hence, this approach can be used to study the complex interplay of membrane geometry and lateral dynamics in membranes on different scales. Therefore, it is well suited for a comparison with models on the molecular level, e.g. molecular dynamics (MD). The latter can be used for a computational upscaling approach of membrane models, as pursued in Section 4.1. In the future, the presented dynamical computational approach could help to get further insights how all the various shaped and beautiful membrane structures are generated and maintained.

4.2.3.1 Line Tension σ

Clustering of various different molecule species (e.g. mixtures of lipids and cholesterol or lipids and proteins) into distinct membrane domains has been shown for

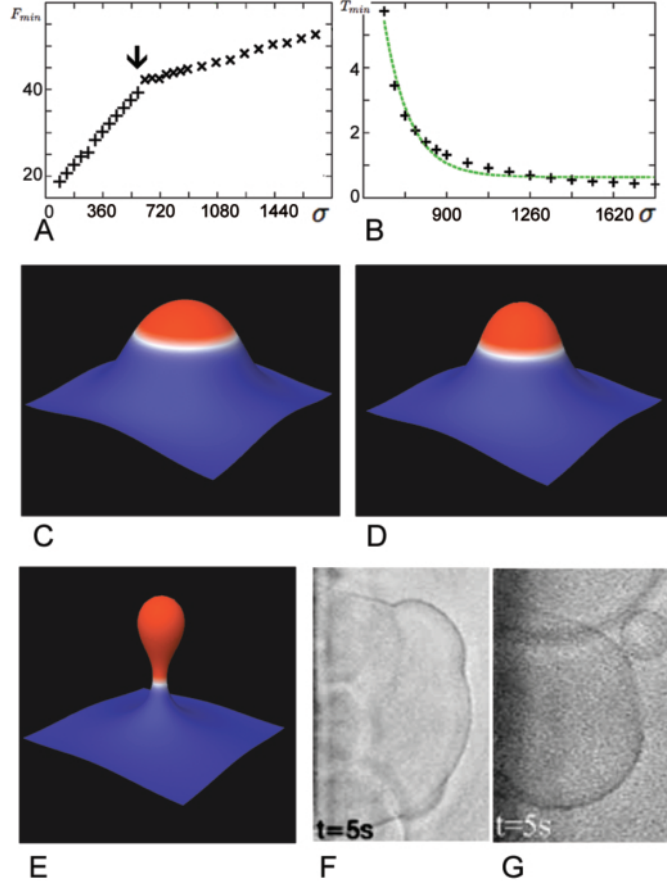


Figure 4.9: The effect of the line tension σ on membrane budding. A: Functional dependence of the free energy F_{min} of the minimum configuration on σ . Black dots: simulation data; arrow marks budding transition. B: The budding time T_{min} decays exponentially with increasing σ ; black dots: values from simulations; green spotted line: exponential fit. C-E: Minimum configurations for different values of σ , C: $\sigma = 90$, D: $\sigma = 540$, E: $\sigma = 630$. F-G: Budding experiments (pictures reprinted from [231], © 2004, with permission from Elsevier) with assumed weak (F) and strong (G) line tension.

different types of biological membranes [12, 17, 18, 245]. The detailed underlying molecular interactions are still a topic of active research [91]. Here, we are integrating this lateral demixing behavior by the effective parameter σ describing the (diffuse) line tension.

In this section, we investigate the effects of different values of $\sigma \in [90, 1800]$ on membrane shapes and budding. In FIG 4.9 we show minimum geometries for $\sigma = 90$ (C), $\sigma = 540$ (D) and $\sigma = 630$ (E). Our results clearly indicate that the line tension plays an important role in the budding process: with increasing line tension the membrane shows an increasing budded geometry (c.f. FIG 4.9 C-D). For $\sigma \geq 630$ we observe a qualitative change in the minimum configuration: the minimum shape of an incomplete bud (c.f. FIG 4.9 D) changes abruptly to the shape of a complete

bud (c.f. FIG 4.9 E). This observation of a budding transition above a critical value σ^* fits well with the theoretical studies of [123, 124, 150] and experimental results of [231] (c.f. FIG 4.9 F-G). Calculating the critical sharp line tension value σ_{si}^* obtained by [150] for equal domain sizes and transformation in the diffuse value (c.f. Appendix B) yields $\bar{\sigma}^* \approx 711$, close to our numerically estimated value.

Although the minimum geometry of the membrane changes discontinuously at σ^* , the corresponding free energy $F_{min}(\sigma)$ does not show any jump at $\sigma = \sigma^*$ (c.f. FIG 4.9 A, black arrow), indicating that at σ^* the free energy of the incomplete bud and of the energy of the complete bud are the same, as proposed by [150]. Once $\sigma \geq \sigma^*$, F_{min} grows linearly, since the minimum geometry is unchanged and F scales linearly with σ . Plotting the budding time $T_{min}(\sigma)$ for $\sigma \geq \sigma^*$ reveals that the budding duration is shortened with increasing line tension, which has been previously observed in dissipative particle dynamics studies [112]. A fit reveals an exponential decay of $T_{min}(\sigma)$ (c.f. FIG 4.9 B).

Beside the previously assumed role of the line tension energy as a control mechanism of membrane shapes and budding [136, 150, 231, 245, 248, 264], our results emphasize the influence of this parameter also on the relevant time scales.

4.2.3.2 Spontaneous Curvature H_0

A variety of molecular curvature generating mechanisms in biological membranes have been proposed in the past (for reviews see [89, 159, 161]): global quantities (such as area difference between lipid monolayers [169] or area/volume ratio of vesicles [69]) as well as local accumulations of shaping components [269] can induce local curvatures. In this subsection, we limit ourselves to the latter case, by modifying the spontaneous curvature H_0 . Strongly nonzero spontaneous curvatures have been described for various membrane proteins, classical examples are clathrin and COP molecules [23, 24, 160, 195]. Also, for different lipids various effective spontaneous curvatures have been determined [269].

In this section, we consider the effect of different spontaneous curvatures $H_0^A \in [-15, 0]$ (keeping $H_0^B = 0$) on domain shapes and budding. Corresponding results are shown in FIG 4.10. As expected, increasing the spontaneous curvature H_0^A results in a domain adapting its curvature to the value of H_0^A (c.f. FIG 4.10 C-D). Above a critical value $-8.5 \leq H_0^{A*} < -8$ budding transition occurs, i.e. we obtain a shape close to complete bud with an infinitesimal small neck still connected to the rest of the membrane (as already stated our Lagrangian approach can not handle topology changes). These results match with the predictions of [123] stating that, even for a vanishing line tension, the spontaneous curvature alone can cause a complete budding.

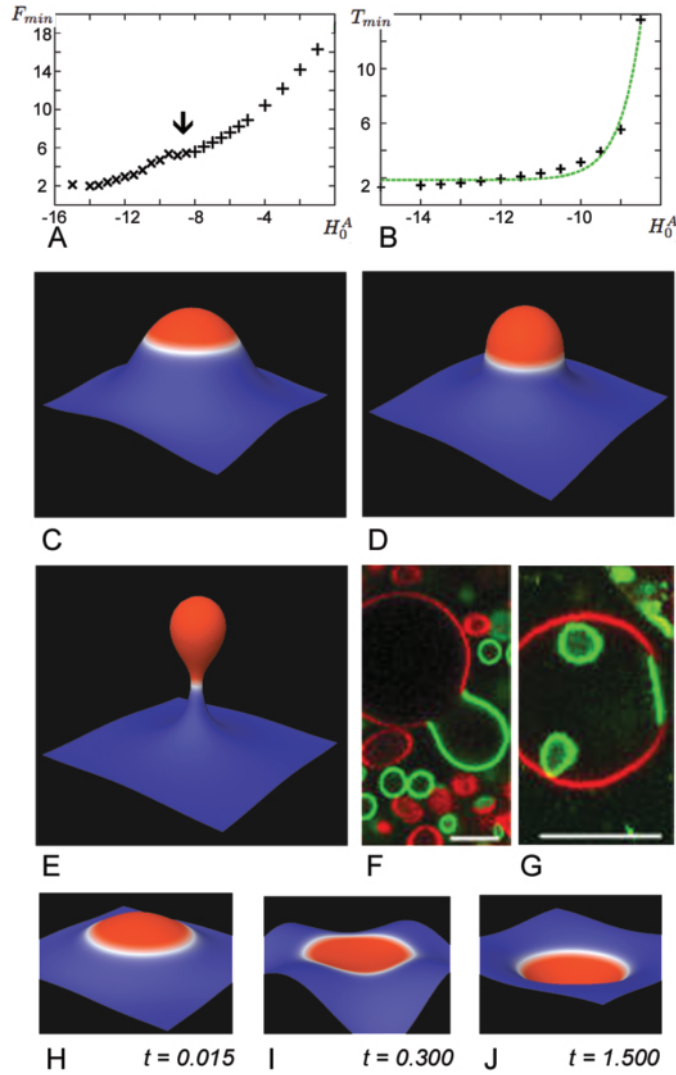


Figure 4.10: The effect of the spontaneous curvature H_0^A on membrane budding. A: Functional dependence of the free energy F_{min} of minimum configurations on H_0^A . Black dots: simulation data; arrow marks budding transition. B: The budding time T_{min} decays exponentially with decreasing H_0^A ; black dots: values from simulations; green spotted line: exponential fit. C-E: Minimum configurations for different values of H_0^A , C: $H_0^A = 0$, D: $H_0^A = -8$, E: $H_0^A = -8.5$. F-G Experimental results: different sterol structures induce different directions of budding (pictures are taken with permission from the National Academy of Sciences, [12], © 2005), H-J: time snapshots of a simulation with $H_0^A = 5$.

Calculating the critical spontaneous curvature \overline{H}_0^{A*} following the approach of [150] for equal domain sizes (c.f. Appendix B for transition between sharp and diffuse line tension) yields $\overline{H}_0^{A*} \approx -4.2$. In other words, \overline{H}_0^{A*} is of the same order, however not very close to the value H_0^{A*} numerically estimated in this study. Plotting the free energy $F_{min}(H_0^A)$ of the minimum geometries for different values of H_0^A does not reveal any discontinuity of F_{min} in H_0^{A*} (c.f. FIG 4.10 A black arrow). When $|H_0^A| \geq |H_0^{A*}|$, F_{min} grows quadratically, since the minimum shape is unchanged and F scales quadratically with $(H_0^A - H)$. Plotting the simulation time T_{min} up to the full bud (i.e. $|H_0^A| \geq |H_0^{A*}|$) reveals an exponential acceleration of the budding process by increasing further H_0^A (c.f. FIG 4.10 B).

To stress the influence of the spontaneous curvature on the budding direction, we further perform simulations in which the sign of H_0^A was opposed to the initial local curvature of the membrane choosing $H_0^A = 5$ (c.f. FIG 4.10 H-J). a_1 , a_2 and a_3 are chosen so that $\int_{\Gamma} ds = 1.08$ and $\int_{\Gamma} \phi ds = -0.55$. All other elastic parameters remain constant: $\kappa \equiv 10 \equiv -\kappa_G$ and $\sigma = 900$. We observe that also in this case the spontaneous curvature is able to induce a budding process opposite to the natural bending of the membrane.

Besides an influence of the spontaneous curvature on budding transition and the time scale of the budding event itself, our results highlight that the sign of the spontaneous curvature could be an important mechanism to control the direction of budding. This could explain how budding in both directions of the same membrane could be achieved, since in this case neither the area/volume ratio nor an area difference in one of the bilayer leaflets can positively influence both budding directions.

Our theoretical predictions are in accordance with the experimental results of [12], reporting a correlation between molecule structure and budding direction (c.f. FIG 4.10 F-G).

4.2.3.3 Bending Rigidity κ

The molecular origin of the macroscopic bending rigidity κ is still a field of active research [22, 42, 45, 46, 133, 184, 190, 204, 251]. Its exact role in basic biological processes such as membrane shaping and budding has not been completely understood yet. Experimentally, κ can be measured via fluctuations analysis of vesicles [109] based on Helfrich's theory [218] - exactly the same way as in the DPD studies in Section 4.1.

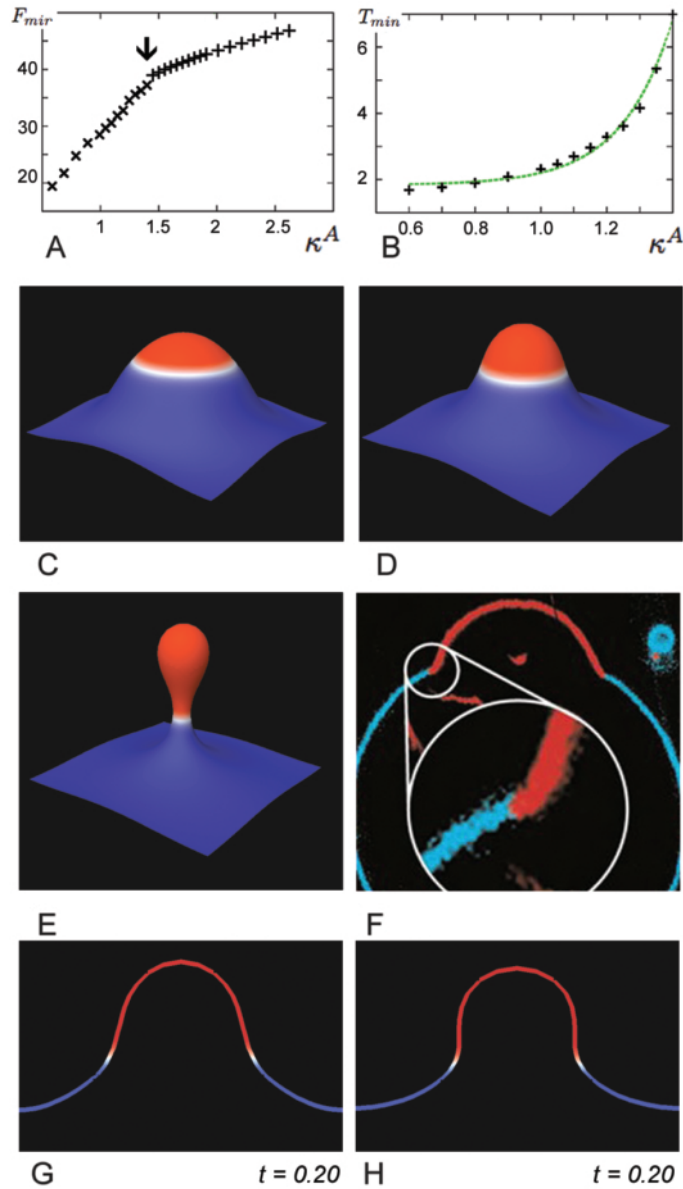


Figure 4.11: The effect of the bending rigidity κ^A on membrane budding. A: Functional dependence of the free energy F_{min} of the minimum configurations on κ^A . Black dots: simulation data; arrow marks budding transition. B: The time T_{min} up to the complete bud decays exponentially decreasing κ^A ; black dots: values from simulations; green spotted line: exponential fit. C-E: Minimum configurations depending on κ^A , C: $\kappa^A = 2.6$, D: $\kappa^A = 1.45$, E: $\kappa^A = 1.4$. F-H: The phase with the higher κ straightens close to the phase boundary, hence neck induced curvature is stronger in the phase with the lower κ . F: Experimental result: red component has a lower value of κ (reprinted by permission from Macmillan Publishers Ltd: Nature, [18], © 2003); G-H: simulation snapshots; G: $H^A = 5$ but $H^B = 1$ shows a less spherical bud than H: $H^A = 1$ but $H^B = 5$.

In this section, we consider the effect of the bending rigidity κ on budding choosing different values $\kappa^A \in [0.6, 2.6]$ and keeping $\kappa^B = 1.5$ and $\sigma = 585$ constant. Corresponding results are shown in FIG 4.11. We find that a strong bending rigidity $\kappa^A = 2.6$ flattens the domain of the corresponding component (c.f. FIG 4.11 C) whereas a weaker value $\kappa^A = 1.45$ causes a more budded minimum geometry (c.f. FIG 4.11 D). Adopting an energetic point of view, in the latter case bending within the domain is less penalized. Furthermore, we observe that stiffening the domain (choosing $H^A = 5$ but $H^B = 1$) straightens the domain at the phase boundaries of species A and B resulting in a less spherical bud than in the case of $H^A = 1$ but $H^B = 5$. Curvature at the neck is more pronounced in the domain, where κ value is lower (c.f. FIG 4.11 F-H). This is in accordance with recent experimental and theoretical observations [17, 18].

Lowering κ^A below a critical value $\kappa^{A*} = 1.4$ induces a discontinuous budding transition, resulting in a minimum geometry consisting of a complete bud (c.f. FIG 4.11 E). This fits quite well with the results of [150]. Calculating the critical value $\bar{\kappa}^{A*}$ for equal domain sizes in the sharp line tension approach of [150] (for transformation between the diffuse and the sharp line tension value c.f. Appendix B) yields $\bar{\kappa}^{A*} \approx 1.23$, which is of the same order as the value estimated numerically by us.

The free energy $F_{min}(\kappa^A)$ of the minimum configuration shows a kink at the critical value κ^{A*} (c.f. FIG 4.11 A, black arrow). It grows up linearly for $\kappa^A \leq \kappa^{A*}$ as expected, the minimum geometry is unchanged and F scales linearly with κ^A . Furthermore, we observe that for values $\kappa^A \leq \kappa^{A*}$ the time up to the full bud $T_{min}(\kappa^A)$ decays exponentially with further lowering of κ^A (c.f. FIG 4.11 B). These results emphasize that the bending rigidity plays a qualitatively equivalent role in the process of budding transition and dynamics such as the spontaneous curvature and the line tension.

4.2.3.4 Gaussian Rigidity κ_G

Theoretical approaches show that differences in molecular properties cause differences in the macroscopic membrane Gaussian rigidity κ_G [22, 42, 209, 251]. Considering heterogeneous membranes, it has been early predicted that lateral gradients in the Gaussian rigidity may influence membrane shape and budding [123, 124]. Since κ_G cannot be determined directly in experiments [226] recent studies focusing on κ_G combine experiments with simulations [6, 17, 30, 60]. These studies usually use a sharp interface approach for the line tension (assuming a large scale). Furthermore, they consider fixed and already formed phases as well as axially symmetric geometries. The actual process leading to the formation of buds is ignored.

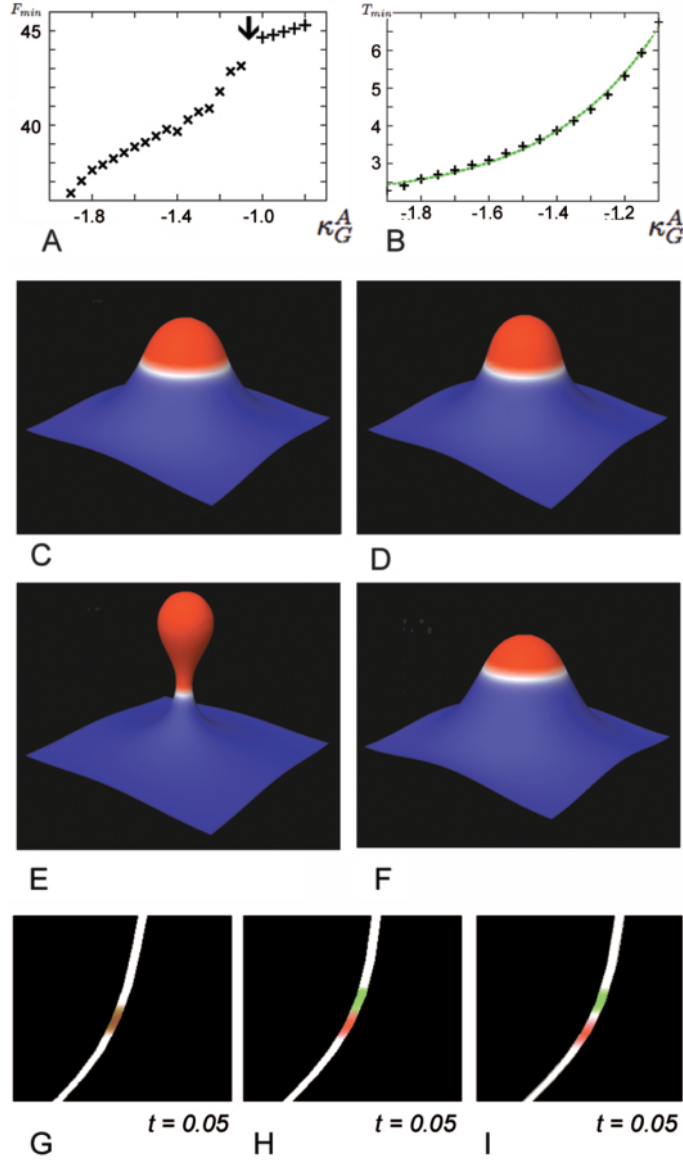


Figure 4.12: The effect of the Gaussian rigidity κ_G^A on membrane budding. A: Functional dependence of the free energy F_{min} of the minimum configurations on κ_G^A . Black dots: simulation data; arrow marks budding transition. B: the budding time T_{min} decays exponentially with decreasing κ_G^A ; $|\kappa_G^A| \geq |\kappa_G^{A*}|$. Black dots: simulation data; green spotted line: exponential fit. C-F: minimum configurations, C: $\kappa_G^A = -0.8$, D: $\kappa_G^A = -1.15$, E: $\kappa_G^A = -1.4$. F: same values expect a lower domain size compared to (E). G-I: shift of the neck region (cross-section) relative to the phase boundary due to differences in κ_G ; maximum values of Gaussian curvature K are marked in green, maximum values of $\nabla^\Gamma \phi$ are marked in red, overlay appears brown; G: $\kappa_G^A = -3.0$, H: $\kappa_G^A = -1.5$, I: $\kappa_G^A = 0.0$.

In the current section we address the influence of differences in the Gaussian rigidity κ_G on the membrane shape and budding, choosing different values of $\kappa_G^A \in [-2, -0.8]$ and keeping $\kappa_G^B = -1.5$ and $\sigma = 675$ constant. Corresponding results are shown in FIG 4.12. Starting with $\kappa_G^A = -0.8$, we find incomplete budded minimum geometries (c.f. FIG 4.12 C-D). For $\kappa_G^A \leq -1.2$ a budding transition occurs causing a minimum geometry of a complete bud (c.f. FIG 4.12 E). These results fit well with the assumptions of [124]. Furthermore, reducing the size of the domain A by choosing a_3 so that $\int_{\Gamma} \phi ds = -0.95$ and keeping $\kappa_G^A = -1.4$ and $\sigma = 675$ constant, we find that budding is inhibited (c.f. FIG 4.12 F). The latter effect holds for all elastic parameters inducing budding in the original setting with $\int_{\Gamma} \phi ds = -0.95$ (results not shown) which matches the observations of [123].

At the critical budding transition value κ_G^{A*} (c.f. FIG 4.12 A, black arrow) the free energy $F_{min}(\kappa_G^A)$ (corresponding to the minimum configurations) shows a well established kink. For values $|\kappa_G^A| \geq |\kappa_G^{A*}|$, F_{min} increases linearly since the minimum geometry is unchanged and F scales linearly with κ_G^A . Plotting the corresponding simulation time $T_{min}(\kappa_G^A)$ reveals an exponential acceleration of the budding process due to further lowering of κ_G^A (c.f. FIG 4.12 B).

Our results clearly show that differences in the Gaussian rigidity can play a major role in budding transition and dynamics. Its influences are qualitatively comparable to the other three elastic parameters σ, H_0 and κ ones. The Gaussian term in F_2 induces forces only in membrane regions, where gradients of ϕ and non zero Gaussian curvatures overlap (e.g. at the neck region). Hence, we expect that the influence of gradients in κ_G on budding plays an increased role at small scales where transition regions and neck induced curvature are relatively large compared to the total domain size. In agreement with the results of [6, 17, 153], we additionally observe that differences in κ_G appear through a shift of the neck into the direction of the phase with the lower Gaussian rigidity (c.f. FIG 4.12 G-I). The observed shift between neck and phase boundary in the case of $\kappa_G^A = \kappa_G^B$ (c.f. FIG 4.12 H) is likely to be due to an asymmetry in the domain geometry.

4.2.3.5 Area Difference Elasticity

It has already been shown that there can be differences in the composition of two monolayers, constituting a lipid bilayer membrane [32]. This asymmetric composition can lead to differences in monolayer surface areas as well. Experiments with artificial membranes show that this area difference can have a striking influence on membrane morphology [21, 174], termed as the "bilayer-couple mechanism". However, in practical terms, the bilayer-couple mechanism seems to be less biological relevant. This is related to the global impact of this mechanism [269]. Nevertheless, an area difference between the monolayers induced by certain proteins, called "flippases", is assumed to be involved in initial steps of vesicle formation and membrane remodeling [37, 67, 199]. Here, we also investigate very briefly the impact of this mechanism on membrane budding.

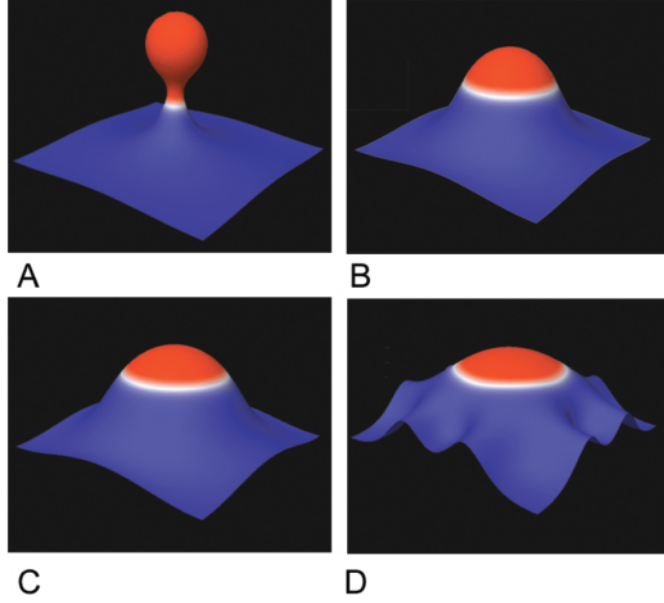


Figure 4.13: The effect of area difference elasticity ΔA_0 on membrane budding. Choosing $\Delta A_0^A = -0.1$ (A) results in a complete bud, whereas increasing ΔA_0^A flattens the domain progressively (B: $\Delta A_0^A = -0.02$, C: $\Delta A_0^A = 0.02$), resulting in strong curvatures in opposite direction (D: $\Delta A_0^A = 0.1$).

Since we consider two conserved molecule species A and B within our membrane, both species may contribute to an average relaxed global area difference ΔA_0 between the two monolayers (e.g. inserting asymmetrically into the membrane, i.e. with preference to one of the monolayers). If the preferred area difference values for the pure species are given by ΔA_0^A and ΔA_0^B , respectively, we define the linear dependence $\Delta A_0 = \frac{\Delta A_0^A + \Delta A_0^B}{2} - \frac{\Delta A_0^A - \Delta A_0^B}{2} \left(\frac{\int_{\Gamma} \phi ds}{A} \right)$, which is constant in time due to global area and mass conservation. Hence, for a membrane exclusively composed of species A (B), it holds $\Delta A_0 = \Delta A_0^A$ ($\Delta A_0 = \Delta A_0^B$). Since estimated values for the dimensionless parameter $\alpha = \frac{\bar{\kappa}}{\kappa}$ yield $\alpha \approx 1.25$ [169], in the following we choose $\bar{\kappa} = 1.25(\kappa^A + \kappa^B)/2$.

To investigate the effect of area difference elasticity on membrane budding, we choose different values $\Delta A_0^A \in [-0.1, 0.1]$, but keep $\Delta A_0^B = 0$. Corresponding results are shown in FIG 4.13. We observe that a strong negative value choosing $\Delta A_0^A = -0.1$ leads to a budding (c.f. FIG 4.13 A). Whereas increasing ΔA_0^A stepwise up to $\Delta A_0^A = 0.1$ flattens the domain (c.f. FIG 4.13 B-C) leading finally to strong curvatures in opposite direction (c.f. FIG 4.13 D). These results are in accordance with the theoretical and experimental observations that the monolayer area difference influences budding direction very sensitively [21, 174].

4.2.4 Discussion

In the present section, we have investigated the impact of different elastic parameters (line tension, bending rigidity, Gaussian rigidity, spontaneous curvature as well as monolayer area difference) on membrane budding, which is a fundamental process in biological cells [4]. We have shown numerically that each of the five parameters can be used to induce budding. Concerning the Gaussian rigidity, this is a new aspect in membrane biology. Furthermore, our results reveal that differences in elastic parameters can be used to influence relevant time scales of the budding process. Presented simulation results match recent theoretical (sharp-interface) and experimental findings in membrane research. Hence, in future work, the presented model and its computation can be used for upscaling approaches of molecular membrane models, as already pursued in Section 4.1.

4.3 Lateral Sorting and Transversal Communication in Coupled Monolayers

4.3.1 Introduction

The detailed concerted organization of molecules within a bilayer membrane is crucial for any biological function of the system. It has been shown that the length of membrane components [139], their stiffness [193], their shape and structure [161], as well as lateral phase separation [18] play a major role in membrane organization. Furthermore, experimental results highlight the strong influence of interactions between the monolayers on membrane organization. Differences in the composition of the two monolayers can induce changes in the bilayer shape as well as phase dependent transversal organization [52, 110]. However, the exact mechanisms leading to the appropriate organization remain unknown. One possibility are passive dynamical flows driven by mechanical forces, since the properties of the molecular membrane components directly influence the local mechanical properties of the membrane.

Various theoretical membrane model systems have been developed in the past to investigate membrane organization, mainly treating the membrane as one layer (c.f. Section 2.3.1 as well as Section 4.1-4.2). Studies explicitly considering a separate inner and outer monolayer are either restricted to lateral homogeneous membranes [149, 257] or deformations have not been considered [7, 247].

In this section, we present a continuous mathematical model of a fluid bilayer membrane, consisting of two explicitly given coupled monolayers. Each monolayer consists of two different lateral phase separating components. The model accounts for differences in the length, stiffness and shape of the molecules (described by macroscopic elastic moduli) as well as a boundary energy between separating phases. We numerically study how the interplay of membrane shape, thickness, lateral, and transversal organization is affected by the exact composition of the membrane as well as the exact dependence on the mechanical properties of the different membrane components found in the monolayers. The results are discussed in the context of recent experimental results and related biological processes. The presented section is closely related to [167].

4.3.2 Mathematical Model

Here, we address a continuous approach to model and simulate the deformations and in-plane organization of lipids and proteins of a lipid bilayer membrane. In contrast to our basic model (c.f. Section 2.4) each monolayer is explicitly considered treating the bilayer as two coupled individual surfaces. Compared to previous intermonolayer coupling studies, where a phenomenological coupling constant has been used [101, 247], all observed sorting effects result directly from the following two basic assumptions: I.) the thickness of the bilayer depends on the length of the opposed molecules; II.) different molecule species can vary in their shape, length or stiffness.

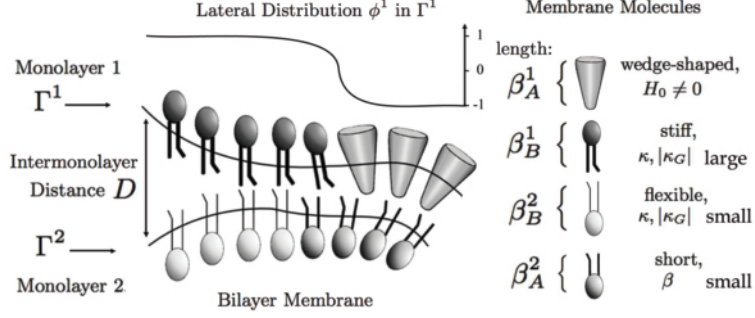


Figure 4.14: Continuous bilayer model: Each monolayer is represented by a surface Γ^i and its lateral composition by an order parameter ϕ^i , $i \in \{1, 2\}$. Molecule properties are outlined on the right hand side. Intermonolayer distance is measured by D , not necessarily coinciding with the optimal distance $a = (\beta_B^1 + \beta_B^2)/2$, as shown on the left hand side.

Furthermore, the model can be explicitly parameterized by the relevant parameters of molecular length and elastic moduli.

For $i \in \{1, 2\}$, each monolayer patch is represented by a two-dimensional (2D) surface Γ^i curved in 3D space, depicted by a parametric representation $\vec{X}^i(u_1, u_2) : U \rightarrow \Gamma^i \subset \mathbb{R}^3$ with $U = [0, 1] \times [0, 1]$. The concentration of two components A and B in Γ^i is described by the order parameter $\phi^i : U \rightarrow [-1, 1]$. If $\phi^i = -1$ the membrane Γ^i is locally composed of 100% species B, if $\phi^i = 1$ locally only species A is present. We assume that hydrophobic interactions between the two monolayers mainly take place between opposed molecules, i.e. molecules only interact with the nearest molecules on the other monolayer. The distance between the layers, i.e. between interacting molecules, is given locally by the distance function $D^i : \Gamma^i \rightarrow \Gamma^j$, where D^i maps $\vec{X}^i \in \Gamma^i$ to $\vec{X}^j \in \Gamma^j$ so that \vec{X}^j has minimal distance to \vec{X}^i . Hence, for each molecule in layer i the function D^i measures the distance to the nearest opposed molecule in the other layer. To guarantee the uniqueness of the distance function $D^i(\vec{X}^i)$ we define it in the following way: $D^i(\vec{X}^i) := \sum_{\vec{Y} \in M^i} \frac{\vec{Y}}{|\vec{M}^i|}$ and $M^i := \{Y \in \Gamma^j : \forall \vec{Z} \in \Gamma^j \|\vec{X}^i - \vec{Y}\| \leq \|\vec{X}^i - \vec{Z}\|\}$.

Adopting the basic approach (c.f. Section 2.4), our model is based on the minimization of the bilayer free energy $F = F^1 + F^2$, where for each monolayer Γ^i ($i = 1, 2$) the free energy is given by $F^i = F_1^i + F_2^i + F_3^i + F_5^i$,

$$F_1^i = \int_{\Gamma^i} \frac{\kappa^i(\phi^i)}{2} (H^i - H_0^i(\phi^i))^2 ds^i$$

$$F_2^i = \int_{\Gamma^i} \kappa_G^i(\phi^i) K^i ds^i,$$

$$F_3^i = \sigma^i \int_{\Gamma^i} \left(\frac{(\xi^i)^2}{2} (\nabla^{\Gamma^i} \phi^i)^2 + f^i(\phi^i) \right) ds^i,$$

$$F_5^i = \frac{\alpha}{2} \int_{\Gamma^i} \left(D^i(\bar{X}^i) - a(\phi^i, \phi^j) \right)^2 ds^i.$$

Here, superscripts denote the monolayer and subscripts refer to different types of energies/interactions. The area difference elasticity term F_4 (c.f. Section 2.4.1) has been neglected in this model, since area differences between the two monolayers can be introduced explicitly.

$F_1^i + F_2^i$ is the bending elastic energy of the membrane (c.f. Section 2.4), where ds^i is the surface area element, H and K are the mean curvature and the Gaussian curvature, respectively, H_0^i is the spontaneous curvature and κ^i and κ_G^i are the bending rigidity and the Gaussian rigidity, respectively. In the case of homogeneous monolayers, the elastic moduli κ^i , κ_G^i and H_0 are taken as constant, whereas K^i and H^i depend on the local geometry of the monolayers. In the present model, both monolayers consist of different molecule species. Since different types of membrane molecules can display different mechanical properties, elastic moduli are again assumed to depend on the local composition of the monolayers, described by ϕ^i . We assume that elastic moduli are linear functions of ϕ^i , i.e. $\kappa^i(\phi^i) = \frac{\kappa_A^i + \kappa_B^i}{2} + \frac{\kappa_A^i - \kappa_B^i}{2} \phi^i$ (although the DPD studies in Section 4.1 suggest a nonlinear relationship), where κ_A^i and κ_B^i are the bending rigidities of the molecular species A and B in Γ^i . H_0^i and κ_G^i are defined analogously.

F_3^i is the Cahn-Hilliard energy (c.f. Section 2.4) describing lateral phase separation of the two species A and B [38]. This energy contribution is included, since lateral demixing seems to be a fundamental process underlying spatial organization in biological membranes [18, 192]. In this energy part, ξ^i is a phase transition length, $\sigma_{si}^i = \sigma^i \cdot \xi^i$ represents the sharp line tension, ∇^{Γ^i} the surface gradient, and $f^i = \frac{9}{32} ((\phi^i)^2 - 1)^2$ a double well potential (c.f. Appendix B), causing the separation into two phases.

Finally, the free energy F_5^i elastically penalizes deviations of the intermonolayer distance from an "optimal bilayer thickness", described by the function $a = a(\phi^i, \phi^j)$ and weighted by α . The optimal thickness of a bilayer is mainly determined by the length of opposite molecules [143, 204]. The physical origin of F_5^i is related to the "hydrophobic effect", i.e. an interaction force causing the clustering of hydrophobic units in water [44]. In the case of lipid bilayers, it is based on strong attractions between hydrophilic parts of membrane molecules and water, partly stabilized by hydrophobic forces [213]. Furthermore, we assume that different molecule lengths and deviations from this optimal thickness primarily change the average distance between opposed molecule heads (leading e.g. to entropic changes) [117, 214, 236]. Additionally, the lengths shall not significantly influence the molecules equilibrium area per molecule-head presented to the water, since head groups try to keep a closed surface. Hence,

bilayer thickness fluctuations do not contradict the assumed lateral area incompressibility of the two monolayer leaflets. (Also incompressibility is considered separately for each monolayer - in contrast to previous studies where the bilayer mid-plane is assumed to be incompressible [169, 219].) It has been already shown that the thickness of a lipid bilayer varies linearly with the length of membrane molecules [143]. Hence, we assume that the bilayer optimal thickness function depends linearly on the average length of locally opposed molecules: if β_A^i and β_B^i represent the lengths of the molecules A and B in Γ^i , the local average molecule length in Γ^i is given by $\beta^i(\phi^i) := \frac{\beta_A^i + \beta_B^i}{2} + \frac{\beta_A^i - \beta_B^i}{2} \phi^i$. Since the bilayer optimal thickness function measures the distance between the mid-planes of the two monolayer leaflets (c.f. FIG 4.14) it is given by the average of the opposite molecule lengths, i.e. $a := (\beta^i(\phi^i) + \beta^j(\phi^j))/2$.

Following the dynamical approach presented in Section 2.4.2, dynamics of the deformation \vec{X}^i in $U \times [0, T)$ are given by the following gradient flow under the constraint of a strong local area incompressibility of each monolayer leaflet (considered separately):

$$\partial_t[\vec{X}^i] = -L_{X^i} \frac{\delta}{\delta \vec{X}^i} \left[F + \int_{\Gamma^i} \gamma^i ds^i \right], \quad (4.6)$$

$$\partial_t[\sqrt{g^i}] = 0, \quad (4.7)$$

for $i = 1, 2$. Hence, an evolution of each monolayer takes place in order to minimize the free energy, which depends in turn on local curvatures, compositions and the distance to the other monolayer. Here, L_{X^i} is a kinetic coefficient (scaling inversely with the viscosity of the surrounding medium), $\frac{\delta}{\delta \vec{X}^i}[F^i] = \frac{\delta}{\delta \vec{X}^i}[F_1^i + F_2^i + F_3^i + F_5^i]$ denotes the variation of F^i with respect to \vec{X}^i , γ^i is a local Lagrange multiplier and g is the determinant of the first metric tensor [61, 93]. Since the surface measure of a curved surface is defined by $ds = \sqrt{g} d^2u$, equation (4.7) represents the local surface incompressibility (c.f. Section 2.4.2).

For detailed calculations of the variations of F_1^i , F_2^i and F_3^i constituting equation (4.6), we refer to Section 2.4.3 and to the Appendix D. In the following, we calculate the variations of F_5^i with respect to \vec{X}^i . Here, $\delta^{\perp i}[\cdot]$ ($\delta^{k i}[\cdot]$) constitutes the normal (k -tangential) variation with respect to \vec{X}^i , and $\frac{\delta^{\perp}}{\delta \vec{X}^i}[\cdot]$ ($\frac{\delta^k}{\delta \vec{X}^i}[\cdot]$) its pointwise strong formulation. For further notational details and definitions, we refer to the Appendix.

Proposition IV.1. *Rewriting $D^i(\vec{X}^i) = \|\vec{X}^i - \vec{X}_{min}^j\|$, it follows:*

$$\frac{\delta^{\perp}}{\delta \vec{X}^i}[D^i(\vec{X}^i)] = \frac{\langle \vec{n}^i, \vec{X}^i - \vec{X}_{min}^j \rangle}{D^i(\vec{X}^i)}. \quad (4.8)$$

Proof: Using the chainrule, it follows:

$$\begin{aligned}\delta^{\perp i}[D^i(\vec{X}^i)] &= \frac{1}{2}\langle \vec{X}^i - \vec{X}_{min}^j, \vec{X}^i - \vec{X}_{min}^j \rangle^{-1/2} \delta^{\perp i}[\langle \vec{X}^i - \vec{X}_{min}^j, \vec{X}^i - \vec{X}_{min}^j \rangle] \\ &= \frac{1}{\|\vec{X}^i - \vec{X}_{min}^j\|} \psi \langle \vec{n}^i, \vec{X}^i - \vec{X}_{min}^j \rangle,\end{aligned}$$

leading to the claim. \square

Since for any \vec{X}^i in Γ^i , \vec{X}^i may appear in F^j as well, we define: $\tilde{\alpha} = \alpha$, if there exists an $\vec{Y}_{X^i}^j \in \Gamma^j$ with $D^j(\vec{Y}_{X^i}^j) = \|\vec{Y}_{X^i}^j - \vec{X}^i\|$, $\tilde{\alpha} = 0$ else.

Lemma IV.2.

$$\begin{aligned}\frac{\delta^{\perp i}[F_5^i]}{\delta \vec{X}^i} &= \alpha(D^i(\vec{X}^i) - a(\phi^i, \phi^j))\langle \vec{X}^i - \vec{X}_{min}^j, \vec{n}^i \rangle D^i(\vec{X}^i)^{-1} \\ &\quad + \frac{\alpha}{2}(D^i(\vec{X}^i) - a(\phi^i, \phi^j))^2 H^i \\ &\quad - \tilde{\alpha}(D^j(\vec{Y}_{X^i}^j) - a(\phi^j, \phi^i))\langle \vec{Y}_{X^i}^j - \vec{X}^i, \vec{n}^i \rangle D^j(\vec{Y}_{X^i}^j)^{-1}.\end{aligned}$$

Proof: Using the chain rule and the identity $\delta^{\perp i}[\sqrt{g^i}] = \psi H^i \sqrt{g^i}$ [267], we obtain

$$\begin{aligned}\delta^{\perp i}[F_5^i] &= \alpha \int_{\Gamma^i} (D^i(\vec{X}^i) - a(\phi^i, \phi^j)) \delta^{\perp i}[(D^i(\vec{X}^i) - a(\phi^i, \phi^j))] \sqrt{g^i} d^2 u \\ &\quad + \frac{\alpha}{2} \int_{\Gamma^i} (D^i(\vec{X}^i) - a(\phi^i, \phi^j))^2 H^i \psi \sqrt{g^i} d^2 u. \\ &\quad + \tilde{\alpha} \int_{\Gamma^j} (D^j(\vec{Y}_{X^i}^j) - a(\phi^j, \phi^i)) \delta^{\perp i}[(D^j(\vec{Y}_{X^i}^j) - a(\phi^j, \phi^i))] \sqrt{g^j} d^2 u.\end{aligned}$$

From Proposition IV.1, it follows:

$$\begin{aligned}\delta^{\perp i}[F_5^i] &= \alpha \int_{\Gamma^i} (D^i(\vec{X}^i) - a(\phi^i, \phi^j)) \langle \vec{X}^i - \vec{X}_{min}^j, \vec{n}^i \rangle D^i(\vec{X}^i)^{-1} \sqrt{g^i} d^2 u \\ &\quad + \frac{\alpha}{2} \int_{\Gamma^i} (D^i(\vec{X}^i) - a(\phi^i, \phi^j))^2 H^i \psi \sqrt{g^i} d^2 u, \\ &\quad - \tilde{\alpha} \int_{\Gamma^j} (D^j(\vec{Y}_{X^i}^j) - a(\phi^j, \phi^i)) \langle \vec{Y}_{X^i}^j - \vec{X}^i, \vec{n}^i \rangle D^j(\vec{Y}_{X^i}^j)^{-1} \sqrt{g^j} d^2 u,\end{aligned}$$

leading to the claim. \square

Proposition IV.3.

$$\frac{\delta^k}{\vec{X}^i}[D^i(\vec{X}^i)] = \frac{\langle \partial_k \vec{X}, \vec{X}^i - \vec{X}_{min}^j \rangle}{D^i(\vec{X}^i)}. \quad (4.9)$$

Proof: The proof goes along the lines of the proof of Proposition IV.1. \square

Lemma IV.4.

$$\begin{aligned} \frac{\delta^k [F_5^i]}{\delta \vec{X}^i} = & \alpha (D^i(\vec{X}^i) - a(\phi^i, \phi^j)) \left(\frac{1}{2} \sum_u \langle \vec{X}^i - \vec{X}_{min}^j, \partial_k \vec{X}^i \rangle (D^i(\vec{X}^i) g_{uk}^{(i)})^{-1} \right) \\ & - \partial^k \left[\frac{\alpha}{2} (D^i(\vec{X}^i) - a(\phi^i, \phi^j))^2 \right] \\ & - \tilde{\alpha} (D^j(\vec{Y}_{X^i}^j) - a(\phi^j, \phi^i)) \left(\frac{1}{2} \sum_u \langle \vec{Y}_{X^i}^j - \vec{X}^i, \partial_k \vec{X}^i \rangle (D^j(\vec{Y}_{X^i}^j) g_{uk}^{(i)})^{-1} \right). \end{aligned}$$

Using again the chain rule and the fact that for functions $\eta \in C^1(U, \mathbb{R})$ it holds that $\int \eta \delta^t [\sqrt{g}] d^2u = -\sum_{k,u} \int \partial^u [\eta] g_{uk} \psi^k \sqrt{g} d^2u$ (c.f. Proposition D.6 in Appendix D), it follows:

$$\begin{aligned} \delta^{ti} [F_5^i] = & \alpha \int_{\Gamma^i} (D^i(\vec{X}^i) - a(\phi^i, \phi^j)) \delta^{ti} [(D^i(\vec{X}^i) - a(\phi^i, \phi^j))] \sqrt{g^i} d^2u \\ & - \sum_{k,u} \frac{\alpha}{2} \int_{\Gamma^i} \partial^u [(D^i(\vec{X}^i) - a(\phi^i, \phi^j))^2] \sqrt{g^i} g_{uk}^{(i)} \psi^k d^2u \\ & + \tilde{\alpha} \int_{\Gamma^j} (D^j(\vec{Y}_{X^i}^j) - a(\phi^j, \phi^i)) \delta^{ti} [(D^j(\vec{Y}_{X^i}^j) - a(\phi^j, \phi^i))] \sqrt{g^j} d^2u. \end{aligned}$$

Using Proposition IV.3, the relation $\delta^t = \sum_k \delta^k$ as well as the identity

$$\langle \vec{Z}, \partial_k \vec{X}^i \rangle (D^i(\vec{X}^i))^{-1} = \frac{1}{2} \sum_u \frac{g_{uk}^{(i)}}{g_{uk}^{(i)}} \langle \vec{Z}, \partial_k \vec{X}^i \rangle (D^i(\vec{X}^i))^{-1}$$

for any \vec{Z} , yields

$$\begin{aligned} \delta^{ti} [F_5^i] = & \frac{\alpha}{2} \sum_{u,k} \int_{\Gamma^i} (D^i(\vec{X}^i) - a(\phi^i, \phi^j)) \frac{g_{uk}^{(i)}}{g_{uk}^{(i)}} \langle \vec{X}^i - \vec{X}_{min}^j, \partial_k \vec{X}^i \rangle (D^i(\vec{X}^i))^{-1} \sqrt{g^i} d^2u \\ & - \sum_{k,u} \frac{\alpha}{2} \int_{\Gamma^i} \partial^u [(D^i(\vec{X}^i) - a(\phi^i, \phi^j))^2] \sqrt{g^i} g_{uk}^{(i)} \psi^k d^2u \\ & - \frac{\tilde{\alpha}}{2} \sum_{u,k} \int_{\Gamma^j} (D^j(\vec{Y}_{X^i}^j) - a(\phi^j, \phi^i)) \frac{g_{uk}^{(i)}}{g_{uk}^{(i)}} \langle \vec{Y}_{X^i}^j - \vec{X}^i, \partial_k \vec{X}^i \rangle (D^j(\vec{Y}_{X^i}^j))^{-1} \sqrt{g^j} d^2u, \end{aligned}$$

leading to the claim. \square

Following the approach presented in Section 2.4.2, we have the following dynamical equation for ϕ in $U \times [0, T)$ considering both monolayers separately

$$d_t[\phi^i] = L_{\phi^i} \Delta^{\Gamma^i} \left[\frac{\delta}{\delta \phi^i} [F] \right] \quad (4.10)$$

for $i = 1, 2$. Relative straight forward calculations yield

$$\begin{aligned} d_t[\phi^i] = & L_{\phi^i} \Delta^{\Gamma^i} \left[\frac{\delta}{\delta \phi^i} [F_1^i + F_2^i + F_3^i] \right. \\ & - \alpha (D^i(\vec{X}^i) - a(\phi^i, \phi^j)) \partial_{\phi^i} [a(\phi^i, \phi^j)] \\ & \left. - \tilde{\alpha} (D^j(\vec{Y}_{X^i}^j) - a(\phi^j, \phi^i)) \partial_{\phi^i} [a(\phi^i, \phi^i)] \right] \end{aligned}$$

in $U \times [0, T)$. For a detailed calculation of $\frac{\delta}{\delta \phi^i} [F_1^i + F_2^i + F_3^i]$ we refer to Section 2.4.3.

4.3.3 Nondimensionalization

Let us now derive a nondimensionalized model of the two coupled monolayers, constituting a bilayer membrane. Since in Section 2.5 we have already nondimensionalized $F_1^i - F_3^i$, we restrict us here to F_2^i , $i \in \{1, 2\}$.

Hence, we choose

$$\vec{X} = \epsilon_x \vec{X}_c \quad \text{with} \quad [\vec{X}] = [\epsilon_x] = m,$$

which implies $ds = \epsilon_x^2 ds_c$, and $a = \epsilon_x a_c$. Choosing

$$\alpha = \frac{\epsilon_\kappa}{\epsilon_x^4} \alpha_c \quad \text{with} \quad [\alpha] = \frac{k_B T}{m^4}$$

yields

$$\frac{\alpha}{2} \int_{\Gamma^i} \left(D^i(\vec{X}^i) - a(\phi^i, \phi^j) \right)^2 ds^i = \epsilon_\kappa \frac{\alpha_c}{2} \int_{\Gamma^i} \left(D_c^i(\vec{X}_c^i) - a_c(\phi_c^i, \phi_c^j) \right)^2 ds_c^i.$$

Again, a consistency check shows $[F_2^i] = [\epsilon_\kappa] = k_B T$ has units of energy.

4.3.4 Finite Element Approximation and Parameter Setup

Using the outlined macroscopic modeling approach, we investigate the effect of molecule length variations and curvature modulated sorting. Hence, we numerically

approximate equations (4.6), (4.7) and (4.10) to study systematically deformations and lateral dynamics of two coupled monolayers constituting a lipid bilayer. We use a mixed finite element approach; for corresponding details, we refer to Chapter III.

In the following, the surface of each monolayer is discretized using a quadrangular grid with $M^i = 4096$ grid points, i.e. in total 8192 grid points. To control the complexity, we do not apply any lateral tension [206] and impose Dirichlet-zero boundary conditions for X_1^i and X_2^i as well as Neumann zero boundary conditions else. (Anyway, it appears that using periodic or Neumann zero boundary conditions for all variables leads to the same qualitative and quantitative results.) For time discretization we use an adaptive semi-implicit Euler scheme. If not otherwise stated, we use in both monolayers stochastic initial conditions, representing the disordered and homogeneous mixture of molecules at high temperatures. Furthermore, we use the following set of parameters: $\kappa^i(\phi^i) \equiv 20 k_B T$, $\kappa_G^i(\phi^i) \equiv -10 k_B T$, $H_0^i(\phi^i) \equiv 0 \text{ nm}^{-1}$, $\sigma^i = 1400 k_B T \mu\text{m}^{-2}$, $\xi = 0.8 \text{ nm}$, $\alpha = 9.6 \cdot 10^7 k_B T \mu\text{m}^{-4}$, $L_{X^i} = 6.25 \cdot 10^{-11} \mu\text{m}^4 \text{s}^{-1} (k_B T)^{-1}$, $L_{\phi^i} = 3.12 \cdot 10^{-5} \mu\text{m}^4 \text{s}^{-1} (k_B T)^{-1}$, $a \equiv 2.5 \text{ nm}$, for $i \in \{1, 2\}$. This parameter set corresponds to the molecular diffusion coefficient $D = L_{\phi^i} \sigma^i = 1.1 \cdot 10^{-10} \text{ cm}^2 \text{s}^{-1}$ and the sharp line tension $\sigma_{si}^i = \sigma^i \xi = 1.15 k_B T \mu\text{m}^{-1}$ (c.f. Appendix B). (Odd numbers result from the conversion of abstract nondimensionalized model parameters into physical values.) Most of the parameters have been already characterized by experimental means and these are in the same magnitude range as the values used here [3, 95, 216, 230].

4.3.5 Numerical Results

Membrane Organization Induced by Varying Molecular Lengths

Motivated by many experimental studies indicating the importance of lipid and membrane protein interactions due to varying molecule sizes [139], we investigate the impact of the molecule size on the lateral membrane organization, i.e. molecular sorting. For this purpose, we study two coupled monolayers differing from each other with respect to their composition of molecules with different lengths (c.f. FIG 4.15). For all corresponding simulations we use constant elastic moduli. Furthermore, we set the following initial conditions: A-F: $\langle \phi_0^1 \rangle = \langle \phi_0^2 \rangle = -0.5$, A: $\Gamma_0^1 = 2.5 + 0.5u_x + 0.125u_x^2 \text{ nm}$ and $\Gamma_0^2 = -0.5u_x - 0.125u_x^2 \text{ nm}$, C-F: $\Gamma_0^1 = 2.0 + 0.15 \sin(\pi u_x) \sin(\pi u_y) \text{ nm}$ and $\Gamma_0^2 = 0.15 \sin(\pi u_x) \sin(\pi u_y) \text{ nm}$.

In FIG 4.15 A we artificially stretch two monolayers on one side apart by an appropriate choice of boundary conditions in the normal direction mimicking big membrane spanning proteins. In Γ^1 we consider molecules with two different lengths $\beta_A^1 = 3 \text{ nm}$ and $\beta_B^1 = 2 \text{ nm}$, and in Γ^2 two species with the same lengths $\beta_A^2 = \beta_B^2 = 2.5 \text{ nm}$. During the simulation, we observe a distance relaxation between the monolayers combined with a distance dependent lateral sorting in Γ^1 and a distance independent sorting in Γ^2 . In Γ^1 longer molecules ϕ_A separate with a strong preference for the

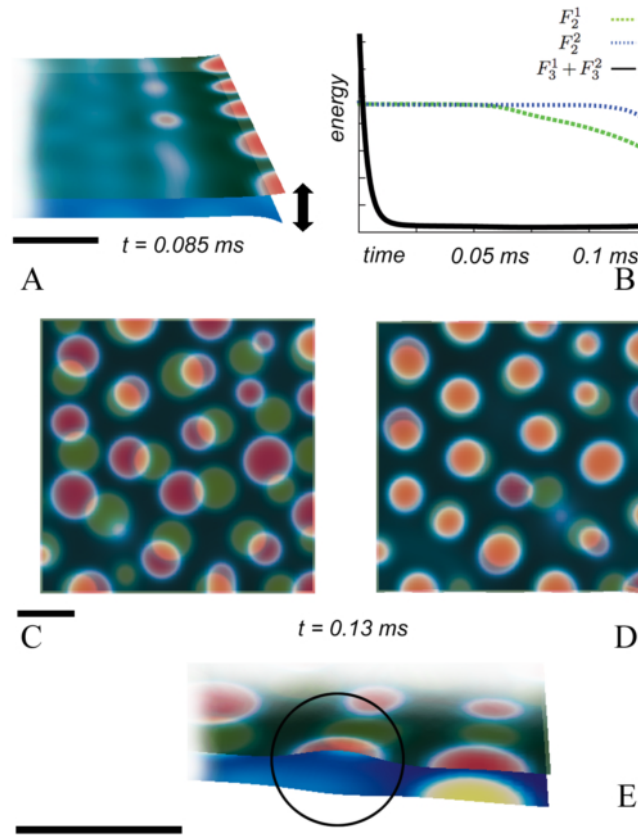


Figure 4.15: Influence of molecule lengths on intermonolayer coupling. Red and green correspond to high local concentrations of species A and B in the upper monolayer; yellow and blue correspond to local high concentrations of species A and B in the lower monolayer, respectively. A: Stretching of the two monolayers in the normal direction leads to a sorting of long molecules to the stretched area in Γ^1 , whereas the molecules in Γ^2 have the same length. B: Corresponding decay of different parts of the free energy F . D: Long molecules are sorted opposite to short molecules, whereas all molecules in (C) have the same length. E: Detailed view of D; non synchronized domains (black circle) induce curvatures in both layers. (Scale bars: 10 nm).

region close to the boundary where the normal stretch is applied. Whereas in Γ^2 no special preference can be observed - as expected. Furthermore, the Cahn-Hilliard energy F_3^1 decays faster than F_3^2 (c.f. FIG 4.15 B), i.e. different molecular lengths do not only lead to an accumulation at specific places but also enhances the speed of the sorting process (c.f. FIG 4.15 B).

So far we have considered one layer with molecules of the same length and one layer with molecules of different length. Now let us consider the following two different scenarios: in C $\beta_A^1 = \beta_B^1 = \beta_A^2 = \beta_B^2 = 2.5$ nm and in D $\beta_A^1 = \beta_B^1 = 4$ nm and $\beta_A^2 = \beta_B^2 = 1$ nm. In both cases no artificial stretching is applied. We observe that different molecule lengths induce a spatial phase synchronization between the monolayers: long molecules of one layer are sorted to short molecules of the other layer causing (in the given ratio of components) a bilayer of homogeneous thickness.

Membrane Organization Induced by Curvature Modulated Intermonolayer Coupling

Inspired by the richness of curvature generating mechanisms [223] and recent experimental evidences for curvature modulated lateral sorting [193, 262], we further investigate the interplay of curvature and lateral/transversal sorting between two coupled monolayers. Corresponding results are presented in FIG 4.16. Previous theoretical studies typically have used a phenomenological coupling constant to describe curvature modulated sorting [5, 45, 120, 237, 260]. Whereas the effects observed here result directly from first physical principles - namely from the assumption that different molecules can vary in their shape and stiffness.

We demonstrate that deformations in one monolayer induced by different mechanisms (identified by experiments) influence the chemical distribution in both layers, if the molecules vary in stiffness or shape. The latter is modeled via differences in macroscopic elastic moduli, e.g. the bending rigidity κ , the Gaussian rigidity κ_G and the local spontaneous curvature H_0 . For all corresponding simulations we use constant molecule lengths. FIG 4.16 shows the interaction of two components A and B in both layers with different bending moduli leading to molecule sorting. In the following, we will study the detailed interplay between lateral sorting and curvature generating mechanisms. Adopting the most basic curvature generating mechanisms in biological membranes [161], local curvatures are induced via different mechanisms.

In FIG 4.16 B contrary to A we apply a constant circular upward force in the middle of Γ^1 - corresponding e.g. to tubules applying a force via motor proteins pushing the membrane [210]. In FIG 4.16 C and D we simulate stable clusters of stiff shaping membrane proteins in Γ^1 choosing $\phi_0^1 = \sin(5\pi u_1)$, $L_\phi^1 = 0$ and $\kappa^1(1) = 40 k_B T$ with positive curvature $H_0^1(1) = 0.2 \text{ nm}^{-1}$ in C as well as negative curvature $H_0^1(1) = -0.2 \text{ nm}^{-1}$ in D. A corresponding example in biological membranes is e.g. the scaffolding mechanism: a huge rigid protein or a protein domain

that has an intrinsic curvature bends the membrane beneath it, but lateral dynamics of lipids are possible in at least one monolayer [269]. In FIG 4.16 E, as opposed to F, the global area A_2 of Γ^1 differs from A_1 , which has been early assumed as a curvature generation mechanism [221] and is proved to be a frequent mechanism in biological membranes - a prominent example is the amphipatic helix insertion [74].

In all simulations shown in FIG 4.16, lateral sorting is induced by choosing differences in stiffness or shape of different membrane components, expressed by differences among the species A and B in one of the macroscopic elastic moduli: the bending rigidity κ , the spontaneous curvature H_0 or the Gaussian rigidity κ_G . In A-B we have set $\kappa^i(1) = 19.9 k_B T$ but $\kappa^i(-1) = 20 k_B T$; In C-D $H_0^2(1) = -5 \cdot 10^{-3} \text{ nm}^{-1}$ but $H_0^2(-1) = 5 \cdot 10^{-3} \text{ nm}^{-1}$ and in E-F $\kappa_G^i(1) = -8.88 k_B T$ but $\kappa_G^i(-1) = -10 k_B T$; $i \in \{1, 2\}$. For the simulations shown in FIGure 4.16 we use the following initial conditions: A-B: $\langle \phi_0^1 \rangle = -0.7$; $\langle \phi_0^2 \rangle = 0$, $\Gamma_0^1 = 3.5 - 5.0 \sin(\pi u_x) \text{ nm}$ and $\Gamma_0^2 = -5.0 \sin(\pi u_x) \text{ nm}$; C-D: $\langle \phi_0^1 \rangle = \sin(5\pi u_x)$; $\langle \phi_0^2 \rangle = 0$, $\Gamma_0^1 = 1.0 - 2.5 \sin(\pi u_x) \text{ nm}$ and $\Gamma_0^2 = -2.5 \sin(\pi u_x) \text{ nm}$; E-F: $\langle \phi_0^1 \rangle = -0.7$; $\langle \phi_0^2 \rangle = 0$, $\Gamma_0^1 = 3.5 + 2.5 \sin(\pi u_x) \sin(\pi u_y) \text{ nm}$ and $\Gamma_0^2 = 2.5 \sin(\pi u_x) \sin(\pi u_y) \text{ nm}$.

The exact choice of the inhomogeneous elastic moduli does not depend on the curvature generating mechanism. For clarity, we have restricted ourselves to selected cases of interplay between curvature generating and lateral sorting mechanisms. Indeed, in real membranes there are many more possible interplays.

4.3.6 Discussion

Above we have addressed the following main aspects of membrane organization: sorting due to different molecule lengths, phase synchronization across monolayers as well as the interplay between curvature generation and lateral sorting mechanisms. The physical interaction and the hereby possible mutual activation or deactivation of different membrane molecules plays a key role in various cellular processes: integral membrane proteins are often activated by special lipid molecules surrounding them [139]. Furthermore, lateral as well as transversal interactions between different membrane proteins play a key role in various biological processes, such as signaling, photosynthesis and endocytosis. The mechanisms presented here could constitute basal mechanisms for these processes, i.e. passive flows of molecules with differences in length, shape and stiffness lead to a multitude of different lateral and transversal organized membrane shapes.

Membrane Organization Induced by Varying Molecular Lengths

It has been assumed that the thickness of the membrane or rather the hydrophobic mismatch of different components influences membrane molecule interactions [127]. To investigate the effect of molecule length on lateral sorting, we have stretched the

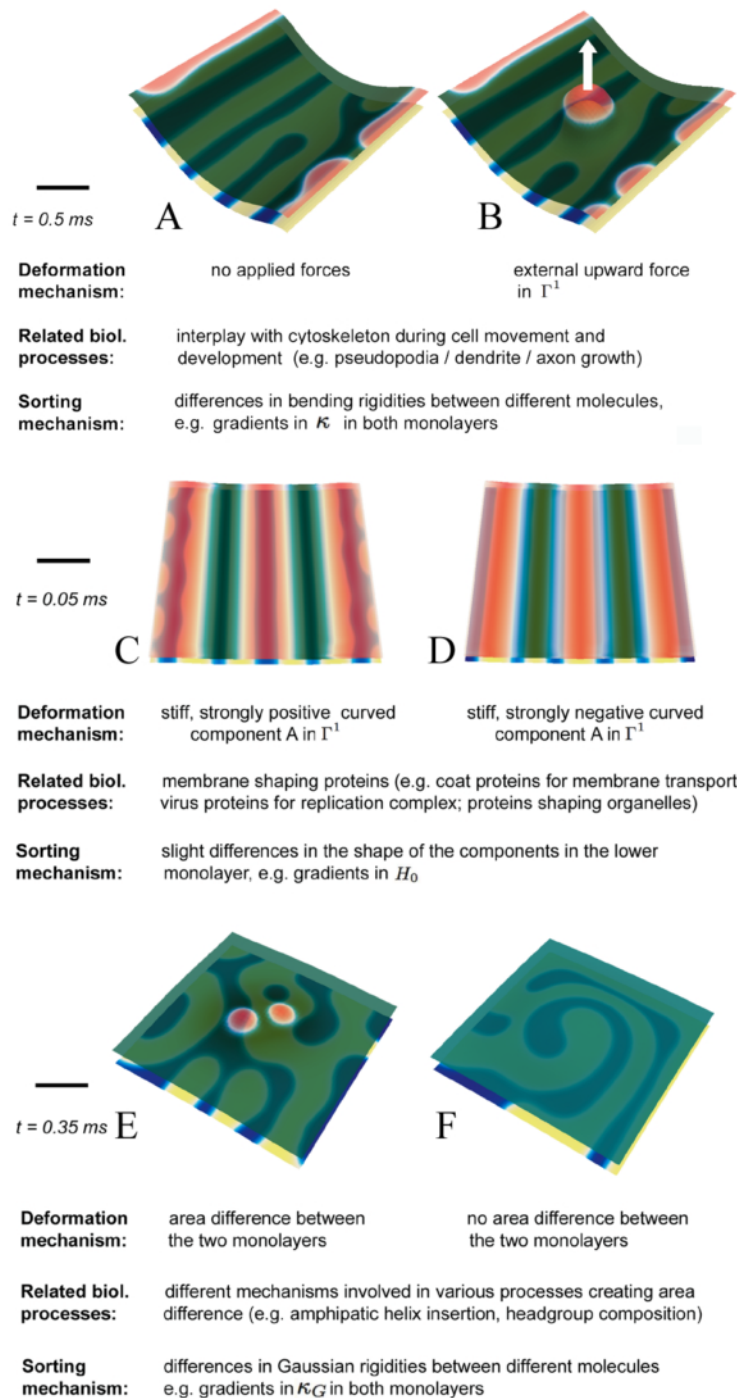


Figure 4.16: Curvature mediated intermonolayer coupling. Red and green correspond to high local concentrations of species A and B in the upper monolayer; yellow and blue correspond to high local concentrations of species A and B in the lower monolayer, respectively. Curvature mediated phase separation in each comparative simulation is driven by gradients in one elastic modulus. Local curvatures have been generated by applying an upward force to Γ^1 in B contrary to A, by choosing contrary spontaneous curvatures $H_0^1(1)$ in C and D, and by introducing a nontrivial global area difference in E contrary to F. (Scale bars: 10 nm).

distance between the two monolayers of the bilayer membrane at one edge, corresponding *in vivo* e.g. to the effects mediated by membrane spanning proteins [77]. We have observed that this thickness mismatch can induce phase separation and sorts molecules according to their length: long molecules aggregate very early in time close to the stretched region (c.f. FIG 4.15 A-B). These observations of an equally sized molecule aggregation (in order to minimize the hydrophobic mismatch) are in well accordance with the assumptions of Killian [127], molecular dynamical studies on small scales [20, 62, 63, 173] as well as experimental results [118]. We would like to mention that the effect of molecule tilt is not considered within our model but is an interesting aspect which should be covered in future studies.

In accordance with recent molecular dynamical results [173], the simulations have revealed that the length of membrane molecules can be used to induce a synchronization of phases across the bilayer membrane (c.f. FIG 4.15 C-E). This synchronization is the result of a combination of two distinct processes: on the one hand the monolayer bending rigidity prevents the layers from small scale spatial curvature fluctuations. These fluctuations become more obvious looking at regions where the synchronization does not take place (FIG 4.15 E black circle) and induce curvatures in both layers. On the other hand the molecule dynamics drive components in regions where they "fit the bilayer thickness". The same mechanism but on the scale of single molecules has been proposed by [1], investigating interdigitated phases of phospholipids and alcohols.

Recent studies have proposed different mechanisms for hydrophobic mismatch dependent sorting and interleaflet coupling [9, 51, 90, 139]. These studies have been mainly focused on energetic and entropic contributions of local compression or stretching of hydrophobic lipid tails. The mechanism presented in this study could explain how cells achieve lateral and transversal component sorting where molecules do not exhibit "flexible" parts, such as membrane proteins. *In vivo*, the observed sorting could constitute mechanisms in cells to assemble membrane proteins with certain chemical or mechanical properties close to each other or to other membrane spanning or compressing protein complexes, found in various cell processes such as signaling.

Membrane Organization Induced by Curvature Modulated Intermonolayer Coupling

So far we have considered the influence of different molecule lengths on lateral sorting. Let us now focus on the interplay between lateral sorting and curvature generating mechanisms in coupled monolayers. Cellular membranes are strikingly dynamic structures changing their shape in various processes such as movement, division, during neuronal development, and vesicle traffic. Some of the main mechanisms hereby are deformations due to external forces such as the actin cytoskeleton, scaffolding by peripheral membrane proteins and area differences between the two monolayers, e.g. induced by asymmetric lipid distributions [161, 269]. Although, the shaping mecha-

nisms themselves are well characterized, the mechanisms for a concerted organization of different components in different monolayers during the deformation process is poorly understood.

In this study, for the first time (up to our knowledge) the interplay of different membrane curvature generating mechanisms with different lateral sorting mechanisms in both monolayers is investigated (c.f. FIG 4.16). Motivated by experimental data [193, 262], our results clearly show that differences among molecular species in each of the three macroscopic mechanical moduli, the bending rigidity κ , the Gaussian rigidity κ_G (both reflecting the molecule stiffness) and the spontaneous curvature H_0 (reflecting the molecule shape), are sufficient for curvature dependent lateral sorting. These results highlight the multitude and complexity of different shapes and lateral patterns that can occur in biological membranes - simply as a result of passive flows of molecules which differ in their first-order mechanical properties.

In vivo, curvature mediated intermonolayer coupling could be an important selection mechanism for the cell: while certain components produce local curvatures (for example shaping proteins or the cytoskeleton) other components can be included in these regions simply due to their mechanical properties by the sorting mechanisms outlined above. This could explain how different structural and catalytic components are getting locally concentrated, e.g. in virus induced deformations [249].

4.4 On the Coupling of Tissue Mechanics with Morphogen Expression: A New Model for Early Pattern Formation in *Hydra* Polyps

4.4.1 Introduction

During the development of biological tissues, a variety of different signaling molecules are responsible and indispensable for pattern formation and shape generation [102] (c.f. Section 2.1.2). Since a seminal paper of Alan Turing [241] a variety of patterns appearing in biological tissues were studied using a framework of reaction-diffusion equations. That approach assumes that there exist diffusing signaling molecules, called morphogens, which nonlinear interactions combined with different rates of diffusion may lead to a destabilization of a constant steady state and formation of spatially heterogeneous structures. The key mechanism of Turing type patterns is that an inhibitor diffuses faster than an activator. This means: there is a short range activation and a long range inhibition. However, in many developmental processes, dynamical and complex tissue topologies are likely to prevent the establishment of the long range inhibitor gradients. These observations support to look for a different inhibitory mechanism such as mechanical inhibition [66]. Furthermore, diffusion rates of typical morphogens are often found to be quite small [98].

Although the influence of morphogens on tissue mechanics (such as curvature) has been known for a long time, only very recent studies show that the interplay is reciprocal and applied curvatures can also influence the expression of genes, e.g. morphogens [34, 66, 88, 182]. The molecular origin of this mechanotransduction in cells and tissues is still a field of active research [187]. Furthermore it appears that tissues may act differently depending on direction of applied stress [181].

Based on these observations, we propose a non-Turing type model for pattern formation in biological tissues, coupling the expression of a morphogen with tissue mechanics. In the following, the terms "positive" and "negative" curvature refer to outward and inward bending, respectively, compared to the initial curvature of a tissue. Expanding the ideas of Cummings [58] we assume that a certain morphogen locally induces positive (negative) curvature, and in turn, positive (negative) curvature induces the expression of this morphogen (c.f. FIG 4.17).

The presented model combines a reaction-diffusion equation for the morphogen with an elastic gradient flow for tissue mechanics. Finite element simulations reveal that the postulated mechanism produces spontaneously a variety of curvature and morphogen patterns in an asymptotically stable way, i.e. insensitive to small changes in initial conditions. Based on various simulation results, we present detailed parameter studies of the model, analyzing a rescaled parameter space. We identify corresponding parameters to control pattern related scales, such as size, amount and curvature of appearing patches. Our results suggest that biomechanical interactions

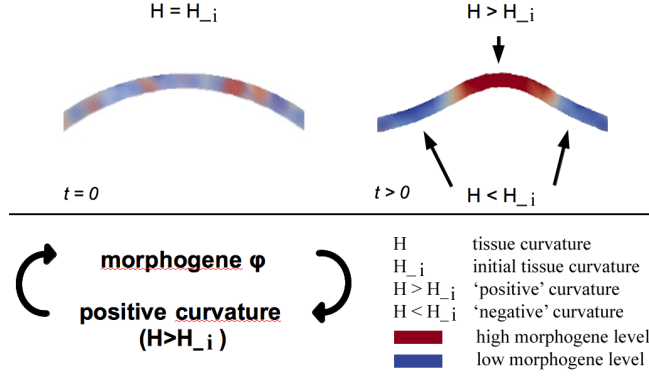


Figure 4.17: Positive feedback loop of morphogen expression and curvature. In combination with degradation, this mechanism leads to spontaneous curvature/morphogen patterns, starting from stochastic initial conditions. Note that positive curvature induces negative curvature at the edges of the domain, replacing the effect of a long range inhibitor molecule.

can constitute the missing link to the Turing long range inhibitor: positive curved domains induce negative curvatures at their edges; in these regions only morphogen degradation takes place (c.f. FIG 4.17).

To investigate if the postulated mechanism appears in real biological systems, we present different comparative studies. As experimental model we use *Hydra*-reaggregates (with β -Catenin as a marker for the symmetry break), constituting a well established biological model system to study early pattern formation. Since, in these reaggregates, symmetry break and pattern formation arise from nearly homogeneous tissue spheres, the model is, due to its simple geometry and well defined initial conditions, very suitable for comparison with simulation data.

Our comparative studies suggest that the presented mechanism could constitute a key mechanism for pattern formation in *Hydra*. However, experimental evidences are still weak. Further experimental work has to be done to approve this mechanism in *Hydra* and to investigate if it could constitute a key mechanism of pattern formation in other organisms as well. The presented section is closely related to [164].

4.4.2 Mathematical Model

Similar to the models of biological membranes considered in Section 4.1-4.3, $\vec{X} : U \rightarrow \Gamma$ is a parametric representation of a thin cell sheet Γ , where $U \subset \mathbb{R}^2$ and $\Gamma \subset \mathbb{R}^3$. The morphogen level is described by the function $\phi : U \rightarrow \mathbb{R}_{\geq 0}$; for each $\vec{X}(u_1, u_2) \in \Gamma$ the concentration $\phi(\vec{X})$ is identified with $\phi(u_1, u_2)$. Hence, ϕ is naturally moving with the deforming tissue, i.e. $d_t \phi = \nabla^\Gamma[\phi] \cdot \partial_t \vec{X} + \partial_t[\phi]$, where ∇^Γ is the surface gradient. For convenience of the reader, detailed descriptions of the used geometrical quantities are given in Appendix A.

To model the curvature dependent elastic properties of a thin cell tissue, we use again the Helfrich energy as a model for the tissue free energy, i.e.

$$F_{tissue} = \int_{\Gamma} \kappa(\phi)(H - H_0(\phi))^2 ds.$$

Here, H is the mean curvature and ds is the surface measure. The mechanical moduli κ and H_0 are usually taken as constant, if the surface is laterally homogeneous. κ constitutes the bending rigidity and reflects the stiffness of the tissue, the spontaneous curvature H_0 reflects the preferred local tissue curvature (which can be non-zero, e.g. if cells are wedge-shaped). As opposed to almost incompressible biomembranes, all tissues behave elastically with respect to lateral deformations. For simplicity, we assume here a local tissue incompressibility. However, in future investigations the impact of this assumption should be carefully investigated.

As already motivated in Section 4.4.1 we assume that the morphogen locally can influence tissue mechanics, such as stiffness and curvature. Here, we assume that tissue rigidity κ and the spontaneous curvature H_0 depend on the morphogen level ϕ . In first approximation we take $\kappa(\phi) = a + \alpha\phi$ and $H_0(\phi) = b + \beta\phi$ as linear functions of ϕ , where $a \geq 0$.

Adopting an energy point of view (and analogue to Section 2.4.2), the evolution of the tissue deformation \vec{X} up to time $T > 0$ in $U \times [0, T)$ is given by the following L^2 -gradient flow under the constraint of local incompressibility of the tissue:

$$d_t \vec{X} = -L_X \frac{\delta}{\delta \vec{X}} \left[F_{tissue} + \int_{\Gamma} \eta ds \right] \quad (4.11)$$

$$\partial_t \sqrt{g} = 0, \quad (4.12)$$

where d_t is the total time derivative, L_X is a kinetic coefficient, $\frac{\delta}{\delta \vec{X}}[\cdot]$ denotes the variation with respect to the arbitrary vector \vec{X} , and η is a local Lagrange multiplier [93] keeping the local area constant. Volume constraints are not considered, since in experiments with *Hydra*-reaggregates it appears that tissue spheres are able to exchange internal fluid with its surrounding [268]. The gradient flow (4.11) leads to a minimization of the free energy F_{tissue} under the constraint of incompressibility (4.12). For detailed calculation of the variations of F_{tissue} we refer to Section 2.4.3 and Appendix D.

In the following, we consider the dynamics of the morphogen ϕ within the tissue. In contrast to the modeling of membrane dynamics showing a fluid behavior with respect to lateral/tangential flows, the evolution of morphogens is modeled separately rather than obtained by a corresponding variation of a free energy. Beside the basic assumptions concerning diffusion and degradation [4, 98, 238], we define the morphogen production as a function depending on the surface curvature. We first assume that at the beginning of the pattern formation process, the tissue is arranged in

a mechanically relaxed configuration with initial curvature $H_i = H(t = 0, \vec{X})$. Based on recent findings [34, 66, 88] we consider that the expression of ϕ can be induced by local curvatures $H \neq H_i$. Especially in the following we assume that only in case $H > H_i$ (in contrast to $H < H_i$) the expression of ϕ is induced. (If both, negative and positive curvatures would induce morphogen expression, we would expect oscillations instead of stable patterns.) Hence, ϕ induces local positive curvatures and positive curvatures induce locally the expression of ϕ , constituting a positive feedback loop.

Using Michaelis-Menten kinetics (due to the existence of a maximal expression rate of the ϕ -promoter) and defining $H_{\geq 0} := \max\{(H - H_i), 0\}$, we obtain the dynamical equation for ϕ :

$$\partial_t \phi = \gamma \Delta^\Gamma[\phi] - \delta \phi + \left(\frac{\zeta H_{\geq 0}}{\omega + H_{\geq 0}} \right), \quad (4.13)$$

with constants $\gamma, \delta, \zeta, \omega \in \mathbb{R}_{\geq 0}$. Hence, the model is given by a nonlinear PDE system of fourth order, coupling the gradient flow for tissue mechanics (4.11) under the constraint of local area incompressibility (4.12) with the reaction-diffusion equation (4.13) for morphogen dynamics.

4.4.3 Nondimensionalization

Let us now derive the nondimensionalized version of the model introduced above. Since in Section 2.5, we have already nondimensionalized F_{tissue} (and the corresponding dynamical surface equation), we restrict us here to the dynamical equation of the morphogen.

Hence, we choose again

$$\vec{X} = \epsilon_x \vec{X}_c \quad \text{as well as} \quad t = \epsilon_t t_c,$$

with $[\vec{X}] = [\epsilon_x] = m$ and $[t] = [\epsilon_t] = s$ which implies $\Delta^\Gamma = \frac{1}{\epsilon_x^2} \Delta_c^\Gamma$, $H_{\geq 0} = \frac{1}{\epsilon_x} H_{\geq 0_c}$ and $\partial_t = \frac{1}{\epsilon_t} \partial_{t_c}$. Setting $\tilde{\gamma} = \frac{\epsilon_t \gamma}{\epsilon_x^2}$, $\tilde{\delta} = \epsilon_t \delta$, $\tilde{\zeta} = \frac{\epsilon_t}{\epsilon_\phi} \zeta$, $\tilde{\omega} = \epsilon_x \omega$ as well as $\phi = \epsilon_\phi \phi_c$ with $[\phi] = [\epsilon_\phi] = \frac{Mol}{m^2}$, we obtain

$$\partial_{t_c} \phi_c = \tilde{\gamma} \Delta_c^\Gamma[\phi_c] - \tilde{\delta} \phi_c + \left(\frac{\tilde{\zeta} H_{\geq 0_c}}{\tilde{\omega} + H_{\geq 0_c}} \right).$$

Choosing ϵ_t appropriately we can always guarantee $\tilde{\delta} = 1$, thus the total parameter space can be reduced to six independent constants, namely $\tilde{\gamma}, \tilde{\zeta}, \tilde{\omega}, \alpha, \beta$ and L_{X_c} .

4.4.4 Finite Element Approximation and Parameter Setup

Using the outlined modeling approach, we investigate the effect of different model parameters, system sizes and initial conditions on the pattern formation process. Hence, we numerically approximate equations (4.11)-(4.13), respectively the nondimensionalized form derived in Section 4.4.3, to study systematically spontaneous pattern formation induced by the proposed mechanism. In the following, we will work only with the nondimensionalized form of equations (4.11)-(4.13) and thus drop subindices c for convenience, i.e. we will work with dimensionless variables and parameters. For spatial discretization we use a biquadratic mixed finite element method (FEM) closely related to the approach presented in Chapter III. To consider a closed surface we adopt the extensions proposed in [104, 105] (for further details we refer to these works). The tissue surface is discretized using a quadrangular grid with 1664 grid points. For time discretization we use an adaptive semi-implicit Euler scheme. Based on the experimental setup for *Hydra*-reaggregates, initial conditions are the sphere $S_R(0)$, $R > 0$ for tissue geometry as well as a stochastic distribution of average $\langle \phi_0 \rangle = \int_{S_R(0)} \phi(t=0) ds$ for the morphogen concentration. In the following, we restrict our studies to the case of morphogens influencing the tissue curvature but not the tissue rigidity, setting $\kappa \equiv 1$ (i.e. $a = 1$ and $\alpha = 0$). Furthermore, we set $\tilde{\omega} = 1$ and $b = H_i$.

4.4.5 Numerical Results

Here, we will work only with the nondimensionalized form of equations (4.11)-(4.13). Thus, we drop subindices c for convenience, i.e. we will work with dimensionless variables and parameters. To investigate the variety of patterns produced by the presented model, we have performed more than 250 simulations using the nondimensionalized parameters $\tilde{\gamma}, \tilde{\zeta}$ as well as β and L_X (setting $a = \tilde{\omega} = 1$, $b = H_i$ and $\alpha = 0$, c.f. previous sections), starting with different values $\langle \phi_0 \rangle$. Depending on the exact choice of parameters, simulation results show two different types of long time behavior: either the system equilibrates with a symmetric medium curved pattern and seems to be stable at least for simulated times (c.f. FIG 4.18 A), or strong budding appears (c.f. FIG 4.18 B) till the numerics break down; it is likely that the limiting shape consist of fully budded patches. For the corresponding simulations we have set $R = 1, L_X = \tilde{\gamma} = 1, \beta = 1$ and $\tilde{\zeta} = 4$ in A,C,D as well as $\tilde{\zeta} = 8$ in B. Using different initial conditions (e.g. different values $\langle \phi_0 \rangle \neq 0$ on a smooth sphere) we obtain that equilibrium patterns appear to be independent of the exact choice of initial conditions, i.e. morphogen levels equal after some time (c.f. FIG 4.18 C) and corresponding equilibrium patterns are very similar (c.f. FIG 4.18 D). Even starting with no morphogen ($\langle \phi_0 \rangle = 0$) on a stochastically perturbed geometry yields the same result (not shown). Hence, the presented mechanism appears to be asymptotically stable and the formation of stable structures does not need the existence of any prepattern.

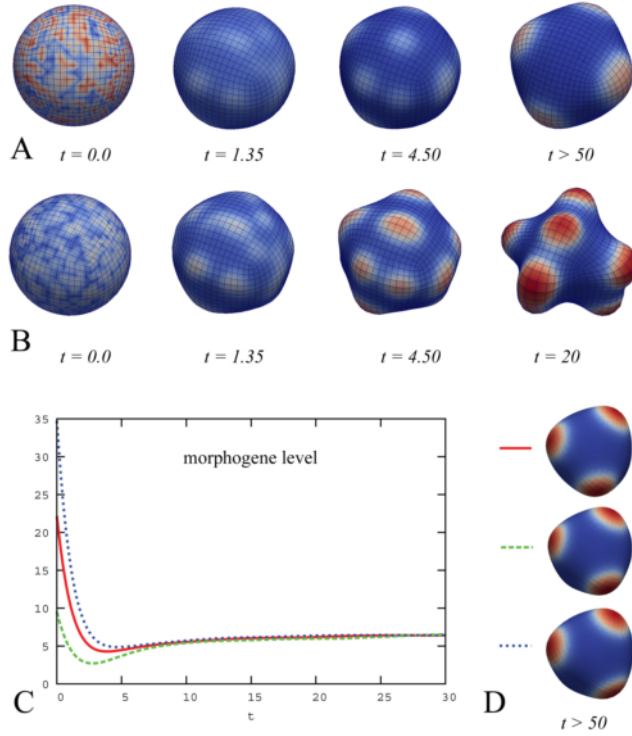


Figure 4.18: Simulation examples of spontaneous tissue pattern formation starting from stochastically distributed morphogen on a sphere. A: The system reaches a symmetric mechanical equilibrium at $t > 50$ (red color: $\phi = 3$, blue color $\phi = 0$). B: The system shows strong budding, numerics breaks down for $t > 20$; the likely equilibrium shape consists of fully budded morphogen patches (red color: $\phi = 6$, blue color $\phi = 0$). C-D: Equilibrium patterns are insensitive to different choices of initial conditions. C: Plot of total morphogen level $\int_{\Gamma} \phi ds$ during tissue development for different values $\langle \phi_0 \rangle = 10$ (green dashed line), $\langle \phi_0 \rangle = 22$ (red line) and $\langle \phi_0 \rangle = 35$ (blue dotted line). D: Corresponding equilibrium patterns (red color: $\phi = 1.5$, blue color $\phi = 0$).

Checking the influence of the different model parameters $\tilde{\gamma}$, $\tilde{\zeta}$, β and L_X on the corresponding emerging patterns, reveals the following relationships:

- Size of appearing patches can be controlled by diffusion: stepwise increasing $\tilde{\gamma} = 0.005$ up to $\tilde{\gamma} = 0.1$ (keeping $\tilde{\zeta} = 1$, $\beta = 4$ and $L_X = 0.01$ constant) results in bigger patches (c.f. FIG 4.19 A) and their number decreases.
- The distance between the patches (and hence the number as well, but not the size) and its curvature can be controlled by the strength of the curvature dependent production $\tilde{\zeta}$ (c.f. FIG 4.19 B) or alternatively by the morphogen level dependent curvature $\beta = 6$ (c.f. FIG 4.19 C): stepwise increasing $\tilde{\zeta} = 2$ up to $\tilde{\zeta} = 9$ but keeping $R = 1$, $\tilde{\gamma} = 0.01$, $\beta = 1$ and $L_X = 0.0001$ constant shows the same results as increasing $\beta = 2$ up to $\beta = 9$ but keeping $R = 1$, $\tilde{\gamma} = 0.01$, $\tilde{\zeta} = 1$, and $L_X = 0.0001$ constant. The only difference is the morphogen level, increa-

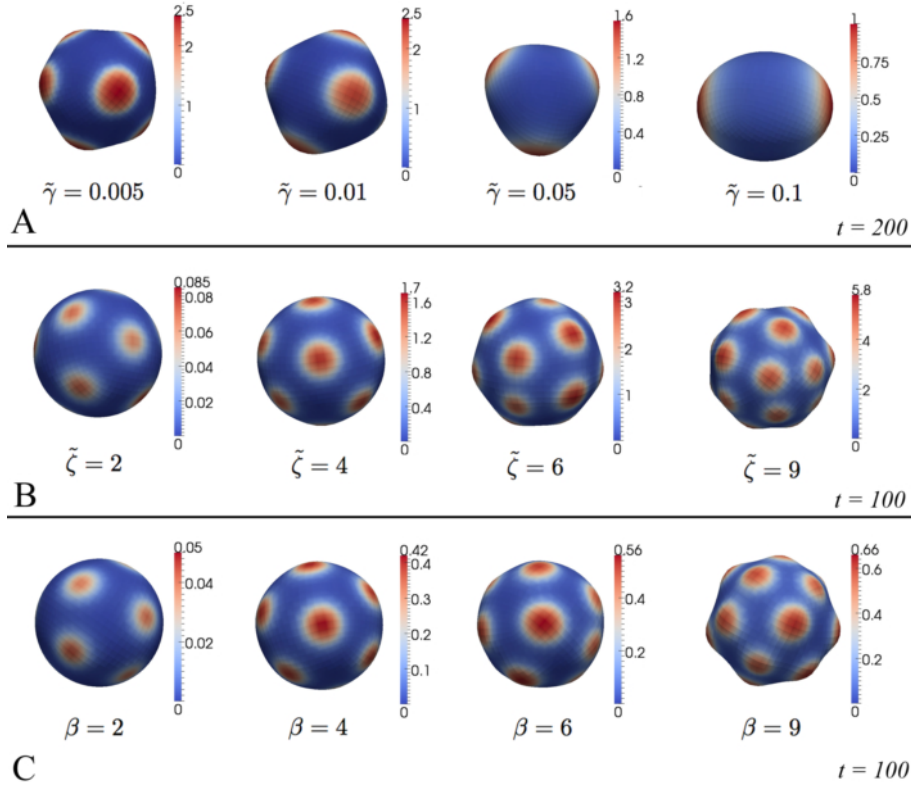


Figure 4.19: Influence of different model parameters on appearing patterns. A: Increasing diffusion by changing $\tilde{\gamma}$ results in bigger morphogen patches. B-C: An increase of curvature dependent morphogen expression $\tilde{\zeta}$ (B) results just as an increase of morphogen level dependent tissue curvature β (C) in more but still equally sized patches.

sing only if $\tilde{\zeta}$ increases. The similar influence of $\tilde{\zeta}$ and β on curvature patterns is as expected: both - curvature dependent production as well as morphogen level dependent curvature - depend linearly on the morphogen level, and additionally both are connected to each other in a positive feedback loop. Furthermore, it seems that these two parameters influence, whether full patch budding occurs or if the system stabilizes within a symmetric pattern.

- Changing L_X does not result in striking differences in pattern formation but only influences relevant time scales.

Investigating the dynamical behavior of the simulations reveals that all performed simulations typically show three qualitative different events during their evolution (c.f. FIG 4.20 B; for the corresponding simulation we have set $\beta = 8$, $R = 1$, $\tilde{\gamma} = 0.01$, $\tilde{\zeta} = 1$, and $L_X = 0.01$.):

- fast smoothing of initially stochastically distributed morphogen distribution,

- appearance of new and bigger slightly curved morphogen patches, and
- distinct visible curvature patterns coinciding with strong morphogen levels, either stabilizing at a symmetric pattern or strongly budding.

Interestingly, fluorescent microscopical data of evolving *Hydra*-reaggregates (using β -Catenin as marker for symmetry break) show striking similarities to our simulations (c.f. FIG 4.20 A-D): starting with stochastically distributed marker, the fluorescence level first decays [268], followed by appearance of morphogen patches first without visible curvatures (c.f. FIG 4.20 A: 7 h) then with local tissue curvatures (c.f. FIG 4.20 A: 25 h). Finally strongly curved patches with a high level of fluorescence appear (c.f. FIG 4.20 A: 45 h). Furthermore, reducing the total size of the system results in both, simulations (setting $R = 0.5$) and experiments, in a smaller number of strongly deformed patches (c.f. FIG 4.20 D). We would like to point out that all corresponding experiments with *Hydra*-reaggregates have been performed by Dr. Mihaela Žigman (Centre for Organismal Studies, Heidelberg University).

4.4.6 Discussion

In the present section we have proposed a new non-Turing type model for early pattern formation in tissue development. Based on recent experimental findings, the key assumption is a positive feedback loop between tissue curvature and morphogen production. We have shown numerically that this simple mechanism leads spontaneously to various morphogen and curvature patterns. Since presented experimental evidences for the proposed mechanism in *Hydra* are still weak, we hope to motivate further experimental research to prove or reject the presented mechanism for early pattern formation in *Hydra* or other organisms.

However, if further experimental evidences can be obtained, the proposed mechanism could constitute an essential step in the evolution of an initial homogeneous tissue sphere to a complex organism. This appears to be one of the greatest current unsolved biological questions [176].

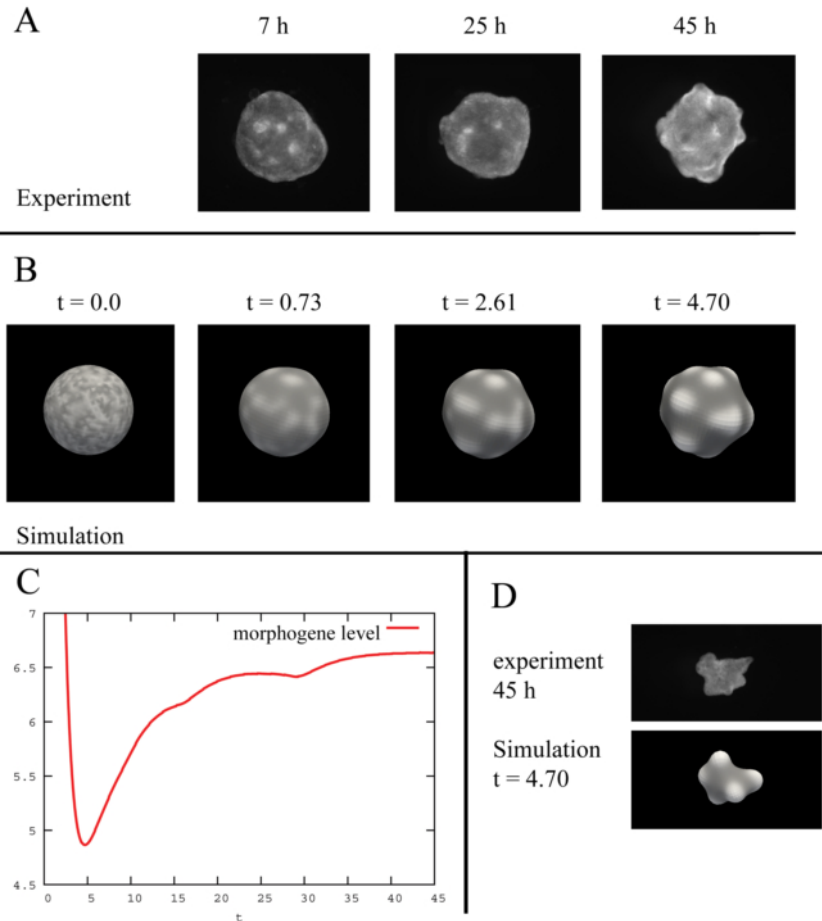


Figure 4.20: Comparative studies of simulations and experimental data showing early pattern formation in *Hydra*. A: Fluorescence microscopical pictures showing the temporal development of a *Hydra*-reaggregate, using fluorescent β -Catenin as marker for symmetry break. B: Comparative simulation data. C: Morphogen level in simulation corresponding to (B). D: Smaller experimental and simulated systems lead to less patches.

CHAPTER V

Summary and Outlook

Elastic thin surfaces constitute a basic building block of a variety of structures in biology. Prominent examples are biological membranes as well as cell tissues. Dynamics and stable patterns of both, membranes and tissues, play an indispensable role for the development and maintenance of cells and organs in any living being. Experimental approaches to study these surfaces are subject to strong limitations. Furthermore, tissues and membranes *in vivo* often show a very high degree of complexity, limiting reliable experimental analysis.

Avoiding these experimental difficulties, different mathematical models for biological surfaces have been developed and presented within this work. Due to its mathematical structure, specific non-standard numerical approaches have been developed, to enable simulations. Finally, extensive simulation experiments closely related to experimental data have been performed, resulting in various new insights into the deformation and pattern formation mechanisms of biological membranes and cell tissues.

Mathematical Modeling

Using the example of biological membranes, in Chapter II we have generalized a continuous mathematical model of elastic surface deformations induced by biomolecules on the surface itself. The dynamical 3D-model combines a parametric description for the deforming surface with a diffuse interface approach for the lateral dynamics of molecules. Our continuous model is based on the minimization of a free energy and is given as a strongly coupled nonlinear PDE system of fourth order, related to the Willmore flow and the Cahn-Hilliard equation.

Considering a biological membrane consisting of two different lateral phase separating components, the presented model accounts for differences in shape, rigidities, line tension, and monolayer area difference between the two coexisting phases. It is neither restricted to small curvatures nor to certain geometries and can be easily adapted to describe deformations of biological tissues.

Finite Element Approximation

In Chapter III we have presented a numerical method approximating solutions of the mathematical model presented in Chapter II. Since strongly coupled geometric nonlinear PDE systems of fourth order (describing strong curvatures) have been considered, numerical implementations have required a non-standard approach. For the first time, we have presented a numerical scheme treating realistic dynamics of lateral inhomogeneous biological membranes without restriction to small curvatures.

The proposed discretization is based on the finite element method, combining a mixed finite element approach for spatial discretization with a semi-implicit Euler scheme for temporal discretization. Furthermore, we have relied on an algorithm keeping good properties with respect to the distribution of meshpoints during deformations without violating effective local mass conservation. In order to prove the reliability of the presented algorithm, we have numerically proved energy decay in time, experimental order of convergence as well as qualitative and quantitative stability analyses.

A Multiscale Approach Investigating Curvature Modulated Sorting in Membranes

In Section 4.1, an extended continuous multiscale model for curvature modulated sorting in biological membranes has been proposed. Here, we have restricted ourselves to fixed membranes, e.g. attached to a rigid substrate. We have presented simulations using a finite element approach and have derived detailed functional relationships from the molecular level using data from DPD studies. Our simulations show that gradients in the three elastic moduli result in distinct metastable minimum patterns and that the decomposition time decreases exponentially with increasing difference in the modulus or corresponding curvature gradient. Additionally, we have shown that the stability of curvature modulated patterns increases with increasing moduli or curvature gradients. Presented phase diagrams allow to estimate if curvature modulated sorting may occur for a given set of geometry and elastic parameters.

Furthermore, our results emphasize that local sorting is quite sensitive to the specific choice of parameters and functional dependencies of macroscopic models. Comparing minimum patterns computed with a model based on nonlinear upscaled parameter functions from microscopic DPD studies and the commonly adopted linear functions shows significant differences. This shows the relevance of a careful choice of fundamental relationships and underlines the importance of multiscale approaches in biological systems.

Impact of Elastic Parameters on Membrane Budding

In Section 4.2, various finite element simulations of the basic model have been performed to study the impact of the elastic parameters on membrane shape and budding. To do so, we have systematically varied the (diffuse) line tension, the elastic moduli - the bending rigidity κ , the spontaneous curvature H_0 and the Gaussian rigidity κ_G - of the two membrane components as well as the monolayer area difference. For the first time, we have shown that the influence of the Gaussian curvature (i.e. the Gaussian rigidity κ_G) on membrane dynamics is similar to the influence of the other elastic moduli κ , H_0 and σ .

Our simulation results are in good qualitative and quantitative agreement with recent experimental and theoretical (sharp-interface) results. Besides individual qualitative differences, we have shown that changes in each of the five elastic parameters can be used to cause or prevent a budding event. Furthermore, we have found that for each elastic parameter σ , κ , κ_G , and H_0 the budding time decreases exponentially with further changes in these parameters once a critical value has been exceeded.

Lateral Sorting and Transversal Communication in Coupled Monolayers

In Section 4.3, we have studied a continuous model of two coupled monolayers consisting of different molecule species. Coupling of the layers has been achieved by an elastic intermonolayer-distance energy, depending on the molecule lengths in the two opposed layers. We have shown that both, the curvature of one layer as well as the distance to the other layer, can influence the chemistry distribution in the other layer: our results show that phase separation and local accumulation of membrane components in stretched regions can be induced by a mismatch between molecule size and bilayer thickness. Furthermore, our results suggest that this thickness mismatch effect can serve as a mechanism to synchronize phases across the bilayer membrane. Additionally, we have analyzed the interplay between membrane curvature and lateral sorting of molecules, showing that differences in stiffness and shape of molecules lead to various possible scenarios of interplays between lateral sorting and local curvature generating mechanisms.

On the Coupling of Tissue Mechanics with Morphogen Expression: A New Model for Early Pattern Formation in Hydra Polyps

In Section 4.4, we have proposed a new mechanism for symmetry break and early pattern formation in biological tissues. Based on recent experimental findings, the key property of this mechanism is the coupling of morphogen expression with tissue deformations in a positive feedback loop. We have formulated this idea in terms of a mechanobiological model coupling an elastic gradient flow for tissue mechanics with

a reaction-diffusion equation for the morphogen, resulting in a nonlinear PDE system of fourth order. Using the finite element method, systematic simulations have shown that various patterns appear spontaneously and are asymptotically stable with respect to stochastic initial conditions. Furthermore, we have analyzed in which way different model parameters influence characteristic properties of the emerging patterns. Comparison with experimental data using *Hydra*-reaggregates have indicated that the proposed mechanism might be a key mechanism for pattern formation in *Hydra*. However, further experiments are necessary to confirm this hypothesis.

Outlook

In this thesis, we have developed new mathematical models and numerical approximation techniques to describe dynamics and steady states of biological membranes and cell tissues. Presented models and numerics are neither restricted to certain geometries (except topological changes) nor to small surface curvatures and account for realistic dynamics. Furthermore, presented parametric approaches require relatively low computational costs and hence are suitable for performing large numbers of simulations (e.g. parameter searches).

Corresponding mathematical models are given in terms of nonlinear coupled PDE systems of fourth order. Proofs concerning existence and uniqueness of solutions have been beyond the scope of this work. However, parts of this thesis have motivated corresponding analysis for at least one of the presented models [165]. For all other models derived within this work, rigorous analytical work proving well-posedness is a challenging open problem, analysis of some related but simplified equations have been obtained by [78, 81, 82, 134, 198].

As already pointed out, presented approaches may serve as a future basis to intensify the junction between experimental and different theoretical techniques: parameterization of the presented models e.g. based on a comparison of simulations with experimental data on experimentally accessible time and space scales. Based on this, mechanochemical processes on experimentally inaccessible scales could be investigated theoretically via simulations, in turn motivating new experimental approaches. Particularly, upscaling techniques deriving macroscopical models from lower (discrete) scales are desirable. Using molecular dynamical techniques, first upscaling approaches for membrane models have been presented within this thesis, as well as in [55, 147, 159, 222]. An alternative approach, which may be suitable for tissue models as well as for membrane models, is rigorous multiscale analysis (e.g. based on the density functional theory [208]).

Within this work, novel continuous models and their computation have been used to investigate and explain different new mechanisms of pattern formation in membranes and tissues. On the one hand, presented models and techniques can be used

in the future to intensify the conjunction between different theoretical and experimental techniques in membrane and tissue research. On the other hand, presented simulation results can motivate future research to focus on new aspects, e.g. the role of the Gaussian curvature in membrane sorting and budding or the influence of tissue deformations on embryonic pattern formation processes.

APPENDICES

APPENDIX A

Notation

For the convenience of the reader, let us shortly repeat the general notations and definitions used in this thesis. For a more detailed survey of differential geometry we refer to [61, 64, 163].

General Notation

| | |
|-------------------------|---|
| a | scalar, |
| \vec{a} | covariant vector a_i , e.g. $(\vec{a})_i = a_i$, |
| \mathbf{a} | matrix, e.g. $(\mathbf{a})_{ij} = a_{ij}$, |
| $\vec{a} \cdot \vec{b}$ | standard vector scalar product, e.g. $(\vec{a} \cdot \vec{b}) = \sum_i a_i b_i$, |
| \mathbf{ab} | standard matrix multiplication, e.g. $(\mathbf{ab})_{ik} = \sum_j a_{ij} b_{jk}$, |
| $\bar{\mathbf{a}}$ | inverse of a matrix, e.g. $(\mathbf{a}^{-1})_{ij} = (\bar{\mathbf{a}})_{ij} = \bar{a}^{ij}$, |
| \vec{n} | unit normal, |
| H | mean curvature, |
| H_0 | spontaneous curvature, |
| K | Gaussian curvature. |

Differential and Integral Operators

| | |
|--|--|
| $\partial_i[\cdot]$ | partial derivative with respect to u_i , |
| $\partial_i \vec{X}$ | basis vector of the tangential space, e.g. $\partial_i \vec{X} = \partial_i [\vec{X}]$, |
| $\partial_t[\cdot]$ | partial time derivative, |
| $d_t[\cdot]$ | total time derivative, |
| $(g_{ij})_{i,j}$ | first fundamental tensor, $g_{ij} = \partial_i \vec{X} \cdot \partial_j \vec{X}$. It holds: $g_{ij} = g_{ji}$, |
| $(b_{ij})_{i,j}$ | second fundamental tensor, $b_{ij} = -\partial_i \vec{X} \cdot \partial_j \vec{n}$. It holds: $b_{ij} = b_{ji}$, |
| g^{ij} | component of the inverse first fundamental tensor, |
| b^{ij} | contravariant component of the second fundamental tensor, $b^{ij} = \sum_{kl} g^{ik} g^{jl} b_{kl}$, |
| α^i | contravariant characterization of a vector or matrix component or a derivative regarding index i , e.g. $\alpha^i = \sum_j g^{ij} \alpha_j$ where $(g^{ij})_{i,j}$ is the inverse of the first fundamental tensor and $\alpha \in \{a, a_j, \partial, \nabla\}$, |
| a_j^i | mixed notation, $a_j^i = \sum_u g_{ju} a^{ui} = \sum_u g^{ui} a_{ju}$ and $a^j_i = \sum_u g_{iu} a^{ju} = \sum_u g^{ju} a_{ui}$. It holds: $\sum_u g^{iu} g_{uj} = g^j_j = \delta^j_j$, |
| $\nabla^\Gamma[\cdot]$ | first surface gradient: $\nabla^\Gamma[f] = \sum_{i,j} g^{ij} \partial_j[f] \partial_i \vec{X}$, |
| $\Delta^\Gamma[\cdot]$ | first surface Laplacian: $\Delta^\Gamma[f] = \frac{1}{\sqrt{g}} \sum_{i,j} \partial_i \left[\sqrt{g} g^{ij} \partial_j[f] \right]$. For the corresponding Green's formula and further integral theorems we refer to reference [261], |
| $\widehat{\nabla}^\Gamma[\cdot]$ | second surface gradient: $\widehat{\nabla}^\Gamma[f] = \sum_{i,j} \overline{b^{ij}} K \partial_j[f] \partial_i \vec{X}$, where $(\overline{b^{ij}}) = (b_{ij})^{-1}$, |
| $\widehat{\Delta}^\Gamma[\cdot]$ | second surface Laplacian: $\widehat{\Delta}^\Gamma[f] = \frac{1}{\sqrt{g}} \sum_{i,j} \partial_i \left[\sqrt{g} \overline{b^{ij}} K \partial_j[f] \right]$. For the corresponding Green's formula and further integral theorems we refer to [259]. |
| $\delta^\alpha[F]$ | Fréchet-derivative or variation with respect to α , |
| $\delta F / \delta \vec{X}(\vec{u})$ | strong formulation of $\delta \vec{X}[F]$ in $\vec{X}(\vec{u})$, |
| $\int \dots ds$ | surface integral on a manifold, where $ds = \sqrt{g} d^2u$, and g is the determinant of the first fundamental tensor, |
| H | mean curvature, $H = \text{trace}(b_i^j)$, |
| K | Gaussian curvature, $K = \det(b_i^j)$, |
| Γ_{jk}^i | Christoffel-symbol, it holds $\Gamma_{jk}^i = \Gamma_{kj}^i = \frac{1}{2} \sum_l g^{il} \left(\partial_k [g_{jl}] + \partial_j [g_{lk}] - \partial_l [g_{jk}] \right)$. |
| $\nabla_k [a_{j_1 \dots j_Q}^{i_1 \dots i_P}]$ | covariant derivative of the type-(P/Q)-tensor field in the direction of k . In particular it holds: $\nabla_k [a] = \partial_k [a]$, $\nabla_k [a^i] = \partial_k [a^i] + \sum_l \Gamma_{kl}^i a^l$, $\nabla_k [a_j^i] = \partial_k [a_j^i] + \sum_l \Gamma_{kl}^i a_j^l - \sum_l \Gamma_{kj}^l a_l^i$ and $\nabla_k [a^{ji}] = \partial_k [a^{ji}] + \sum_l \Gamma_{kl}^i a^{jl} + \sum_l \Gamma_{kj}^l a^{li}$. |

APPENDIX B

Transition Between Sharp and Diffuse Line Tension

Line tension forces in the dynamical equation for the membrane deformation \vec{X} , e.g. equation (2.8), result from the Cahn-Hilliard part of the free energy. Hence, they are based on a diffuse interface. Nevertheless, in case of already separated phases in the largest part of Γ it holds $\phi \equiv \pm 1$. The line tension forces act only in the transition region of width ξ at the boundary of the phases, where $-1 < \phi < 1$.

However, many theoretical approaches consider already separated phases approximating the diffuse line tension by a sharp one [6, 17, 60, 124]. In this sharp-interface models the line tension energy is given by the line integral

$$F_{si} = \sigma_{si} \oint dl$$

along the domain boundary, where σ_{si} is a surface energy constant.

The sharp line tension energy F_{si} is basically the limit $\xi \rightarrow 0$ of the reformulated diffuse Cahn Hilliard energy

$$F_\epsilon = \hat{\sigma} \int_{\Gamma} \left(\frac{\xi}{2} |\nabla^\Gamma[\phi]|^2 + \frac{1}{\xi} f(\phi) \right) ds, \quad (\text{B.1})$$

weighted by $\hat{\sigma} = \sigma\xi$, where ξ is small and related to the thickness of the diffuse interface between the phases (in the limit $\xi \rightarrow 0$; $\hat{\sigma}$ is kept constant). Considering the limit $\xi \rightarrow 0$, the relationship between sharp and diffuse interface line tension constants is given by [135]

$$\sigma_{si} = 2\hat{\sigma} \int_{-1}^1 \sqrt{\frac{f(\phi)}{2}} d\phi. \quad (\text{B.2})$$

Hence, using $f(\phi) = \frac{9}{32}(\phi^2 - 1)^2$ the following simple relationship between sharp and diffuse line tension is obtained:

$$\sigma_{si} = 2\sigma\xi \int_{-1}^1 \sqrt{\frac{9}{32} \frac{(z^2 - 1)^2}{2}} dz = \sigma\xi. \quad (\text{B.3})$$

Choosing $f(\phi) = \frac{1}{2}(\phi^2 - 1)^2$ in equation (B.2) yields $\sigma_{si} = \frac{4}{3}\widehat{\sigma}$, matching with the very recent results of [84] who investigated the line tension limit on arbitrary curved surfaces.

APPENDIX C

Technical Remarks

In this Appendix we summarize some important results of differential geometry which are used in this thesis. We remember that δ^\perp and δ^k constitute the variation in normal direction and k -tangential direction regarding Γ , respectively, where $\delta^t = \sum_k \delta^k$ (c.f. Section 2.2.2).

We mention furthermore the following geometric relations derived in [267]

$$\delta^\perp[H] = -\Delta^\Gamma[\psi] - \psi(H^2 - 2K) \quad (\text{C.1})$$

and

$$\delta^\perp[\sqrt{g}] = \psi H \sqrt{g}, \quad (\text{C.2})$$

where g is the determinant of the first fundamental tensor [64] (corresponding definitions of geometric operators and quantities are given for convenience in the Appendix A).

Following [73] it holds that

$$\delta^\perp[K] = \widehat{\Delta}^\Gamma[\psi] - HK\psi, \quad (\text{C.3})$$

where $\widehat{\Delta}^\Gamma$ is the second surface laplacian (c.f. Appendix A). Following [126], it has been shown that

$$\delta^\perp[g^{ij}] = -2 \sum_k g^{jk} b_k^i \psi = -2b^{ij}\psi, \quad (\text{C.4})$$

$$\delta^t[g^{ij}] = -\nabla^i[\psi^j] - \nabla^j[\psi^i], \quad (\text{C.5})$$

where (g_{ij}) is the first fundamental tensor, (b_{ij}) is the second fundamental tensor, ∇_i is the covariant derivative in the direction of i and raised indices denote contravariant indices (c.f. Appendix A). Furthermore, it holds

$$\delta^t[b_{ij}] = \sum_k (\nabla_j[\psi^k] b_{ik} + \nabla_i[\psi^k] b_{jk} + \nabla_k[b_{ij}] \psi^k) \quad (\text{C.6})$$

according to [41], as well as the Mainardi-Codazzi-equation [50]

$$\nabla_c [b_{ab}] = \nabla_b [b_{ac}]. \quad (\text{C.7})$$

In addition, we will use the results of [119] stating

$$\sum_a \nabla_a [b^a_b] = \partial_b [H]. \quad (\text{C.8})$$

We would like to point out that in some of the publications cited above, the mean curvature \hat{H} differs from the definition used in this thesis, e.g. the relation $\hat{H} = -H/2$ or $\hat{H} = -H$ has been adopted.

APPENDIX D

Fréchet Derivatives

In the following, we present the calculation of the Fréchet derivatives of F_1, F_2 and F_3 (c.f. Section 2.4.1). Calculations have been already presented in [163], here we present a significantly shortened version of the proofs. In certain parts, proofs could be further shortened using for example the calculus of surface gradients [15, 83]. However, here we will rely on a formulation which should be easy to follow for non-experts in the field of differential geometry.

Lemma D.1.

$$\begin{aligned} \frac{\delta^\perp[F_1]}{\delta \vec{X}} &= -\Delta^\Gamma[\kappa(\phi)(H - H_0(\phi))] \\ &\quad -\kappa(\phi)(H - H_0(\phi))(H^2 - 2K) + \frac{\kappa(\phi)}{2}(H - H_0(\phi))^2 H \end{aligned}$$

Proof: Using the chain rule, $ds = \sqrt{g}d^2u$ as well as (C.1) and (C.2) yields

$$\begin{aligned} \delta^\perp[F_1] &= \int \left\{ \kappa(\phi)(H - H_0(\phi))(-\Delta^\Gamma[\psi] - \psi(H^2 - 2K)) \right. \\ &\quad \left. + \frac{\kappa(\phi)}{2}(H - H_0(\phi))^2 \psi H \right\} \sqrt{g} d^2u. \end{aligned}$$

Using twice the Green's identities for the first surface Laplace operator [261] results in

$$\begin{aligned} \delta^\perp[F_1] &= \int \left\{ -\Delta^\Gamma[\kappa(\phi)(H - H_0(\phi))\psi - \kappa(\phi)(H - H_0(\phi))(H^2 - 2K)\psi] \right. \\ &\quad \left. + \frac{\kappa(\phi)}{2}(H - H_0(\phi))^2 \psi H \right\} \sqrt{g} d^2u, \end{aligned}$$

leading to the assertion of the lemma. □

Lemma D.2.

$$\frac{\delta^\perp[F_2]}{\delta \vec{X}} = -\widehat{\Delta}^\Gamma[\kappa_G(\phi)].$$

Proof: Using the product rule and considering (C.3), we obtain

$$\begin{aligned} \delta^\perp[F_2] &= \int \kappa_G(\phi)(-\widehat{\Delta}^\Gamma[\psi] - HK\psi)\sqrt{g} d^2u + \int \kappa_G(\phi)K\psi H\sqrt{g} d^2u \\ &= -\int \kappa_G(\phi)\widehat{\Delta}^\Gamma[\psi]\sqrt{g} d^2u. \end{aligned}$$

Green's identities for the second Laplacian [261] yield

$$\delta^\perp[F_2] = -\int \widehat{\Delta}^\Gamma[\kappa_G(\phi)]\psi\sqrt{g} d^2u.$$

□

Lemma D.3.

$$\frac{\delta^\perp[F_3]}{\delta \vec{X}} = -\xi^2 \sum_{i,j} b^{ij} \partial_i[\phi] \partial_j[\phi] + H\left(\frac{\xi^2}{2}(\nabla^\Gamma[\phi])^2 + f(\phi)\right).$$

Proof: Equality (C.2) and the product rule yield

$$\begin{aligned} \delta^\perp[F_3] &= \int \delta^\perp\left[\frac{\xi^2}{2}(\nabla^\Gamma[\phi])^2 + f(\phi) + \right]\sqrt{g} d^2u \\ &\quad + \int \left\{\frac{\xi^2}{2}(\nabla^\Gamma[\phi])^2 + f(\phi)\right\}\psi H\sqrt{g} d^2u. \end{aligned}$$

Using $(\nabla^\Gamma[\phi])^2 = \sum_{i,j} g^{ij} \partial_i[\phi] \partial_j[\phi]$ as well as (C.4) we obtain

$$\begin{aligned} \delta^\perp[F_3] &= \int \frac{\xi^2}{2} \sum_{i,j} \delta^\perp[g^{ij}] \partial_i[\phi] \partial_j[\phi] \sqrt{g} d^2u \\ &\quad + \int \left\{\frac{\xi^2}{2}(\nabla^\Gamma[\phi])^2 + f(\phi)\right\}\psi H\sqrt{g} d^2u \\ &= \int \left\{-\xi^2 \sum_{i,j} b^{ij} \partial_i[\phi] \partial_j[\phi] + \frac{\xi^2}{2}H((\nabla^\Gamma[\phi])^2 + f(\phi))\right\}\psi\sqrt{g} d^2u, \end{aligned}$$

which yields the assertion of the Lemma. □

Proposition D.4.

$$\delta^k[g_{ij}] = \partial_i[\partial_k \vec{X} \psi^k] \cdot \partial_j \vec{X} + \partial_j[\partial_k \vec{X} \psi^k] \cdot \partial_i \vec{X}$$

Proof: It holds that

$$\delta^k [g_{ij}] = \partial_i [\delta^k [\vec{X}]] \cdot \partial_j \vec{X} + \partial_i \vec{X} \cdot \partial_j [\delta^k [\vec{X}]].$$

The claim of the proposition directly follows from

$$\delta^k [\vec{X}] := \left. \frac{d}{d\epsilon} [\vec{X} + \epsilon \partial_k \vec{X} \psi^k] \right|_{\epsilon=0} = \partial_k \vec{X} \psi^k.$$

□

Proposition D.5.

$$\delta^t [H] = \sum_{i,j,k} g^{ij} \nabla_k [b_{ij}] \psi^k.$$

Proof: It holds that

$$\begin{aligned} \delta^t [H] &= \delta^t \left[\sum_i b_i^i \right] = \delta^t \left[\sum_{i,j} g^{ij} b_{ij} \right] \\ &= \sum_{i,j} \delta^t [g^{ij}] b_{ij} + \sum_{i,j} g^{ij} \delta^t [b_{ij}], \end{aligned}$$

due to (C.5) and (C.6). Since $(b_{ij})_{i,j}$ and $(g^{ij})_{i,j}$ are symmetric, it follows that

$$\delta^t [H] = -2 \sum_{i,j} \nabla^i [\psi^j] b_{ij} + 2 \sum_{i,j,k} g^{ij} \nabla_i [\psi^k] b_{jk} + \sum_{i,j,k} g^{ij} \nabla_k [b_{ij}] \psi^k.$$

Furthermore, it holds

$$\begin{aligned} 2 \sum_{i,j,k} g^{ij} \nabla_i [\psi^k] b_{jk} &= 2 \sum_{j,k} \nabla^j [\psi^k] b_{jk} \\ &= 2 \sum_{i,j} \nabla^i [\psi^j] b_{ij}, \end{aligned}$$

i.e. the first two terms vanish, and the claim holds true. □

Proposition D.6. *For any $\eta \in C^1(U)$ it holds:*

$$\int \eta \delta^t [\sqrt{g}] d^2 u = - \sum_{k,u} \int \partial^u [\eta] g_{uk} \psi^k \sqrt{g} d^2 u.$$

Proof: Applying the chain rule to the determinant yields

$$\int \eta \delta^k [\sqrt{g}] d^2 u = \int \frac{1}{2} \sum_{i,j} \sqrt{g} g^{ij} \delta^k [g_{ij}] \eta d^2 u.$$

Using Proposition D.4 and integration by parts yields

$$\int \eta \delta^k [\sqrt{g}] d^2 u = - \int \sum_{i,j} \partial_i [\eta g^{ij} \sqrt{g} \partial_j \vec{X}] \cdot \partial_k \vec{X} \psi^k d^2 u.$$

Since $\sum_{i,j} \partial [g^{ij} \sqrt{g} \partial_j \vec{X}] \cdot \partial_k \vec{X} = -\sqrt{g} \Delta^\Gamma \vec{X} \cdot \partial_k \vec{X} = \sqrt{g} H \vec{n} \cdot \partial_k \vec{X} = 0$ it holds that

$$\int \eta \delta^k [\sqrt{g}] d^2 u = - \sum_j \int \partial^j [\eta] g_{jk} \psi^k \sqrt{g} d^2 u.$$

Since $\delta^t = \sum_k \delta^k$, the claim directly follows. \square

Lemma D.7.

$$\frac{\delta^k [F_1]}{\delta \vec{X}} = -\frac{1}{2} \partial^k [\kappa(\phi)] (H - H_0(\phi))^2 + \kappa(\phi) (H - H_0(\phi)) \partial^k [H_0(\phi)].$$

Proof: Using the product rule we obtain

$$\begin{aligned} & \delta^t \left[\frac{1}{2} \int \kappa(\phi) (H - H_0(\phi))^2 \sqrt{g} d^2 u \right] \\ &= \frac{1}{2} \int \kappa(\phi) \delta^t [(H - H_0(\phi))^2] \sqrt{g} d^2 u + \frac{1}{2} \int \kappa(\phi) (H - H_0(\phi))^2 \delta^t [\sqrt{g}] d^2 u. \end{aligned}$$

Propositions D.5 and D.6 as well as the product rule provide

$$\begin{aligned} & \delta^t \left[\frac{1}{2} \int \kappa(\phi) (H - H_0(\phi))^2 \sqrt{g} d^2 u \right] \\ &= \int \kappa(\phi) (H - H_0(\phi)) \sum_{i,j,k} g^{ij} \nabla_k [b_{ij}] \psi^k \sqrt{g} d^2 u \\ &\quad - \frac{1}{2} \sum_{k,u} \int \partial^u [\kappa(\phi)] (H - H_0(\phi))^2 g_{uk} \psi^k \sqrt{g} d^2 u \\ &\quad - \sum_{k,u} \int \kappa(\phi) (H - H_0(\phi)) \partial^u [H] g_{uk} \psi^k \sqrt{g} d^2 u \\ &\quad + \sum_{u,k} \int \kappa(\phi) (H - H_0(\phi)) \partial^u [H_0(\phi)] g_{uk} \psi^k \sqrt{g} d^2 u. \end{aligned}$$

Due to (C.7) and (C.8) and since the covariant derivatives and the first metric tensor commute, it follows that

$$\begin{aligned} \sum_{i,j} g^{ij} \nabla_k [b_{ij}] &= \sum_{i,j} g^{ij} \nabla_j [b_{ik}] = \sum_j \nabla_j \left[\sum_i g^{ij} b_{ik} \right] \\ &= \sum_j \nabla_j [b^j_k] = \partial_k [H] = \sum_u g_{uk} \partial^u [H]. \end{aligned}$$

Since the first and third term cancel each other, we obtain

$$\begin{aligned} & \delta^t \left[\frac{1}{2} \int \kappa(\phi) (H - H_0(\phi))^2 \sqrt{g} d^2 u \right] \\ &= -\frac{1}{2} \sum_{k,u} \int \partial^u [\kappa(\phi)] (H - H_0(\phi))^2 g_{uk} \psi^k \sqrt{g} d^2 u \\ &\quad + \sum_{k,u} \int \kappa(\phi) (H - H_0(\phi)) \partial^u [H_0(\phi)] g_{uk} \psi^k \sqrt{g} d^2 u. \end{aligned}$$

\square

Proposition D.8.

$$\sum_i \bar{b}^i_j b_{ik} = g_{jk},$$

where \bar{b}^i_j are components of the inverse of the matrix (b_i^j) .

Proof: It holds that

$$\sum_i \bar{b}^i_j b_{ik} = \sum_i \left(\sum_l \bar{g}^{li} b_{jl} \right) b_{ik}$$

and since $(AB)^{-1} = B^{-1}A^{-1}$ it follows that

$$\begin{aligned} \sum_i \bar{b}^i_j b_{ik} &= \sum_i \left(\sum_l \bar{g}^{lj} \bar{b}_{il} \right) b_{ik} \\ &= \sum_i \left(\sum_l g_{lj} \bar{b}_{il} \right) b_{ik} = \sum_l \left(\sum_i \bar{b}_{il} b_{ik} \right) g_{lj} = \sum_l \delta_l^k g_{lj} = g_{kj}, \end{aligned}$$

as it is claimed. □

Proposition D.9.

$$\delta^t [K] = \sum_{i,j,k} \bar{b}^i_j \nabla_k [b_i^j] \psi^k K.$$

Proof: It holds that

$$\delta^t [K] = \sum_{i,j,k} K \bar{b}^i_j \delta^t [g^{ki}] b_{jk} + \sum_{i,j,k} K \bar{b}^i_j g^{ki} \delta^t [b_{jk}].$$

Using (C.8) and (C.6), tedious calculations [163] yield

$$\begin{aligned} \delta^t [K] &= -2 \sum_{i,j,k} K \bar{b}^i_j \nabla^k [\psi^i] b_{jk} \\ &\quad + 2 \sum_{i,j,k} K \bar{b}^i_j b_{jk} \nabla^i [\psi^k] + \sum_{i,j,k,u} K \bar{b}^i_j g^{ki} \nabla_u [b_{jk}] \psi^u. \end{aligned}$$

Proposition D.8 yields

$$\begin{aligned} \delta^t [K] &= -2 \sum_{i,k} g_{ik} K \nabla^k [\psi^i] + 2 \sum_{i,k} K g_{ik} \nabla^i [\psi^k] + \sum_{i,j,k,u} K \bar{b}^i_j g^{ki} \nabla_u [b_{jk}] \psi^u \\ &= \sum_{i,j,k,u} \bar{b}^i_j g^{ki} \nabla_u [b_{jk}] \psi^u K. \end{aligned}$$

Since the covariant derivatives and the first metric tensor commute, we obtain

$$\delta^t [K] = \sum_{i,j,u} \bar{b}^i_j \nabla_u [b_j^i] \psi^u K,$$

which is the claim. □

Lemma D.10.

$$\frac{\delta^k[F_2]}{\delta \vec{X}} = -\partial^k[\kappa_G(\phi)]K.$$

Proof: It holds that

$$\partial^t \left[\int \kappa_G(\phi) K \sqrt{g} d^2u \right] = \int \kappa_G(\phi) \partial^t [K] \sqrt{g} d^2u + \int \kappa_G(\phi) K \partial^t [\sqrt{g}] d^2u.$$

Using Propositions D.5 and D.9, the product rule as well as the definition of the covariant derivative, we obtain

$$\begin{aligned} \partial^t \left[\int \kappa_G(\phi) K \sqrt{g} d^2u \right] &= \sum_{i,j,k} \kappa_G(\phi) \bar{b}_j^i \left\{ \partial_k [b_j^i] + \sum_l (\Gamma_{kl}^i b_j^l - \Gamma_{kj}^l b_l^i) \right\} K \psi^k \sqrt{g} d^2u \\ &\quad - \sum_{u,k} \int \partial^u [\kappa_G(\phi)] K g_{uk} \psi^k \sqrt{g} d^2u - \sum_k \int \kappa_G(\phi) \partial_k [K] \psi^k \sqrt{g} d^2u. \end{aligned}$$

Applying the chain rule to the determinant leads to

$$\begin{aligned} \partial^t \left[\int \kappa_G(\phi) K \sqrt{g} d^2u \right] &= \int \kappa_G(\phi) \left\{ \sum_{i,j,k,l} \bar{b}_j^i b_j^l \Gamma_{kl}^i - \sum_{i,j,k,l} \bar{b}_j^i b_l^i \Gamma_{kj}^l \right\} \psi^k K \sqrt{g} d^2u \\ &\quad - \sum_{u,k} \int \partial^u [\kappa_G(\phi)] K g_{uk} \psi^k \sqrt{g} d^2u. \end{aligned}$$

Since $\sum_l \bar{b}_i^l b_l^j = \delta_i^j$, where δ_i^j is the Kronecker symbol, it follows

$$\begin{aligned} \partial^t \left[\int \kappa_G(\phi) K \sqrt{g} d^2u \right] &= - \sum_{u,k} \int \partial^u [\kappa_G(\phi)] K g_{uk} \psi^k \sqrt{g} d^2u, \end{aligned}$$

which is the claim. □

Proposition D.11.

$$\nabla_a [\psi^z] = \sum_{b,k} g^{zb} \partial_b \vec{X} \cdot \partial_a [\partial_k \vec{X} \psi^k], \quad (\text{D.1})$$

Proof: It holds that

$$\begin{aligned} & \sum_{b,k} g^{zb} \partial_b \vec{X} \cdot \partial_a [\partial_k \vec{X} \psi^k] \\ &= \sum_k \frac{1}{2} \sum_b g^{zb} \left\{ \partial_k [g_{ba}] + \partial_a [g_{bk}] - \partial_b [g_{ak}] \right\} \psi^k + \partial_a [\psi^z]. \end{aligned}$$

Using the definition of the Christoffel symbol, we obtain that

$$\sum_{b,k} g^{zb} \partial_b \vec{X} \cdot \partial_a [\partial_k \vec{X} \psi^k] = \partial_a [\psi^z] + \sum_k \Gamma_{ak}^z \psi^k = \nabla_a [\psi^z],$$

which was the claim. In particular, we obtain $\sum_b g^{zb} \partial_b \vec{X} \cdot \partial_a [\partial_k \vec{X}] = \Gamma_{ak}^z$. \square

Proposition D.12.

$$\nabla_b [\psi_a] = \sum_k \partial_a \vec{X} \cdot \partial_b [\partial_k \vec{X} \psi^k]. \quad (\text{D.2})$$

Proof: It holds that

$$\begin{aligned} \nabla_b [\psi_a] &= \sum_l g_{la} \nabla_b [\psi^l] = \sum_l g_{la} \sum_{u,k} g^{ul} \partial_u \vec{X} \cdot \partial_b [\partial_k \vec{X} \psi^k] \\ &= \sum_{u,k} \delta_a^u \partial_u \vec{X} \cdot \partial_b [\partial_k \vec{X} \psi^k] = \sum_k \partial_a \vec{X} \cdot \partial_b [\partial_k \vec{X} \psi^k], \end{aligned}$$

which was the claim. \square

Lemma D.13.

$$\frac{\delta^k [F_3]}{\delta \vec{X}} = \xi^2 \sum_u \nabla_u [\partial^k [\phi] \partial^u [\phi]] - \partial^k \left[\frac{\xi^2}{2} (\nabla^\Gamma [\phi])^2 + f(\phi) \right].$$

Proof: Using the chain rule it follows that

$$\begin{aligned} & \delta^t \left[\int \left\{ \frac{\xi^2}{2} (\nabla^\Gamma [\phi])^2 + f(\phi) \right\} \sqrt{g} d^2 u \right] \\ &= \int \left\{ \frac{\xi^2}{2} \delta^t [(\nabla^\Gamma [\phi])^2] \sqrt{g} d^2 u + \int \left\{ \frac{\xi^2}{2} (\nabla^\Gamma [\phi])^2 + f(\phi) \right\} \delta^t [\sqrt{g}] d^2 u. \right. \end{aligned} \quad (\text{D.3})$$

Considering the first term of equation (D.3) results in

$$\int \frac{\xi^2}{2} \delta^t [(\nabla^\Gamma [\phi])^2] \sqrt{g} d^2 u = \frac{\xi^2}{2} \int \delta^t \left[\sum_{i,j} g^{ij} \partial_i [\phi] \partial_j [\phi] \right] \sqrt{g} d^2 u.$$

From [126] it follows that $\delta^t [g^{ij}] = -\nabla^i [\psi^j] - \nabla^j [\psi^i]$. Thus, it follows that

$$\int \frac{\xi^2}{2} \delta^t [(\nabla^\Gamma [\phi])^2] \sqrt{g} d^2 u = -\xi^2 \sum_{i,j,u} \int g^{iu} \nabla_u [\psi^j] \partial_i [\phi] \partial_j [\phi] \sqrt{g} d^2 u.$$

Proposition D.11 yields

$$\begin{aligned}
& \int \frac{\xi^2}{2} \delta^t [(\nabla^\Gamma [\phi])^2] \sqrt{g} d^2 u \\
&= -\xi^2 \sum_{i,j,u} \int g^{iu} \left(\sum_{b,k} g^{jb} \partial_b \vec{X} \cdot \partial_u [\partial_k \vec{X} \psi^k] \right) \partial_i [\phi] \partial_j [\phi] \sqrt{g} d^2 u \\
&= -\xi^2 \sum_{u,b,k} \int \partial^u [\phi] \partial^b [\phi] \partial_b \vec{X} \cdot \partial_u [\partial_k \vec{X} \psi^k] \sqrt{g} d^2 u.
\end{aligned}$$

Applying Green's formula provides

$$\begin{aligned}
& \int \frac{\xi^2}{2} \delta^t [(\nabla^\Gamma [\phi])^2] \sqrt{g} d^2 u \\
&= \xi^2 \sum_{u,b,k} \int \partial_u [\partial^u [\phi] \partial^b [\phi] \partial_b \vec{X} \sqrt{g}] \cdot \partial_k \vec{X} \psi^k d^2 u \\
&= \xi^2 \sum_{u,b,k} \int \left\{ \partial_u [\partial^b [\phi] \partial_b \vec{X}] \cdot \partial_k \vec{X} \partial^u [\phi] \sqrt{g} \psi^k + \partial_u [\sqrt{g} \partial^u [\phi]] g_{bk} \partial^b [\phi] \psi^k \right\} d^2 u.
\end{aligned}$$

Thus, it holds that

$$\begin{aligned}
& \int \frac{\xi^2}{2} \delta^t [(\nabla^\Gamma [\phi])^2] \sqrt{g} d^2 u \\
&= \xi^2 \sum_{u,b,k} \int \left\{ \partial_u [\partial^b [\phi] \partial_b \vec{X}] \cdot \partial_k \vec{X} \partial^u [\phi] \sqrt{g} \psi^k + \partial_u [\sqrt{g} \partial^u [\phi]] g_{bk} \partial^b [\phi] \psi^k \right\} d^2 u.
\end{aligned} \tag{D.4}$$

Applying Proposition D.11 to the first term on the right-hand side of equation (D.4), we obtain

$$\begin{aligned}
& \xi^2 \sum_{u,b,k} \int \partial_u [\partial^b [\phi] \partial_b \vec{X}] \cdot \partial_k \vec{X} \partial^u [\phi] \psi^k \sqrt{g} d^2 u \\
&= \xi^2 \sum_{u,b,k} \int \nabla_u [\partial^b \phi] \partial^u [\phi] g_{bk} \psi^k \sqrt{g} d^2 u.
\end{aligned}$$

For the second term of (D.4) it holds that

$$\begin{aligned}
& \xi^2 \sum_{u,b,k} \int \partial_u [\sqrt{g} \partial^u [\phi]] g_{bk} \partial^b [\phi] \psi^k d^2 u \\
&= \xi^2 \sum_{u,b,k} \int \left\{ \partial_u [\partial^u [\phi]] \sqrt{g} + \partial_u [\sqrt{g}] \partial^u [\phi] \right\} \partial^b [\phi] g_{bk} \psi^k d^2 u.
\end{aligned}$$

Applying the chain rule to the determinant results in [163]

$$\begin{aligned}
& \xi^2 \sum_{u,b,k} \int \partial_u [\partial^b[\phi] \partial_b \vec{X}] \cdot \partial_k \vec{X} \partial^u[\phi] \psi^k \sqrt{g} d^2u \\
&= \xi^2 \sum_{u,b,k} \int \partial_u [\partial^u \phi] \partial^b[\phi] g_{bk} \psi^k \sqrt{g} d^2u \\
&\quad + \xi^2 \sum_{u,b,k,i,j} \int g^{ij} \partial_u [\partial_i \vec{X}] \cdot \partial_j \vec{X} \partial^b[\phi] g_{bk} \psi^k \sqrt{g} d^2u.
\end{aligned}$$

Using the alternative definition of the Christoffel symbol $\sum_b g^{zb} \partial_b \vec{X} \cdot \partial_a [\partial_k \vec{X}] = \Gamma_{ak}^z$ (see the proof of Proposition D.11), we obtain

$$\begin{aligned}
& \xi^2 \sum_{u,b,k} \int \partial_u [\partial^b[\phi] \partial_b \vec{X}] \cdot \partial_k \vec{X} \partial^u[\phi] \psi^k \sqrt{g} d^2u \\
&= \xi^2 \sum_{u,b,k} \int \partial_u [\partial^u \phi] \partial^b[\phi] g_{bk} \psi^k \sqrt{g} d^2u \\
&\quad + \xi^2 \sum_{u,b,k,i} \int \Gamma_{ui}^i \partial^u[\phi] \partial^b[\phi] g_{bk} \psi^k \sqrt{g} d^2u.
\end{aligned}$$

Transposition of the indices $u \leftrightarrow i$, use of $\Gamma_{ui}^i = \Gamma_{iu}^i$, and the definition of the covariant derivative lead to [163]

$$\begin{aligned}
& \xi^2 \sum_{u,b,k} \int \partial_u [\partial^b[\phi] \partial_b \vec{X}] \cdot \partial_k \vec{X} \partial^u[\phi] \psi^k \sqrt{g} d^2u \\
&= \xi^2 \sum_{u,b,k} \int \nabla_u [\partial^u \phi] \partial^b[\phi] g_{bk} \psi^k \sqrt{g} d^2u.
\end{aligned}$$

Reformulating the terms of Equation (D.4), we obtain that

$$\begin{aligned}
\int \frac{\xi^2}{2} \partial^t [(\nabla^\Gamma[\phi])^2] \sqrt{g} d^2u &= \xi^2 \sum_{u,b,k} \int \nabla_u [\partial^b[\phi]] \partial^u[\phi] \psi^k g_{bk} \sqrt{g} d^2u \\
&\quad + \xi^2 \sum_{u,b,k} \int \nabla_u [\partial^u[\phi]] \partial^b[\phi] g_{bk} \psi^k \sqrt{g} d^2u.
\end{aligned} \tag{D.5}$$

Furthermore, substituting in equation (D.3) provides

$$\begin{aligned}
& \delta^t \left[\int \left\{ \frac{\xi^2}{2} (\nabla^\Gamma[\phi])^2 + f(\phi) \right\} \sqrt{g} d^2u \right] \\
&= \xi^2 \sum_{u,b,k} \int \left\{ \nabla_u [\partial^b[\phi]] \partial^u[\phi] + \nabla_u [\partial^u[\phi]] \partial^b[\phi] \right\} g_{bk} \psi^k \sqrt{g} d^2u \\
&\quad + \int \left\{ \frac{\xi^2}{2} (\nabla^\Gamma[\phi])^2 + f(\phi) \right\} \delta^t [\sqrt{g}] d^2u.
\end{aligned}$$

Finally, using the chain rule for covariant derivatives we obtain that

$$\begin{aligned} \delta^t \left[\int \left\{ \frac{\xi^2}{2} (\nabla^\Gamma[\phi])^2 + f(\phi) \right\} \sqrt{g} d^2u \right] \\ = \xi^2 \sum_{u,b,k} \int \nabla_u [\partial^b[\phi] \partial^u[\phi]] g_{bk} \psi^k \sqrt{g} d^2u \\ - \sum_{u,k} \int \partial^u \left[\frac{\xi^2}{2} (\nabla^\Gamma[\phi])^2 + f(\phi) \right] g_{uk} \psi^k \sqrt{g} d^2u, \end{aligned}$$

leading to the claim. □

Lemma D.14. (c.f. [84])

$$\begin{aligned} d_t[\phi(\vec{u}, t)] = L_\phi \Delta^\Gamma \left[\frac{1}{2} \kappa'(\phi) (H - H_0(\phi))^2 + \kappa(\phi) (H - H_0(\phi)) H'_0(\phi) \right. \\ \left. + \kappa'_G(\phi) K - \xi^2 \Delta^\Gamma \phi + f'(\phi) \right]. \end{aligned}$$

Proof:

$$\begin{aligned} \delta^\phi[F_1] &= \frac{1}{2} \int \delta^\phi[\kappa(\phi)] (H - H_0(\phi))^2 ds - \int \kappa(\phi) (H - H_0(\phi)) \delta^\phi[H_0(\phi)] ds \\ &= \frac{1}{2} \int \kappa'(\phi) (H - H_0(\phi))^2 \psi ds + \int \kappa(\phi) (H - H_0(\phi)) H'_0(\phi) \psi ds. \end{aligned}$$

Thus, it follows that

$$\frac{\delta F_1}{\delta \phi(\vec{u})} = \frac{1}{2} \kappa'(\phi) (H - H_0(\phi))^2 - \kappa(\phi) (H - H_0(\phi)) H'_0(\phi).$$

Furthermore, we have

$$\delta^\phi[F_2] = \int \delta^\phi[\kappa_G(\phi)] K ds = \int \kappa'_G(\phi) K \psi ds$$

and consequently

$$\frac{\delta[F_2]}{\delta \phi(\vec{u})} = \kappa'_G(\phi) K.$$

The third energy term reads

$$\delta^\phi[F_3] = \xi^2 \int (\nabla^\Gamma[\phi]) (\nabla^\Gamma[\psi]) ds + \int f'(\phi) \psi ds.$$

Then, using Green's formula we obtain that

$$\delta^\phi[F_3] = -\xi^2 \int \Delta^\Gamma[\phi] \psi ds + \int f'(\phi) \psi ds.$$

Finally, it holds that

$$\frac{\delta F_3}{\delta \phi(\vec{u})} = -\xi^2 \Delta^\Gamma [\phi] + f'(\phi),$$

and since $\delta F_4/\delta \phi = 0$, we obtain

$$\begin{aligned} \frac{\delta F}{\delta \phi(\vec{u})} &= \frac{1}{2} \kappa'(\phi)(H - H_0(\phi))^2 - \kappa(\phi)(H - H_0(\phi))H_0'(\phi) \\ &\quad + \kappa'_G(\phi)K - \xi^2 \Delta^\Gamma [\phi] + f'(\phi). \end{aligned}$$

□

BIBLIOGRAPHY

BIBLIOGRAPHY

- [1] T. Adachi, H. Takahashi, K. Ohki, and I. Hatta. Interdigitated structure of phospholipid-alcohol systems studied by X-ray diffraction. *Biophys J*, 68:1850–1855, 1995.
- [2] A. Agrawal and D. J. Steigmann. Boundary-value problems in the theory of lipid membranes. *Cont Mech Thermodyn*, 21:57–82, 2009.
- [3] N. J. Agrawal, J. Nukpezah, and R. Radhakrishnan. Minimal mesoscale model for protein-mediated vesiculation in Clathrin-dependent endocytosis. *PLoS Comput Biol*, 6:e1000926, 2010.
- [4] B. Alberts, D. Bray, and J. Lewis. *Molecular biology of the cell*. Garland Publishing, Inc., 2006.
- [5] J.-M. Allain and M. B. Amar. Budding and fission of a multiphase vesicle. *Eur Phys J E Soft Matter*, 20:409–420, 2006.
- [6] J.-M. Allain, C. Storm, A. Roux, M. B. Amar, and J.-F. Joanny. Fission of a multiphase membrane tube. *Phys Rev Lett*, 93:158104, 2004.
- [7] D. W. Allender and M. Schick. Phase separation in bilayer lipid membranes: effects on the inner leaf due to coupling to the outer leaf. *Biophys J*, 91:2928–2935, 2006.
- [8] D. Andelman, T. Kawakatsu, and K. Kawasaki. Equilibrium shape of two-component unilamellar membranes and vesicles. *Europhys Lett*, 19:57–62, 1992.
- [9] O. S. Andersen and R. E. Koeppe. Bilayer thickness and membrane protein function: an energetic perspective. *Annu Rev Biophys Biomol Struct*, 36:107–130, 2007.
- [10] N. L. Anderson and N. G. Anderson. Proteome and proteomics: new technologies, new concepts, and new words. *Electrophoresis*, 19:1853–1861, 1998.
- [11] G. S. Ayton, J. L. McWhirter, P. McMurtry, and G. A. Voth. Coupling field theory with continuum mechanics: a simulation of domain formation in giant unilamellar vesicles. *Biophys J*, 88:3855–3869, 2005.

- [12] K. Bacia, P. Schwille, and T. Kurzchalia. Sterol structure determines the separation of phases and the curvature of the liquid-ordered phase in model membranes. *PNAS*, 102:3272–3277, 2005.
- [13] R. Baierlein. The elusive chemical potential. *American J Phys*, 69:423–434, 2001.
- [14] J. Barrett, H. Garcke, and R. Nürnberg. On the parametric finite element approximation of evolving hypersurfaces in \mathbb{R}^3 . *J Comp Phys*, 227:4281–4307, 2008.
- [15] J. Barrett, H. Garcke, and R. Nürnberg. Parametric approximation of Willmore flow and related geometric evolution equations. *SIAM J Sci Comp*, 31:225–253, 2008.
- [16] R. Bartenschlager and V. Lohmann. Replication of hepatitis C virus. *J Gen Virol*, 81:1631–1648, 2000.
- [17] T. Baumgart, S. Das, W. W. Webb, and J. T. Jenkins. Membrane elasticity in giant vesicles with fluid phase coexistence. *Biophys J*, 89:1067–1080, 2005.
- [18] T. Baumgart, S. T. Hess, and W. W. Webb. Imaging coexisting fluid domains in biomembrane models coupling curvature and line tension. *Nature*, 425:821–824, 2003.
- [19] R. Becker, M. Braack, T. Dunne, D. Meidner, T. Richter, and B. Vexler. Gascoigne 3D- a finite element toolbox (<http://www.gascoigne.uni-hd.de>). 2005.
- [20] S. V. Bennun, M. L. Longo, and R. Faller. Molecular-scale structure in fluid-gel patterned bilayers: stability of interfaces and transmembrane distribution. *Langmuir*, 23:12465–12468, 2007.
- [21] K. Berndl, J. Käs, R. Lipowsky, and E. Sackmann. Shape transformations of giant vesicles: extreme sensitivity to bilayer asymmetry. *Europhys Lett*, 13:659–664, 1990.
- [22] M. Berström. Derivation of expressions for the spontaneous curvature, mean and Gaussian bending constants of thermodynamically open surfactant monolayers and bilayers. *J Chem Phys*, 118:1440–1452, 2003.
- [23] L. C. Bickford, E. Mossessova, and J. Goldberg. A structural view of the COPII vesicle coat. *Curr Opin Struct Biol*, 14:147–153, 2004.
- [24] J. Bigay, P. Gounon, S. Robineau, and B. Antonny. Lipid packing sensed by ArfGAP1 couples COPI coat disassembly to membrane bilayer curvature. *Nature*, 426:563–566, 2003.
- [25] H. R. Bode. Head regeneration in *Hydra*. *Dev Dyn*, 226:225–236, 2003.

- [26] J. S. Bonifacino and J. Lippincott-Schwartz. Coat proteins: shaping membrane transport. *Nat Rev Mol Cell Biol*, 4:409–414, 2003.
- [27] A. Bonito, R. Nochetto, and M. S. Pauletti. Parametric FEM for geometric biomembranes. *J Comp Phys*, 221:31713188, 2010.
- [28] B. Bozic, V. Kralj-Iglic, and S. Svetina. Coupling between vesicle shape and lateral distribution of mobile membrane inclusions. *Phys Rev E Stat Nonlin Soft Matter Phys*, 73:041915, 2006.
- [29] G. Brannigan and F. L. H. Brown. A consistent model for thermal fluctuations and protein-induced deformations in lipid bilayers. *Biophys J*, 90:1501–1520, 2006.
- [30] G. Brannigan and F. L. H. Brown. Contributions of Gaussian curvature and nonconstant lipid volume to protein deformation of lipid bilayers. *Biophys J*, 92:864–876, 2007.
- [31] A. J. Bray. Theory of phase-ordering kinetics. *Adv in Phys*, 43:357–459, 1994.
- [32] M. S. Bretscher. Asymmetrical lipid bilayer structure for biological membranes. *Nat New Biol*, 236:11–12, 1972.
- [33] F. Brezzi and M. Fortin. *Mixed and hybrid finite element methods*. New York, 1991.
- [34] E. Brouzes and E. Farge. Interplay of mechanical deformation and patterned gene expression in developing embryos. *Curr Opin Genet Dev*, 14:367–374, 2004.
- [35] F. L. H. Brown. Elastic modeling of biomembranes and lipid bilayers. *Annu Rev Phys Chem*, 59:685–712, 2008.
- [36] F. L. H. Brown. Continuum simulations of biomembrane dynamics and the importance of hydrodynamic effects. *Q Rev Biophys*, 44:1–42, 2011.
- [37] R. J. Bruckner, S. S. Mansy, A. Ricardo, L. Mahadevan, and J. W. Szostak. Flip-flop-induced relaxation of bending energy: implications for membrane remodeling. *Biophys J*, 97:3113–3122, 2009.
- [38] J. Cahn and J. Hilliard. Free energy of a nonuniform system: Interfacial free energy. *J Chem Phys*, 28:258–267, 1958.
- [39] F. Campelo and A. Hernandez-Machado. Model for curvature-driven pearling instability in membranes. *Phys Rev Lett*, 99:088101, 2007.
- [40] N. A. Campbell. *Biologie*. Spektrum Akademischer Verlag GmbH Heidelberg, 1997.

- [41] R. Capovilla and J. Guven. Stresses in lipid membranes. *J Phys A: Math Gen*, 35:6233–6247, 2002.
- [42] E. Chacon and A. Somoza. Elastic constants from a microscopic model of bilayer membrane. *J Chem Phys*, 109:2371–2379, 1998.
- [43] Y.-H. M. Chan and S. G. Boxer. Model membrane systems and their applications. *Curr Opin Chem Biol*, 11:581–587, 2007.
- [44] D. Chandler. Interfaces and the driving force of hydrophobic assembly. *Nature*, 437:640–647, 2005.
- [45] C. M. Chen. Theory for the bending anisotropy of lipid membranes and tubule formation. *Phys Rev E Stat Phys Plasmas Fluids Relat Interdiscip Topics*, 59:6192–6195, 1999.
- [46] C. M. Chen. Theory for the bending rigidity of protein-coated lipid membranes. *Physica A*, 281:41–50, 2000.
- [47] C. M. Chen, P. G. Higgs, and F. C. MacKintosh. Theory of fission for two-component lipid vesicles. *Phys Rev Lett*, 79:1579–1582, 1997.
- [48] X.-B. Chen, H.-J. Shi, and L.-S. Niu. Numerical study of the phase separation in binary lipid membrane containing protein inclusions under stationary shear flow. *J Biomech*, 42:603–613, 2009.
- [49] P. Ciarlet. *Mathematical elasticity, Vol II: Theory of Plates, Series "Studies in Mathematics and its Applications"*. North Holland, Amsterdam, 1997.
- [50] D. Codazzi. Sulle coordinate curvilinee d’una superficie e dello spazio. *Annali di Matematica Pura ed Applicata*, 2:101–119, 1868.
- [51] M. D. Collins. Interleaflet coupling mechanisms in bilayers of lipids and cholesterol. *Biophys J*, 94:L32–L34, 2008.
- [52] M. D. Collins and S. L. Keller. Tuning lipid mixtures to induce or suppress domain formation across leaflets of unsupported asymmetric bilayers. *PNAS*, 105:124–128, 2008.
- [53] V. Conte, J. J. Muoz, and M. Miodownik. A 3D finite element model of ventral furrow invagination in the *Drosophila melanogaster* embryo. *J Mech Behav Biomed Mater*, 1:188–198, 2008.
- [54] I. R. Cooke and M. Deserno. Solvent-free model for self-assembling fluid bilayer membranes: stabilization of the fluid phase based on broad attractive tail potentials. *J Chem Phys*, 123:224710, 2005.
- [55] I. R. Cooke and M. Deserno. Coupling between lipid shape and membrane curvature. *Biophys J*, 91:487–495, 2006.

- [56] I. R. Cooke, K. Kremer, and M. Deserno. Tunable generic model for fluid bilayer membranes. *Phys Rev E Stat Nonlin Soft Matter Phys*, 72:011506, 2005.
- [57] G. C. Cruywagen and J. D. Murray. On a tissue interaction model for skin pattern formation. *J Nonl Sci*, 2:217–240, 1992.
- [58] F. W. Cummings. On surface geometry coupled to morphogen. *J Theor Biol*, 137:215–219, 1989.
- [59] F. W. Cummings. The interaction of surface geometry with morphogens. *J Theor Biol*, 212:303–313, 2001.
- [60] S. Das, J. Jenkins, and T. Baumgart. Neck geometry and shape transitions in vesicles with co-existing fluid phases: Role of Gaussian curvature stiffness vs. spontaneous curvature. *EPL*, 86:1–6, 2009.
- [61] F. David. *Statistical Mechanics of Membranes and Surfaces*. World Scientific Press, 2004.
- [62] F. J.-M. de Meyer, J. M. Rodgers, T. F. Willems, and B. Smit. Molecular simulation of the effect of cholesterol on lipid-mediated protein-protein interactions. *Biophys J*, 99:3629–3638, 2010.
- [63] F. J.-M. de Meyer, M. Venturoli, and B. Smit. Molecular simulations of lipid-mediated protein-protein interactions. *Biophys J*, 95(4):1851–1865, Aug 2008.
- [64] K. Deckelnick, G. Dziuk, and C. Elliott. Computation of geometric partial differential equations and mean curvature flow. *Acta Numerica*, 14:139–232, 2005.
- [65] J. Derganc. Curvature-driven lateral segregation of membrane constituents in golgi cisternae. *Phys Biol*, 4:317–324, 2007.
- [66] N. Desprat, W. Supatto, P.-A. Pouille, E. Beaurepaire, and E. Farge. Tissue deformation modulates twist expression to determine anterior midgut differentiation in *Drosophila* embryos. *Dev Cell*, 15:470–477, 2008.
- [67] P. F. Devaux. Is lipid translocation involved during endo- and exocytosis? *Biochimie*, 82:497–509, 2000.
- [68] H. G. Döbereiner. *Soft-Matter Characterization: Optical Microscopy of Fluctuating Giant Vesicles and Motile Cells*. Springer Verlag, 2008.
- [69] H. G. Döbereiner, J. Käs, D. Noppl, I. Sprenger, and E. Sackmann. Budding and fission of vesicles. *Biophys J*, 65:1396–1403, 1993.
- [70] M. Dogterom and G. Koenderink. Cell-membrane mechanics: Vesicles in and tubes out. *Nat Mater*, 10:561–562, 2011.

- [71] N. Dong, S. Hui-Ji, Y. Ya-Jun, and N. Li-Sha. Dynamics of phase separation in mixed lipid membranes between two bounding walls. *Physica B*, 388:159–166, 2007.
- [72] N. Dong, S. Huiji, Y. Yajun, and N. Lisha. Stability of biphasic vesicles with membrane embedded proteins. *J Biomech*, 40:1512–1517, 2007.
- [73] N. Dong, Y. Yajun, and S. Huiji. Equilibrium shape equation and geometrically permissible condition for two-component lipid bilayer vesicles. *J Biol Phys*, 31:135–143, 2005.
- [74] G. Drin and B. Antonny. Amphipathic helices and membrane curvature. *FEBS Lett*, 584:1840–1847, 2010.
- [75] Q. Du, C. Liu, R. Ryham, and X. Wang. Modeling the spontaneous curvature effects in static cell membrane deformations by a phase field formulation. *Comm Pure Appl Anal*, 4:537–548, 2005.
- [76] Q. Du, C. Liu, and X. Wang. Simulating the deformation of vesicle membranes under elastic bending energy in three dimensions. *J Comp Phys*, 212:757–777, 2006.
- [77] D. Duque, X.-J. Li, K. Katsov, and M. Schick. Molecular theory of hydrophobic mismatch between lipids and peptides. *J Chem Phys*, 116:10478, 2002.
- [78] G. Dziuk, E. Kuwert, and R. Schätzle. Evolution of elastic curves in \mathbb{R}^n : Existence and computation. *SIAM J Math Anal*, 33:1228–1245, 2002.
- [79] C. Eilks and C. M. Elliott. Numerical simulation of dealloying by surface dissolution via the evolving surface finite element method. *J Comp Phys*, 227:9727–9741, 2008.
- [80] C. Elliott, D. French, and F. Milner. A second order splitting method for the Cahn-Hilliard equation. *Num Math*, 54:575–590, 1989.
- [81] C. Elliott and H. Garcke. On the Cahn-Hilliard equation with degenerate mobility. *SIAM J Math Anal*, 27:404–423, 1996.
- [82] C. Elliott and Z. Songmu. On the Cahn-Hilliard equation. *Arch Rat Mech Anal*, 96:339–357, 1986.
- [83] C. Elliott and B. Stinner. Modeling and computation of two phase geometric biomembranes using surface finite elements. *J Comp Phys*, 229:6585–6612, 2010.
- [84] C. M. Elliott and B. Stinner. A surface phase field model for two-phase biological membranes. *SIAM J Appl Math*, 70:2904–2928, 2010.
- [85] E. L. Elson, E. Fried, J. E. Dolbow, and G. M. Genin. Phase separation in biological membranes: Integration of theory and experiment. *Annu Rev Biophys*, 39:207–226, 2010.

- [86] H. Engelhardt, H. P. Duwe, and E. Sackmann. Bilayer bending elasticity measured by fourier analysis of thermally excited surface undulations of flaccid vesicles. *J Physique Lett*, 46:395–400, 1985.
- [87] E. A. Evans. Bending resistance and chemically induced moments in membrane bilayers. *Biophys J*, 14:923–931, 1974.
- [88] E. Farge. Mechanotransduction in development. *Curr Top Dev Biol*, 95:243–265, 2011.
- [89] K. Farsad and P. D. Camilli. Mechanisms of membrane deformation. *Curr Opin Cell Biol*, 15:372–381, 2003.
- [90] D. R. Fattal and A. Ben-Shaul. A molecular model for lipid-protein interaction in membranes: the role of hydrophobic mismatch. *Biophys J*, 65:1795–1809, 1993.
- [91] G. W. Feigenson. Phase boundaries and biological membranes. *Annu Rev Biophys Biomol Struct*, 36:63–77, 2007.
- [92] S. E. Feller. Molecular dynamics simulations of lipid bilayers. *Cur Op Coll Interf Sci*, 5:217–223, 2000.
- [93] G. Foltin. Dynamics of incompressible fluid membranes. *Phys Rev E Stat Phys Plasmas Fluids Relat Interdiscip Topics*, 49:5243–5248, 1994.
- [94] V. A. Frolov, V. A. Lizunov, A. Y. Dunina-Barkovskaya, A. V. Samsonov, and J. Zimmerberg. Shape bistability of a membrane neck: a toggle switch to control vesicle content release. *PNAS*, 100:8698–8703, 2003.
- [95] V. A. J. Frolov, Y. A. Chizmadzhev, F. S. Cohen, and J. Zimmerberg. "entropic traps" in the kinetics of phase separation in multicomponent membranes stabilize nanodomains. *Biophys J*, 91:189–205, 2006.
- [96] A. J. Garcia-Saez, S. Chiantia, and P. Schwille. Effect of line tension on the lateral organization of lipid membranes. *J Biol Chem*, 282:33537–33544, 2007.
- [97] R. Gennis. *Biomembranes: Molecular Structure and Function*. Springer-Verlag, New York, 1989.
- [98] T. Gregor, E. F. Wieschaus, A. P. McGregor, W. Bialek, and D. W. Tank. Stability and nuclear dynamics of the bicoid morphogen gradient. *Cell*, 130:141–152, 2007.
- [99] G. Guigas, D. Morozova, and M. Weiss. Exploring membrane and protein dynamics with dissipative particle dynamics. *Adv Protein Chem Struct Biol*, 85:143–182, 2011.

- [100] K. Guo and J. Li. Exploration of the shapes of double-walled vesicles with a confined inner membrane. *J Phys Condens Matter*, 23:285103, 2011.
- [101] P. L. Hansen, L. Miao, and J. H. Ipsen. Fluid lipid bilayers: Intermonolayer coupling and its thermodynamic manifestations. *Phys Rev E*, 58:2311–2324, 1998.
- [102] F. M. Harold. From morphogens to morphogenesis. *Microbiology*, 141:2765–2778, 1995.
- [103] M. P. Harris, S. Williamson, J. F. Fallon, H. Meinhardt, and R. O. Prum. Molecular evidence for an activator-inhibitor mechanism in development of embryonic feather branching. *PNAS*, 102:11734–11739, 2005.
- [104] D. Hartmann. *Multiscale Modelling, Analysis, and Simulation in Mechanobiology*. PhD thesis, Heidelberg University, 2007.
- [105] D. Hartmann. A multiscale model for red blood cell mechanics. *Biomech Model Mechanobiol*, 9:1–17, 2010.
- [106] X. He and J. D. Axelrod. A WNTer wonderland in snowbird. *Development*, 133:2597–2603, 2006.
- [107] M. Heinrich, A. Tian, C. Esposito, and T. Baumgart. Dynamic sorting of lipids and proteins in membrane tubes with a moving phase boundary. *PNAS*, 107:7208–7213, 2010.
- [108] W. Helfrich. Elastic properties of lipid bilayers: theory and possible experiments. *Z Naturforsch [C]*, 28:693–703, 1973.
- [109] J. Henriksen, A. C. Rowat, and J. H. Ipsen. Vesicle fluctuation analysis of the effects of sterols on membrane bending rigidity. *Eur Biophys J*, 33:732–741, 2004.
- [110] J. M. Holopainen, M. I. Angelova, and P. K. Kinnunen. Vectorial budding of vesicles by asymmetrical enzymatic formation of ceramide in giant liposomes. *Biophys J*, 78:830–838, 2000.
- [111] T. Holstein. Unpublished data (2011).
- [112] B. Hong, F. Qiu, H. Zhang, and Y. Yang. Budding dynamics of individual domains in multicomponent membranes simulated by N-varied dissipative particle dynamics. *J Phys Chem B*, 111:5837–5849, 2007.
- [113] U. Hornung, W. Jäger, and A. Mikelic. Reactive transport through an array of cells with semi-permeable membranes. *Math Model Num Anal*, 28:59–94, 1994.
- [114] J. Hu, Y. Shibata, C. Voss, T. Shemesh, Z. Li, M. Coughlin, M. M. Kozlov, T. A. Rapoport, and W. A. Prinz. Membrane proteins of the endoplasmic reticulum induce high-curvature tubules. *Science*, 319:1247–1250, 2008.

- [115] L. Hufnagel, A. A. Teleman, H. Rouault, S. M. Cohen, and B. I. Shraiman. On the mechanism of wing size determination in fly development. *PNAS*, 104:3835–3840, 2007.
- [116] J. H. Hurley, E. Boura, L.-A. Carlson, and B. Rozycki. Membrane budding. *Cell*, 143:875–887, 2010.
- [117] G. Illya, R. Lipowsky, and J. C. Shillcock. Two-component membrane material properties and domain formation from dissipative particle dynamics. *J Chem Phys*, 125:114710, 2006.
- [118] V. P. Ivanova, I. M. Makarov, T. E. Schäffer, and T. Heimburg. Analyzing heat capacity profiles of peptide-containing membranes: cluster formation of gramicidin A. *Biophys J*, 84:2427–2439, 2003.
- [119] J. T. Jenkins. Static equilibrium configurations of a model red blood cell. *J Math Biol*, 4:149–169, 1977.
- [120] Y. Jiang, T. Lookman, and A. Saxena. Phase separation and shape deformation of two-phase membranes. *Phys Rev E Stat Phys Plasmas Fluids Relat Interdiscip Topics*, 61:R57–R60, 2000.
- [121] G. Job and F. Herrmann. Chemical potential - a quantity in search of recognition. *Europ J Phys*, 27:353–371, 2006.
- [122] J. Juhasz, F. J. Sharom, and J. H. Davis. Quantitative characterization of coexisting phases in DOPC/DPPC/cholesterol mixtures: comparing confocal fluorescence microscopy and deuterium nuclear magnetic resonance. *Biochim Biophys Acta*, 1788:2541–2552, 2009.
- [123] F. Jülicher and R. Lipowsky. Domain-induced budding of vesicles. *Phys Rev Lett*, 70:2964–2967, 1993.
- [124] F. Jülicher and R. Lipowsky. Shape transformations of vesicles with intramembrane domains. *Phys Rev E Stat Phys Plasmas Fluids Relat Interdiscip Topics*, 53:2670–2683, 1996.
- [125] M. Kamal, D. Mills, M. Grzybek, and J. Howard. Measurement of the membrane curvature preference of phospholipids reveals only weak coupling between lipid shape and leaflet curvature. *PNAS*, 106:22245–22250, 2009.
- [126] Y. Kentaro. Infinitesimal variations of submanifolds. *Kodai Math J*, 1:33–44, 1978.
- [127] J. A. Killian. Hydrophobic mismatch between proteins and lipids in membranes. *Biochim Biophys Acta*, 1376:401–415, 1998.
- [128] S. Komura and D. Andelman. Adhesion-induced lateral phase separation in membranes. *Eur Phys J E*, 3:259–271, 2000.

- [129] Y. Kozlovsky and M. M. Kozlov. Membrane fission: model for intermediate structures. *Biophys J*, 85:85–96, 2003.
- [130] V. Kralj-Iglic, A. Iglic, G. Gomiscek, F. Sevsek, V. Arrigler, and H. Hägerstrand. Microtubes and nanotubes of a phospholipid bilayer membrane. *Journal Phys A*, 35:1533–1549, 2002.
- [131] J. Kühnle. Structure formation and self-organization in the early secretory pathway. *Dissertation, Universität Heidelberg*, 2011.
- [132] P. B. S. Kumar, G. Gompper, and R. Lipowsky. Budding dynamics of multi-component membranes. *Phys Rev Lett*, 86:3911–3914, 2001.
- [133] E. Kurtisovski, N. Taulier, R. Ober, M. Waks, and W. Urbach. Molecular origin of model membrane bending rigidity. *Phys Rev Lett*, 98:258103, 2007.
- [134] E. Kuwert and R. Schätzle. Gradient flow for the Willmore functional. *Comm Anal Geom*, 10:307–339, 2002.
- [135] D. Kwak. The sharp-interface limit of the Cahn-Hilliard system with elasticity. *Dissertation, Universität Regensburg*, 2008.
- [136] M. Laradji and P. B. S. Kumar. Domain growth, budding, and fission in phase-separating self-assembled fluid bilayers. *J Chem Phys*, 123:224902, 2005.
- [137] M. Laradji and P. B. S. Kumar. Anomalously slow domain growth in fluid membranes with asymmetric transbilayer lipid distribution. *Phys Rev E Stat Nonlin Soft Matter Phys*, 73:040901, 2006.
- [138] M. Laradji and O. Mouritsen. Elastic properties of surfactant monolayers at liquid-liquid interfaces: A molecular dynamics study. *J Chem Phys*, 112:8621–8630, 2000.
- [139] A. G. Lee. How lipids affect the activities of integral membrane proteins. *Biochim Biophys Acta*, 1666:62–87, 2004.
- [140] A. G. Lee. Lipid sorting: lipids do it on their own. *Curr Biol*, 15:R421–R423, 2005.
- [141] S. Leibler. Curvature instability in membranes. *J Physique*, 47:507–516, 1986.
- [142] M. Lenz, S. Morlot, and A. Roux. Mechanical requirements for membrane fission: common facts from various examples. *FEBS Lett*, 583:3839–3846, 2009.
- [143] B. A. Lewis and D. M. Engelman. Lipid bilayer thickness varies linearly with acyl chain length in fluid phosphatidylcholine vesicles. *J Mol Biol*, 166:211–217, 1983.
- [144] M. Lewis and J. Murray. Analysis of stable two-dimensional patterns in contractil cytogel. *J Nonlin Sci*, 1:289–311, 1991.

- [145] J. Li, H. Zhang, P. Tang, F. Qiu, and Y. Yang. A discrete, space variation model for studying the kinetics of shape deformation of vesicles coupled with phase separation. *Macromol Theo Sim*, 15:432–439, 2006.
- [146] L. Li, M. Lin, and F. Qui. Lateral separation and budding of giant vesicles. *Acta chimica sinica*, 63:1375–1378, 2005.
- [147] X. Li, I. V. Pivkin, H. Liang, and G. E. Karniadakis. Shape transformations of membrane vesicles from amphiphilic triblock copolymers: a dissipative particle dynamics simulation study. *Macromolecule*, 42:3195–3200, 2009.
- [148] Q. Liang and Y.-Q. Ma. Curvature-induced lateral organization in mixed lipid bilayers supported on a corrugated substrate. *J Phys Chem B*, 113:8049–8055, 2009.
- [149] G. Lim, M. Wortis, and R. Mukhopadhyay. Stomatocyte-discocyte-echinocyte sequence of the human red blood cell: evidence for the bilayer- couple hypothesis from membrane mechanics. *PNAS*, 99:16766–16769, 2002.
- [150] L. Lipowsky. Budding of membranes induced by intramembrane domains. *J Phys France*, 2:1825–1840, 1992.
- [151] R. Lipowsky. The conformation of membranes. *Nature*, 349(6309):475–481, 1991.
- [152] R. Lipowsky. Domain-induced budding of fluid membranes. *Biophys J*, 64:1133–1138, 1993.
- [153] R. Lipowsky and S. Grothaus. Hydration vs. protrusion forces between between lipid bilayers. *Europhys. Lett.*, 23:599–604, 1993.
- [154] J. Liu, Y. Sun, D. G. Drubin, and G. F. Oster. The mechanochemistry of endocytosis. *PLoS Biol*, 7:e1000204, 2009.
- [155] J. S. Lowengrub, A. Rätz, and A. Voigt. Phase-field modeling of the dynamics of multicomponent vesicles: Spinodal decomposition, coarsening, budding, and fission. *Phys Rev E Stat Nonlin Soft Matter Phys*, 79:031926, 2009.
- [156] A. Marciniak-Czochra. Receptor-based models with hysteresis for pattern formation in *Hydra*. *Math Biosci*, 199:97–119, 2006.
- [157] A. J. Markvoort, K. Pieterse, M. N. Steijaert, P. Spijker, and P. A. J. Hilbers. The bilayer-vesicle transition is entropy driven. *J Phys Chem B*, 109:22649–22654, 2005.
- [158] A. J. Markvoort, P. Spijker, A. F. Smeijers, K. Pieterse, R. A. van Santen, and P. A. J. Hilbers. Vesicle deformation by draining: geometrical and topological shape changes. *J Phys Chem B*, 113:8731–8737, 2009.

- [159] A. J. Markvoort, R. A. van Santen, and P. A. J. Hilbers. Vesicle shapes from molecular dynamics simulations. *J Phys Chem B*, 110:22780–22785, 2006.
- [160] R. J. Mashl and R. F. Bruinsma. Spontaneous-curvature theory of clathrin-coated membranes. *Biophys J*, 74:2862–2875, 1998.
- [161] H. T. McMahon and J. L. Gallop. Membrane curvature and mechanisms of dynamic cell membrane remodelling. *Nature*, 438:590–596, 2005.
- [162] H. Meinhardt and A. Gierer. Pattern formation by local self-activation and lateral inhibition. *Bioessays*, 22:753–760, 2000.
- [163] M. Mercker. Ein kontinuierliches dynamisches Modell der Deformation und Phasenseparation von Biomembranen. Master’s thesis, Applied Analysis Group, Heidelberg, 2011.
- [164] M. Mercker, D. Hartmann, M. Zigman, and A. Marciniak-Czochra. On the coupling of tissue mechanics with morphogen expression: A new model for early pattern formation in *Hydra* polyps. *In preperation, on inquiry preprint available*, 2011.
- [165] M. Mercker, M. Ptashnyk, J. Kühnle, D. Hartmann, M. Weiss, and W. Jäger. A multiscale approach to curvature modulated sorting in biological membranes. *In review in the Journal of Theoretical Biology, on inquiry preprint available*, 2011.
- [166] M. Mercker, T. Richter, and D. Hartmann. Impact of elastic parameters on membrane shape and budding transition. *In review in Physical Review E, on inquiry preprint available*, 2011.
- [167] M. Mercker, T. Richter, and D. Hartmann. Sorting mechanisms and communication in phase-separating coupled monolayers. *J Phys Chem B*, 115:11739–11745, 2011.
- [168] H. Metiu, K. Kitahara, and J. Ross. A derivation and comparison of two equations (Landau-Ginzburg and Cahn) for the kinetics of phase transitions. *J Chem Phys*, 65:393–396, 1976.
- [169] L. Miao, U. Seifert, M. Wortis, and H. Döbereiner. Budding transitions of fluid-bilayer vesicles: The effect of area-difference elasticity. *Phys Rev E Stat Phys Plasmas Fluids Relat Interdiscip Topics*, 49:5389–5407, 1994.
- [170] I. Mikhalyov and A. Samsonov. Lipid raft detecting in membranes of live erythrocytes. *Biochim Biophys Acta*, 1808:1930–1939, 2011.
- [171] A. Minami and K. Yamada. Domain-induced budding in buckling membranes. *Eur Phys J E Soft Matter*, 23:367–374, 2007.

- [172] J. H. Miner and P. D. Yurchenco. Laminin functions in tissue morphogenesis. *Annu Rev Cell Dev Biol*, 20:255–284, 2004.
- [173] D. Morozova, G. Guigas, and M. Weiss. Dynamic structure formation of peripheral membrane proteins. *PLoS Comput Biol Biol*, 7:1–11, 2011.
- [174] B. L. Mui, H. G. Döbereiner, T. D. Madden, and P. R. Cullis. Influence of transbilayer area asymmetry on the morphology of large unilamellar vesicles. *Biophys J*, 69:930–941, 1995.
- [175] C. Mullins. *Molecular Biology Intelligence Unit: The biogenesis of cellular organelles*. Plenum publishers New York, 2005.
- [176] J. Murray. *Mathematical Biology II: Spatial models and biomedical applications*. Springer-Verlag Berlin, Heidelberg, 2003.
- [177] J. D. Murray. *Conference on: Modelling of Patterns in Space and Time, Heidelberg 1983. Lecture Notes in Biomathematics Series*. Springer Verlag Berlin-Heidelberg-New York, 1983.
- [178] J. D. Murray. On the mechanochemical theory of biological pattern formation with application to vasculogenesis. *C R Biol*, 326:239–252, 2003.
- [179] J. D. Murray, G. C. Cruywagen, and P. K. Maini. *Pattern formation in tissue interaction models*. Springer Verlag, Heidelberg, Germany, 1994.
- [180] B. N. Nagorcka, V. S. Manoranjan, and J. D. Murray. Complex spatial patterns from tissue interactions - an illustrative model. *J Theo Biol*, 128:359–374, 1987.
- [181] C. M. Nelson. Personal communication. 2011.
- [182] C. M. Nelson, R. P. Jean, J. L. Tan, W. F. Liu, N. J. Sniadecki, A. A. Spector, and C. S. Chen. Emergent patterns of growth controlled by multicellular form and mechanics. *PNAS*, 102:11594–11599, 2005.
- [183] H. Noguchi. Solvent-free coarse-grained lipid model for large-scale simulations. *J Chem Phys*, 134:055101, 2011.
- [184] D. Norouzi, M. M. Mueller, and M. Deserno. How to determine local elastic properties of lipid bilayer membranes from atomic-force-microscope measurements: a theoretical analysis. *Phys Rev E Stat Nonlin Soft Matter Phys*, 74:061914, 2006.
- [185] A. Novick-Cohen. The nonlinear Cahn-Hilliard equation: transition from spinodal decomposition to nucleation behavior. *J Stat Phys*, 38:707–722, 1985.
- [186] G. Odel, G. Oster, B. Burnside, and P. Alberch. The mechanical basis for morphogenesis. *Dev Biol*, 85:446–462, 1981.

- [187] A. W. Orr, B. P. Helmke, B. R. Blackman, and M. A. Schwartz. Mechanisms of mechanotransduction. *Dev Cell*, 10:11–20, 2006.
- [188] M. Orsi, D. Y. Haubertin, W. E. Sanderson, and J. W. Essex. A quantitative coarse-grain model for lipid bilayers. *J Phys Chem B*, 112:802–815, 2008.
- [189] G. F. Oster, J. D. Murray, and A. K. Harris. Mechanical aspects of mesenchymal morphogenesis. *J Embryol Exp Morphol*, 78:83–125, 1983.
- [190] W. Otter and W. Briels. The bending rigidity of an amphiphilic bilayer from equilibrium and nonequilibrium molecular dynamics. *J Chem Phys*, 118:4712–4720, 2003.
- [191] S. Oversteegen and E. Blokhuis. Rigidity constants from mean-field models. *J Chem Phys*, 112:2980–2986, 2000.
- [192] R. Parthasarathy and J. Groves. Curvature and spatial organisation in biological membranes. *Soft Matter*, 3:24–33, 2007.
- [193] R. Parthasarathy, C. Yu, and J. Groves. Curvature-modulated phase separation in lipid bilayer membranes. *Langmuir*, 22:5095–5099, 2006.
- [194] P. Patwari and R. T. Lee. Mechanical control of tissue morphogenesis. *Circ Res*, 103:234–243, 2008.
- [195] B. M. Pearse. Clathrin: a unique protein associated with intracellular transfer of membrane by coated vesicles. *PNAS*, 73:1255–1259, 1976.
- [196] J. Pencer, A. Jackson, N. Kucerka, M.-P. Nieh, and J. Katsaras. The influence of curvature on membrane domains. *Eur Biophys J*, 37:665–671, 2008.
- [197] Peterson. Comment on "instability and deformation of a spherical vesicle by pressure". *Phys Rev Lett*, 61:1325, 1988.
- [198] A. Polden. Curves and surfaces of least total curvature and fourth-order flows. *Dissertation, Mathematisches Institut, Universitaet Tübingen*, 1996.
- [199] T. Pomorski and A. K. Menon. Lipid flippases and their biological functions. *Cell Mol Life Sci*, 63:2908–2921, 2006.
- [200] J. D. Potter. Morphogens, morphostats, microarchitecture and malignancy. *Nat Rev Cancer*, 7:464–474, 2007.
- [201] S. Ramachandran, P. B. S. Kumar, and M. Laradji. Lipid flip-flop driven mechanical and morphological changes in model membranes. *J Chem Phys*, 129:125104, 2008.
- [202] S. Ramaswamy, J. Toner, and J. Prost. Nonequilibrium fluctuations, traveling waves, and instabilities in active membranes. *Phys Rev Lett*, 84:3494–3497, 2000.

- [203] M. Rauzi and T. Lecuit. Closing in on mechanisms of tissue morphogenesis. *Cell*, 137:1183–1185, 2009.
- [204] W. Rawicz, K. C. Olbrich, T. McIntosh, D. Needham, and E. Evans. Effect of chain length and unsaturation on elasticity of lipid bilayers. *Biophys J*, 79:328–339, 2000.
- [205] B. J. Reynwar, G. Illya, V. A. Harmandaris, M. M. Mueller, K. Kremer, and M. Deserno. Aggregation and vesiculation of membrane proteins by curvature-mediated interactions. *Nature*, 447:461–464, 2007.
- [206] J. E. Rim, T. S. Ursell, R. Phillips, and W. S. Klug. Morphological phase diagram for lipid membrane domains with entropic tension. *Phys Rev Lett*, 106:057801, 2011.
- [207] H. J. Risselada and S. J. Marrink. Curvature effects on lipid packing and dynamics in liposomes revealed by coarse grained molecular dynamics simulations. *Phys Chem Chem Phys*, 11:2056–2067, 2009.
- [208] M. Röger and M. Peletier. Cell membranes, lipid bilayers, and the Elastica functional. *Proc Appl Math Mech*, 6:11–14, 2006.
- [209] V. Romero-Rochn, C. Varea, and A. Robledo. Microscopic expressions for interfacial bending constants and spontaneous curvature. *Phys Rev A*, 44:8417–8420, 1991.
- [210] A. Roux, D. Cuvelier, P. Nassoy, J. Prost, P. Bassereau, and B. Goud. Role of curvature and phase transition in lipid sorting and fission of membrane tubules. *EMBO J*, 24:1537–1545, 2005.
- [211] R. Rusu. An algorithm for the elastic flow of surfaces. *Interfaces and Free Boundaries*, 7:229–239, 2005.
- [212] B. Rzycki, T. R. Weikl, and R. Lipowsky. Stable patterns of membrane domains at corrugated substrates. *Phys Rev Lett*, 100:098103, 2008.
- [213] S. Safran. *Statistical Thermodynamics of Surfaces, Interfaces and Membranes Ch. 1-3*. Addison-Wesley, Reading, 1994.
- [214] U. Schmidt, G. Guigas, and M. Weiss. Cluster formation of transmembrane proteins due to hydrophobic mismatching. *Phys Rev Lett*, 101:128104, 2008.
- [215] U. Schmidt and M. Weiss. Anomalous diffusion of oligomerized transmembrane proteins. *J Chem Phys*, 134:165101, 2011.
- [216] U. Schwarz and G. Gompper. Bicontinuous surfaces in self-assembling amphiphilic systems. *Lect Notes Phys*, 600, 2002.

- [217] U. Seifert. Curvature-induced lateral phase segregation in two-component vesicles. *Phys Rev Lett*, 70:1335–1338, 1993.
- [218] U. Seifert. Configurations of fluid membranes and vesicles. *Adv Phys Lett*, 46:13–137, 1997.
- [219] U. Seifert, K. Berndl, and R. Lipowsky. Shape transformations of vesicles: Phase diagram for spontaneous- curvature and bilayer-coupling models. *Phys Rev A*, 44:1182–1202, 1991.
- [220] S. Semrau, T. Idema, L. Holtzer, T. Schmidt, and C. Storm. Accurate determination of elastic parameters for multicomponent membranes. *Phys Rev Lett*, 100:088101, 2008.
- [221] M. P. Sheetz and S. J. Singer. Biological membranes as bilayer couples. a molecular mechanism of drug-erythrocyte interactions. *PNAS*, 71:4457–4461, 1974.
- [222] Q. Shi and G. A. Voth. Multi-scale modeling of phase separation in mixed lipid bilayers. *Biophys J*, 89:2385–2394, 2005.
- [223] Y. Shibata, J. Hu, M. M. Kozlov, and T. A. Rapoport. Mechanisms shaping the membranes of cellular organelles. *Annu Rev Cell Dev Biol*, 25:329–354, 2009.
- [224] S. Sick, S. Reinker, J. Timmer, and T. Schlake. WNT and DKK determine hair follicle spacing through a reaction-diffusion mechanism. *Science*, 314:1447–1450, 2006.
- [225] D. P. Siegel. The Gaussian curvature elastic energy of intermediates in membrane fusion. *Biophys J*, 95:5200–5215, 2008.
- [226] D. P. Siegel and M. M. Kozlov. The Gaussian curvature elastic modulus of N-monomethylated dioleoylphosphatidylethanolamine: relevance to membrane fusion and lipid phase behavior. *Biophys J*, 87:366–374, 2004.
- [227] G. Simonett. The Willmore flow near spheres. *Differential and Integral Equations*, 14:1005–1014, 2001.
- [228] S. J. Singer and G. L. Nicolson. The fluid mosaic model of the structure of cell membranes. *Science*, 175:720–731, 1972.
- [229] A. F. Smeijers, A. J. Markvoort, K. Pieterse, and P. A. J. Hilbers. A detailed look at vesicle fusion. *J Phys Chem B*, 110:13212–13219, 2006.
- [230] A. E. Sowers and C. R. Hackenbrock. Rate of lateral diffusion of intramembrane particles: measurement by electrophoretic displacement and rerandomization. *PNAS*, 78:6246–6250, 1981.

- [231] G. Staneva, M. I. Angelova, and K. Koumanov. Phospholipase A2 promotes raft budding and fission from giant liposomes. *Chem Phys Lipids*, 129:53–62, 2004.
- [232] C. D. Stoner. Inquiries into the nature of free energy and entropy in respect to biochemical thermodynamics. *Entropy*, 2:106–141, 2000.
- [233] I. P. Sugar, N. K. Mizuno, M. M. Momsen, and H. L. Brockman. Lipid lateral organization in fluid interfaces controls the rate of colipase association. *Biophys J*, 81:3387–3397, 2001.
- [234] S. Svetina and B. Zeks. Bilayer couple hypothesis of red cell shape transformations and osmotic hemolysis. *Biomed Biochim Acta*, 42:S86–S90, 1983.
- [235] I. Szleifer, D. Kramer, A. Ben-Shaul, W. Gelbart, and S. Safran. Molecular theory of curvature elasticity in surfactant films. *J Chem Phys*, 92:6800–6817, 1990.
- [236] I. Szleifer, D. Kramer, A. Ben-Shaul, D. Roux, and M. Gelbart. Curvature elasticity of pure and mixed surfactant films. *Phys Rev Lett*, 60:1966–1969, 1988.
- [237] T. Taniguchi. Shape deformation and phase separation dynamics of two-component vesicles. *Phys Rev Lett*, 76:4444–4447, 1996.
- [238] I. The and N. Perrimon. Morphogen diffusion: the case of the wingless protein. *Nat Cell Biol*, 2:E79–E82, 2000.
- [239] A. Tian and T. Baumgart. Sorting of lipids and proteins in membrane curvature gradients. *Biophys J*, 96:2676–2688, 2009.
- [240] F.-C. Tsai and H.-Y. Chen. Adsorption-induced vesicle fission. *Phys Rev E Stat Nonlin Soft Matter Phys*, 78:051906, 2008.
- [241] A. M. Turing. The chemical basis of morphogenesis. *Phil Trans R Soc London B*, 237:37–72, 1953.
- [242] P. Van. Wealy nonlocal irreversible thermodynamics - the Ginzburg-Landau equation. *Technische Mechanik*, 22:104–110, 2002.
- [243] G. van Meer, D. R. Voelker, and G. W. Feigenson. Membrane lipids: where they are and how they behave. *Nat Rev Mol Cell Biol*, 9:112–124, 2008.
- [244] S. L. Veatch and S. L. Keller. Separation of liquid phases in giant vesicles of ternary mixtures of phospholipids and cholesterol. *Biophys J*, 85:3074–3083, 2003.
- [245] D. Vind-Kezunovic, C. H. Nielsen, U. Wojewodzka, and R. Gniadecki. Line tension at lipid phase boundaries regulates formation of membrane vesicles in living cells. *Biochim Biophys Acta*, 1778:2480–2486, 2008.

- [246] V. J. Vinson. Proteins in motion. Introduction. *Science*, 324:197, 2009.
- [247] A. J. Wagner, S. Löw, and S. May. Influence of monolayer-monolayer coupling on the phase behavior of a fluid lipid bilayer. *Biophys J*, 93:4268–4277, 2007.
- [248] X. Wang and Q. Du. Modelling and simulations of multi-component lipid membranes and open membranes via diffuse interface approaches. *J Math Biol*, 56:347–371, 2008.
- [249] S. Welsch, S. Miller, I. Romero-Brey, A. Merz, C. Bleck, P. Walther, S. Fuller, C. Antony, J. Krijnse-Locker, and R. Bartenschlager. Composition and three-dimensional architecture of the dengue virus replication and assembly sites. *Cell Host and Microbe*, 5:365–375, 2009.
- [250] T. Willmore. *Geometry and Topology of Submanifolds IV*. Worlds Sci. Pub., 1992.
- [251] A. Würger. Bending elasticity of surfactant films: the role of the hydrophobic tails. *Phys Rev Lett*, 85:337–340, 2000.
- [252] A. Yamamoto and H. S. Budding and fission dynamics of two-component vesicles. *J Chem Phys*, 118:7937–7943, 2003.
- [253] S. Yamamoto, Y. Maruyama, and S. Hyodo. Dissipative particle dynamics study of spontaneous vesicle formation. *J Chem Phys*, 116:5842, 2002.
- [254] M. Yanagisawa, M. Imai, and T. Taniguchi. Shape deformation of ternary vesicles coupled with phase separation. *Phys Rev Lett*, 100:148102, 2008.
- [255] M. Yanagisawa, M. Imai, and T. Taniguchi. Periodic modulation of tubular vesicles induced by phase separation. *Phys Rev E Stat Nonlin Soft Matter Phys*, 82:051928, 2010.
- [256] K. Yang, X. Shao, and Y.-Q. Ma. Shape deformation and fission route of the lipid domain in a multicomponent vesicle. *Phys Rev E Stat Nonlin Soft Matter Phys*, 79:051924, 2009.
- [257] A. Yeung. *Mechanics of Inter-Monolayer Coupling in Fluid Surfactant Bilayers*. PhD thesis, University of British Columbia, 1994.
- [258] Y. Yin. Integral theorems based on a new gradient operator derived from biomembranes (part ii): Applications. *Tsinghua science and technology*, 10:376–380, 2005.
- [259] Y. Yin, Y. Chen, D. Ni, H. Shi, and Q. Fan. Shape equations and curvature bifurcations induced by inhomogeneous rigidities in cell membranes. *J Biomech*, 38:1433–1440, 2005.

- [260] Y. Yin and C. Lv. Equilibrium theory and geometrical constraint equation for two-component lipid bilayer vesicles. *J Biol Phys*, 34:591–610, 2008.
- [261] Y. Yin, J. Wu, and J. Yin. Symmetrical fundamental tensors, differential operators, and integral theorems in differential geometry. *Tsinghua science and technology*, 13:121–126, 2008.
- [262] T.-Y. Yoon, C. Jeong, S.-W. Lee, J. H. Kim, M. C. Choi, S.-J. Kim, M. W. Kim, and S.-D. Lee. Topographic control of lipid-raft reconstitution in model membranes. *Nat Mater*, 5:281–285, 2006.
- [263] T. Yoshigaki. Theoretically predicted effects of Gaussian curvature on lateral diffusion of membrane molecules. *Phys Rev E Stat Nonlin Soft Matter Phys*, 75:041901, 2007.
- [264] Y. Yu, J. Vroman, S. Bae, and S. Granick. Vesicle budding induced by a pore-forming peptide. *JACS*, 132:195–201, 2010.
- [265] H. Yuan, C. Huang, J. Li, G. Lykotrafitis, and S. Zhang. One-particle-thick, solvent-free, coarse-grained model for biological and biomimetic fluid membranes. *Phys Rev E Stat Nonlin Soft Matter Phys*, 82:011905, 2010.
- [266] Zhong-can and Helfrich. Instability and deformation of a spherical vesicle by pressure. *Phys Rev Lett*, 59:2486–2488, 1987.
- [267] O. Zhong-Can and W. Helfrich. Bending energy of vesicle membranes: General expressions for the first, second, and third variation of the shape energy and applications to spheres and cylinders. *Phys Rev A*, 39:5280–5288, 1989.
- [268] M. Zigman. Personal communication, 2011.
- [269] J. Zimmerberg and M. M. Kozlov. How proteins produce cellular membrane curvature. *Nat Rev Mol Cell Biol*, 7:9–19, 2006.

ACKNOWLEDGEMENTS

First of all, I would like to thank my supervisors Prof. Willi Jäger and Prof. Matthias Weiss as well as Prof. Anna Marciniak-Czochra for having offered me the possibility to work on the presented topic. It has constituted an ideal fusion of my scientific interests, making the last years to the most exciting research time of my life. Furthermore, I would like to thank them all for interesting discussions, for always being interested in real interdisciplinary work and for their support and understanding combining research and being a new father.

Particularly, I would like to highlight the reliable encouragement and patience of my supervisor Dirk Hartmann at any time. Various stimulating discussions with him, his experiences and his moral support played an important role for me during the last years.

Moreover, I would like to thank Thomas Richter for the excellent and constant Gascoigne support, Mariya Ptashnyk, Mihaela Žigman and Jens Kühnle for very fruitful discussions on the mathematical, the biological and the biophysical part of this thesis, respectively and Dirk Hartmann, Alexandra Köthe and Prof. Anna Marciniak-Czochra for proofreading.

Finally, I would like to thank Virginie for her constant love, motivation, and idealistic support. Together with our daughter Eline she always took care for my balance between research and family, which has been an outstanding source of satisfaction.